

Solution of Electromagnetic Problems by the Moment Method :
Performance and Limitations

A Thesis

Presented to

The Department of Electrical Engineering
The Faculty of Engineering
The University of Manitoba

In Partial Fulfillment
of the Requirements for the Degree
Master of Science

by

Chun Wai Lee

Winnipeg, Manitoba, 1984

(c) Chun Wai Lee, 1984

SOLUTION OF ELECTROMAGNETIC PROBLEMS BY THE MOMENT METHOD :
PERFORMANCE AND LIMITATIONS

by

Chun Wai Lee

A thesis submitted to the Faculty of Graduate Studies of
the University of Manitoba in partial fulfillment of the requirements
of the degree of

MASTER OF SCIENCE

© 1984

Permission has been granted to the LIBRARY OF THE UNIVER-
SITY OF MANITOBA to lend or sell copies of this thesis. to
the NATIONAL LIBRARY OF CANADA to microfilm this
thesis and to lend or sell copies of the film, and UNIVERSITY
MICROFILMS to publish an abstract of this thesis.

The author reserves other publication rights, and neither the
thesis nor extensive extracts from it may be printed or other-
wise reproduced without the author's written permission.

ABSTRACT

For both scattering and antenna problems the electric field and magnetic field integral equation formulations are considered. It is shown that by using the moment method these integral equations can be reduced to a set of linear equations, whose matrix solution gives the required field distribution. The moment method is applied to both scattering and antenna problems, and the computed results are compared with either analytic solutions or experimental data so that the constraints of the method can be analyzed. Based on these investigations, the performance and limitations of the moment method are summarized. Computation techniques which overcome some of these limitations are then described. Finally, the thesis discusses a rapid and reasonably accurate method which can be used to calculate field solutions from electrically large objects.

ACKNOWLEDGEMENTS

The author wishes to thank Dr. L. Shafai for his patient supervision and encouragement over the course of this work.

Drs. O. Aboul-Atta and I.M.R. Ciric are thanked for many helpful discussions and suggestions.

The author is grateful to all his colleagues, especially Mr. G. Bridges and Mr. G. McGonigal, for their invaluable assistance.

Financial assistance from the Natural Sciences and Engineering Research Council of Canada is gratefully acknowledged.

TABLE OF CONTENTS

ABSTRACT	ii
ACKNOWLEDGEMENTS	iii
TABLE OF CONTENTS	iv
LIST OF TABLES	vi
LIST OF FIGURES	vii
LIST OF PRINCIPAL SYMBOLS	x

<u>Chapter</u>	<u>page</u>
I. INTRODUCTION	1
II. A REVIEW OF THE INTEGRAL EQUATION FORMULATION FOR TIME-HARMONIC ELECTROMAGNETIC FIELDS	6
Electromagnetic Field Solution in an Infinite Domain	10
Electric Field Integral Equations (EFIE)	11
Magnetic Field Integral Equations (MFIE)	14
Numerical Solution	16
III. APPLICATIONS	19
Modeling Methodology	21
Wire Modeling	21
Surface-Patch Modeling	24
Application to Scattering Problems	28
Analytical Method	29
Wire-Grid Approach	30
Surface Patch Approach	37
Comparison of Wire-Grid and Surface-Patch Modeling Schemes	43
Application to Wire Antennas	46
Sandwich Wire Antenna	47
IV. TECHNIQUES FOR THE SOLUTION OF ELECTRICALLY LARGE STRUCTURES	58
Utilization of Symmetry	58
Virtual Memory Addressing Technique	60
Progressive Numerical Method (PNM)	63
Description of the Method	64
Discussion of the Method	68

Optimal Parameters for the PNM 71
V. CONCLUSION 87

Appendix page
A. THE PNM PROGRAM 90
B. FLOW CHARTS FOR THE OPTIMIZATION PROGRAM 98
C. MULTI-STAGE OPTIMIZATION PROGRAM 102
REFERENCES 107

LIST OF TABLES

<u>Table</u>		<u>page</u>
4.1	Comparison of Matrix Storage, Fill-up Time, and Factor Time for Different Numbers of Planes of Symmetry	59
4.2	Comparison of the Performance of NEC for a Structure of 108 Segments	63
4.3	Optimal Results of Stage 3 for $ka = 10$	78
4.4	Optimal Results of Stage 3 for different ka values	79
4.5	Comparison of the Computational Errors, Time, and Storage Requirements of the Moment Method and the PNM	80

LIST OF FIGURES

<u>Figure</u>	<u>page</u>
2.1 General Representation of Scattering Geometry	8
2.2 Geometry for Scattering by a Thin Wire	13
2.3 Geometry Pertaining to MFIE	15
3.1 Block Diagram of the Overall Structure of an Electromagnetic Response Analysis Program	20
3.2 Modeling of a Sphere with Wire-grid Approach	24
3.3 Patch Position and Orientation	25
3.4 Modeling of Spheres Using Uniform and Variable Segmentation Schemes	26
3.5 Scattering Problem Geometry	28
3.6 Wire Segmentation Scheme	31
3.7 Comparison (A) of E-plane Scattering Cross-section with Wire-grid Model for Different Wire Radius	33
3.8 Comparison (A) of H-plane Scattering Cross-section with Wire-grid Model for Different Wire Radius	34
3.9 Comparison (B) of E-plane Scattering Cross-section with Wire-grid Model for Different Wire Radius	35
3.10 Comparison (B) of H-plane Scattering Cross-section with Wire-grid Model for Different Wire Radius	36
3.11 Surface Patch Segmentation for a Sphere	37
3.12 E-plane Scattering Cross-section of a Sphere When $Ka = 4$. .	39
3.13 H-plane Scattering Cross-section of a Sphere When $Ka = 4$. .	40
3.14 E-plane Scattering Cross-section of a Sphere When $Ka = 12$.	41
3.15 H-plane Scattering Cross-section of a Sphere When $Ka = 12$.	42

3.16	Comparison of E-plane Scattering Cross-section using NEC and Analytical Method	44
3.17	Comparison of H-plane Scattering Cross-section using NEC and Analytical Method	45
3.18	Geometry of a Sandwich Wire Antenna	47
3.19	Geometry of a Central Conductor with Tapered Trapezoidal Undulations	48
3.20	Wire Modeling of a Sandwich Wire Antenna with Tapered Trapezoidal Undulations	50
3.21	Comparison of H-plane Radiation Patterns of Different Segment Lengths	53
3.22	Comparison between the Calculated and Measured H-plane Radiation Patterns	54
3.23	Comparison (A) of H-plane Radiation Patterns for Different L/R Ratios	55
3.24	Comparison (B) of H-plane Radiation Patterns for Different L/R Ratios	56
3.25	Beam Squint with Respect to Different Frequencies	57
4.1	Dividing an Object into Several Small Sub-regions	65
4.2	Geometry of Overlapping Regions	67
4.3	Matrix Representation of Overlapping Regions	67
4.4	Cross Section of a Circular Cylinder and Coordinate System .	77
4.5	Comparison of the Moment Method Surface Current with the Exact Solution	83
4.6	Comparison of the PNM Surface Current with the Exact Solution	84
4.7	Comparison of the Moment Method Far Scattered Field with The Exact Solution	85
4.8	Comparison of the PNM Far Scattered Field with The Exact Solution	86
B.1	Block Diagram of the Staged Analysis Program	98
B.2	Flow Chart for Stage 1 of the Staged-program	99
B.3	Flow Chart for Stage 2 (Grid Search)	100

B.4 Flow Chart for Stage 3 101

LIST OF PRINCIPAL SYMBOLS

<u>Symbol</u>	<u>Description</u>
a	Wire radius
\vec{A}	Vector magnetic potential
\vec{B}	Magnetic flux density
C	Total in-core memory available for a program
\vec{D}	Electric flux density
e	Excitation source
E_0	Magnitude of the incident electric field
\vec{E}	Electric field intensity
\vec{E}^i	External incident electric field
\vec{E}^s	Scattered electric field
f	Unknown function to be expanded by the moment method
f_j	Basis functions
F_n	Objective function n for the optimization process
g	Free-space Green's function of a three-dimensional scalar wave function
$\vec{\vec{G}}$	Free-space dyadic Green's function
\vec{H}	Magnetic field intensity
\vec{H}^i	External incident magnetic field
\vec{H}^s	Scattered magnetic field
H_n	Hankel function of order n
\hat{H}_n	Riccati Hankel function of order n
I	Current intensity

$\bar{\bar{I}}$	Unit dyad
\bar{J}	Electric current density
\bar{J}_s	Induced surface current density
\hat{J}_n	Riccati Bessel function of order n
k	Wave propagation constant
\bar{K}	Magnetic current density
ℓ	Wire segment length
ℓ'	Distance parameter along the wire axis at r'
$\hat{\ell}'$	Unit vector tangent to the wire axis at r'
L	Linear operator
m	Magnetic charge density
M	Dimension of the sub-region matrix used by the PNM
\hat{n}	Unit normal vector
N	Dimension of the coefficient matrix
P_n	Legendre polynomial of order n
r	Radius of a wire segment
\bar{r}	Vector position of the observation point
\bar{r}'	Vector position of the source point
s	Numbers of planes of symmetry
S	Number of elements per region
t	Time
\hat{t}	Orthogonal surface unit vector
T	Total computation time
w_i	Weighting functions
X_1	Number of divisions per wavelength
X_2	Sub-region size for each evaluation step used in the PNM
X_3	Number of calculated current pulses which are discarded

[E]	Excitation source vector
[G]	Structure element coefficient matrix
[I]	Vector of unknown current distributions
α_j	Unknown coefficients obtained by expanding a function
δ	Dirac delta function
ϵ	Permittivity
η	Free space wave impedance
λ	Wavelength
μ	Permeability
ρ	Electric charge density
σ	Conductivity
τ	Average CPU time required for one operation
ϕ	Scalar electric potential
ω	Angular frequency
f	Principal value of the integral
∇'_s	Surface divergence operator in source coordinates

Chapter I

INTRODUCTION

The time-harmonic response of electromagnetic waves in the presence of a scatterer depends on: i) the configuration and material properties of the object and ii) the propagation frequency, polarization, and angle of incidence of the impinging field. The distinction between antennas and scatterers is dependent upon the source location. If the source is on the object, it is considered to be an antenna; if the source is distant from the object, it is viewed as a scatterer. By analyzing the problem with an appropriate source for the impressed field [1, p. 116], one can solve both these problems using the same solution technique.

Classical solutions involving expansions of cylindrical (two-dimensional), spherical and spheroidal wave functions, exist only for a limited class of geometries where separation of variables may be practiced. In the low-frequency region, analytic solutions are obtained in the form of convergent power series expansions [2]. At high-frequencies, techniques such as ray tracing or physical optics [3], geometrical optics, and the geometrical theory of diffraction [4] become applicable and can be used to generate asymptotic solutions. Corresponding techniques for the transition or the resonance region includes modal expansion [5] and the method of conformal transformation [6].

In recent years, with the advent of high-speed and large-storage digital computers, considerable interest has been shown in the application of numerical solution techniques to the evaluation of scattering and radiating problems. The scattering properties of complex bodies can be computed with very high accuracy through the use of numerical techniques. Of the many approaches available for the formulation of these problems, the integral equation method appears to be the one most conveniently adaptable to computer solution [7, p. 1].

For perfect electric conductors, two usual integral equations [7, p. 168] are (with a time factor $e^{j\omega t}$, which is suppressed)

$$\hat{n}(\bar{r}) \times \bar{E}^i(\bar{r}) = \frac{j\omega\mu}{4\pi} \hat{n}(\bar{r}) \times \int_S [\bar{J}_S(\bar{r}')g(\bar{r},\bar{r}') - \frac{1}{k^2} \nabla'_S \cdot \bar{J}_S(\bar{r},\bar{r}') \nabla'g(\bar{r},\bar{r}')] dS', \quad \bar{r} \in S \quad (1.1)$$

and

$$\bar{J}_S(\bar{r}) = 2\hat{n}(\bar{r}) \times \bar{H}^i(\bar{r}) + \frac{1}{2\pi} \int_S \hat{n}(\bar{r}) \times [\bar{J}_S(\bar{r}') \times \nabla'g(\bar{r},\bar{r}')] dS', \quad \bar{r} \in S. \quad (1.2)$$

These two equations, together with the detailed definition of their nomenclature, are explained in Chapter II. Equations (1.1) and (1.2) are vector integral equations for the field vectors $\bar{E}(\bar{r})$ and $\bar{H}(\bar{r})$ (where $\bar{r} \in S$) and are generally referred to as the electric field integral equation (EFIE) and the magnetic field integral equation (MFIE), respectively.

Either of these equations can be solved for the surface current. Whether to use the EFIE or MFIE will, in general, be dictated by the geometry of the scatterer and the intended solution technique. In practice it is generally preferred to use the EFIE for wire structures and the MFIE for volumetric surfaces. For a structure containing both wires and surfaces the EFIE and MFIE are usually coupled. The EFIE is ideally suited for thin-wire structures of vanishing volume since the axial currents are assumed to be constrained along the wire. Nevertheless, the EFIE can also be used to analyze thin structures where there is little separation between the front and back surfaces.

The problem of determining the current distribution in an antenna can be formulated in terms of either (1.1) or (1.2). The integral equation can be solved using the computer by first transforming it into a matrix equation. The solution for the current distribution on the antenna, the input impedance and the radiation pattern, etc., may all be computed from the knowledge of the numerical solution of the integral equation.

Equations (1.1) and (1.2) give the relationships between the incident field on the surface of an object, the surface currents, and charges which is represented by the divergence of the surface current density \bar{J}_s . Because both equations involve vector operations of complex forms, the object identification plays an important role in the accuracy of the solution. The antenna or scattering surface must be modeled correctly and, preferably, in a simple form. Nevertheless, the accuracy and other performance characteristics of a numerical program will heavily depend on the proper modeling of the object.

The moment method is a common numerical technique for solving integral equations. To solve the integral equation easily, accurately, and rapidly, the constraints of this numerical method must be known. A limitation of this method, when used to analyze scattering problems, is that the electrical dimensions of the scattering body cannot be larger than a few wavelengths since large bodies result in large matrices which dictate excessive computer storage and execution time. In addition, the accumulation of errors while inverting large matrices greatly impairs the accuracy of the solution.

The application of the moment method to scattering bodies with sharp edges introduces another type of problem. When certain field components become infinite, an accurate evaluation of these components requires careful treatment. Shafai [13, 14, 15] has related singularities at sharp edges of the scatterer using a transformation method. Abdelmessih and Sinclair [16] described the exact behavior of the fields at the edges by the Meixner edge conditions [17]. Much other work has also been accomplished [19], but the simplest approach, however, is to ignore the contribution of the edge currents by placing the sampling points near but not on the edge itself. Kay and Nihon [18] have demonstrated the validity of this approach by solving the problem of scattering from a perfectly conducting rectangle. Their results show that for step sizes less than $\lambda/10$, the resulting error in the calculated induced current due to a finite mesh size will not exceed two percent. In many cases, unless very high accuracy is required, the singularity may be ignored.

In summary, this thesis attempts to study the performance of the moment method by analyzing various modeling schemes, the effects of different geometries, and the constraints associated with large and complex structures. The results of this investigation will identify the limitations of the method. The study is concluded by recommending a technique which can extend the applicability of numerical methods to electrically large scattering or radiating objects.

In Chapter II, the scattering problem is formulated in the form of a set of integral equations. During the course of this study, a typical computer program, namely the Numerical Electromagnetic Code (NEC) [10, 11, 12] has been used to analyze the performance and limitations of the moment method. The program applies the moment method to both EFIE and MFIE integral equations for the solution of scattering and antenna problems. Chapter III presents the application of the integral equations to both scattering and antenna problems. Finally, Chapter IV discusses a rapid and reasonably accurate method which can be used to calculate the field responses from a scatterer having an area larger than $20 \lambda^2$.

Chapter II

A REVIEW OF THE INTEGRAL EQUATION FORMULATION FOR TIME-HARMONIC ELECTROMAGNETIC FIELDS

General solutions of the electromagnetic field problems satisfy Maxwell's equations, which are (in instantaneous values)

$$\nabla \times \bar{E} = -\frac{\partial \bar{B}}{\partial t} \quad (2.1)$$

$$\nabla \times \bar{H} = \frac{\partial \bar{D}}{\partial t} + \bar{J} \quad (2.2)$$

$$\nabla \cdot \bar{D} = \rho \quad (2.3)$$

$$\nabla \cdot \bar{B} = 0 \quad (2.4)$$

where

\bar{E} = electric field intensity

\bar{H} = magnetic field intensity

\bar{D} = electric flux density

\bar{B} = magnetic flux density

\bar{J} = electric current density

ρ = electric charge density.

For isotropic media the following constitutive equations are associated with the Eqns. (2.1) to (2.4)

$$\bar{D} = \epsilon \bar{E} \quad (2.5)$$

$$\bar{B} = \mu \bar{H} \quad (2.6)$$

$$\bar{J} = \sigma \bar{E} \quad (2.7)$$

where ϵ , μ and σ are the permittivity, permeability and conductivity, respectively.

In the case of time-harmonic electromagnetic fields, this system of equations can also be written in the following form (with the time factor $e^{j\omega t}$)

$$\nabla \times \bar{E} = -j\omega\mu\bar{H} - \bar{K} \quad (2.8)$$

$$\nabla \times \bar{H} = j\omega\epsilon\bar{E} + \bar{J} \quad (2.9)$$

$$\nabla \cdot \bar{E} = \rho/\epsilon \quad (2.10)$$

$$\nabla \cdot \bar{H} = m/\mu \quad (2.11)$$

where

\bar{K} = magnetic current density

m = magnetic charge density

ω = angular frequency.

The relationships defining the conservation of charges can be derived from Eqns (2.8) to (2.11) as

$$\nabla \cdot \bar{J} = -j\omega\rho \quad (2.12)$$

$$\nabla \cdot \bar{K} = -j\omega m \quad (2.13)$$

The second order equations, satisfied by \bar{E} and \bar{H} , are obtained from Eqns. (2.8) and (2.9)

$$\nabla \times \nabla \times \bar{E} - k^2 \bar{E} = -j\omega\mu\bar{J} - \nabla \times \bar{K} \quad (2.14)$$

$$\nabla \times \nabla \times \bar{H} - k^2 \bar{H} = -j\omega\epsilon\bar{K} + \nabla \times \bar{J} \quad (2.15)$$

where

$$k = \omega\sqrt{\epsilon\mu}. \quad (2.16)$$

The solution of electric and magnetic field equations must satisfy the following boundary conditions on any surface (S) separating two different media (1) and (2) as illustrated in Fig. 2.1

$$\hat{n} \times \bar{E}_1 = \hat{n} \times \bar{E}_2 \quad (2.17)$$

$$\hat{n} \times \bar{H}_1 = \hat{n} \times \bar{H}_2 \quad (2.18)$$

with \hat{n} being the unit vector normal to (S).

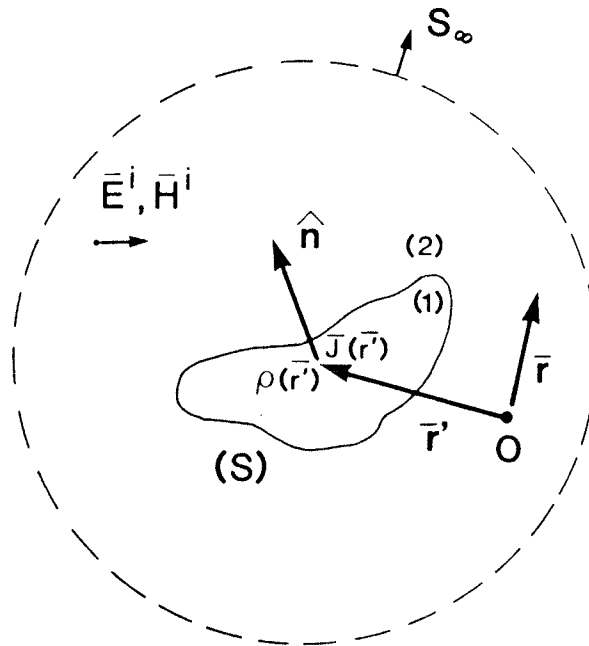


Figure 2.1: General Representation of Scattering Geometry

Electric and magnetic fields can be determined with the aid of vector and scalar potentials. For instance, the vector magnetic potential \bar{A} and the scalar electric potential ϕ may be defined such that

$$\bar{H} = \frac{1}{\mu} \nabla \times \bar{A} \quad (2.19)$$

$$\bar{E} = -j\omega\bar{A} - \nabla\phi . \quad (2.20)$$

Substituting these two expressions in Eqns. (2.9) and (2.10) and applying the Lorentz condition

$$\nabla \cdot \bar{A} + j\omega\epsilon\mu\phi = 0 , \quad (2.21)$$

the equations satisfying \bar{A} and ϕ are obtained, for homogeneous media, as the Helmholtz equations

$$\nabla^2\bar{A} + k^2\bar{A} = -\mu\bar{J} \quad (2.22)$$

$$\nabla^2\phi + k^2\phi = -\rho/\epsilon . \quad (2.23)$$

Once the vector potential \bar{A} has been determined the magnetic field intensity is given by Eqn. (2.19) and the electric field intensity is derived from Eqns. (2.20) and (2.21) to be

$$\bar{E} = -j\omega \left[1 + \frac{1}{k^2} \nabla\nabla \cdot \right] \bar{A} . \quad (2.24)$$

2.1 ELECTROMAGNETIC FIELD SOLUTION IN AN INFINITE DOMAIN

The solutions of Helmholtz equations (2.22) and (2.23) in an infinite domain, corresponding to outgoing waves from source, are given by [20, p. 26]

$$\bar{A}(\bar{r}) = \frac{\mu}{4\pi} \int_V \bar{J}(\bar{r}') g(\bar{r}, \bar{r}') dv' \quad (2.25)$$

and

$$\phi(\bar{r}) = \frac{1}{4\pi\epsilon} \int_V \rho(\bar{r}') g(\bar{r}, \bar{r}') dv' \quad (2.26)$$

where

$$g(\bar{r}, \bar{r}') = \frac{e^{-jk|\bar{r} - \bar{r}'|}}{|\bar{r} - \bar{r}'|} \quad (2.27)$$

is the free-space Green's function pertaining to a three-dimensional scalar wave equation. The vector position of the source point is denoted by \bar{r}' and that of the observation point by \bar{r} .

Substituting the vector potential (2.25) into Eqn. (2.24) and imposing the radiation condition [20, p. 27]

$$\lim_{r \rightarrow \infty} r \left[\nabla \times \begin{bmatrix} \bar{E} \\ \bar{H} \end{bmatrix} - jk\hat{r} \times \begin{bmatrix} \bar{E} \\ \bar{H} \end{bmatrix} \right] = 0, \quad (2.28)$$

the electric field intensity in the case of an infinite domain can be written in the form

$$\bar{E}(\bar{r}) = \frac{-j\omega\mu}{4\pi} \int_V \bar{J}(\bar{r}') \cdot \bar{G}(\bar{r}, \bar{r}') dv'. \quad (2.29)$$

Here $\bar{G}(\bar{r}, \bar{r}')$ is the free-space dyadic Green's function [20, p. 50] and is defined as the solution of the dyadic differential equation

$$\nabla \times \nabla \times \bar{G}(\bar{r}, \bar{r}') - k^2 \bar{G}(\bar{r}, \bar{r}') = 4\pi \bar{I} \delta(\bar{r} - \bar{r}') \quad (2.30)$$

where $\bar{\bar{I}}$ denotes the unit dyad (in Cartesian coordinates $\hat{x}\hat{x} + \hat{y}\hat{y} + \hat{z}\hat{z}$) and $\delta(\bar{r} - \bar{r}')$ is the Dirac delta function. The relationship between the free space dyadic Green's function and the free-space Green's function (2.27) is

$$\bar{\bar{G}}(\bar{r}, \bar{r}') = \left[\bar{\bar{I}} + \frac{1}{k^2} \nabla \nabla \right] g(\bar{r}, \bar{r}'). \quad (2.31)$$

Using the expression (2.25) in Eqn. (2.19), the magnetic field intensity is obtained as

$$\bar{H}(\bar{r}) = \frac{1}{4\pi} \int_V \bar{J}(\bar{r}') \times \nabla' g(\bar{r}, \bar{r}') dv' \quad (2.32)$$

with ∇' operating with respect to the integration variable \bar{r}' .

When the electric current is distributed on a surface, the volume integrals in Eqns (2.29) and (2.32) are replaced by the corresponding surface integrals.

2.2 ELECTRIC FIELD INTEGRAL EQUATIONS (EFIE)

The solution of electromagnetic field problems involving either surface or linear electric current distributions can be obtained via integral equations satisfied by the surface current density. From a numerical calculation point of view, these integral equations are, in general, much more effective than the direct solution of the corresponding partial differential equations. For instance, in the case a current distribution is limited to the surface (S) of a perfectly conducting body, Eqn. (2.29) becomes

$$\bar{E}(\bar{r}) = \frac{-j\omega\mu}{4\pi} \int_S \bar{J}_S(\bar{r}') \cdot \bar{\bar{G}}(\bar{r}, \bar{r}') dS', \quad (2.33)$$

where \bar{J}_S is the surface current density. If \bar{r} approaches (S) as a limit, this electric field is evaluated from

$$\bar{E}(\bar{r}) = \frac{-j\omega\mu}{4\pi} \oint_S \bar{J}_S(\bar{r}') \cdot \bar{G}(\bar{r}, \bar{r}') dS' \quad (2.34)$$

where \oint indicates the principal value of the integral since $\bar{G}(\bar{r}, \bar{r}')$ is unbounded for $\bar{r} = \bar{r}'$.

The electric field integral equation can be obtained from Eqn. (2.34) by imposing the boundary condition

$$\hat{n}(\bar{r}) \times [\bar{E}^s(\bar{r}) + \bar{E}^i(\bar{r})] \Big|_{\bar{r} \in S} = 0 \quad (2.35)$$

on the perfectly conducting surface with \bar{E}^s being the scattered field produced by the induced current \bar{J}_S and \bar{E}^i the external incident field. Using (2.33) for \bar{E}^s yields the EFIE in the case of a perfectly conducting surface as

$$\begin{aligned} \hat{n}(\bar{r}) \times \bar{E}^i(\bar{r}) &= \frac{j\omega\mu}{4\pi} \hat{n}(\bar{r}) \\ &\times \oint_S \bar{J}_S(\bar{r}') \cdot \left[\bar{I} + \frac{1}{k^2} \nabla \nabla \right] g(\bar{r}, \bar{r}') dS', \quad \bar{r} \in S. \end{aligned} \quad (2.36)$$

This equation can be written in an equivalent form as

$$\begin{aligned} \hat{n}(\bar{r}) \times \bar{E}^i(\bar{r}) &= \frac{j\omega\mu}{4\pi} \hat{n}(\bar{r}) \times \oint_S [\bar{J}_S(\bar{r}') g(\bar{r}, \bar{r}') \\ &- \frac{1}{k^2} \nabla'_S \cdot \bar{J}_S(\bar{r}') \nabla' g(\bar{r}, \bar{r}')] dS', \quad \bar{r} \in S \end{aligned} \quad (2.37)$$

where ∇'_S represents the surface divergence operator in source coordinates [7, p. 167].

By applying the vector integral equation (2.36) to the conducting surface of a thin cylindrical wire, the scalar EFIE [7, p. 171] is

$$\hat{\ell} \cdot \bar{E}^i(\bar{r}) = \frac{j\omega\mu}{4\pi} \int_L I(\ell') \left[\hat{\ell} \cdot \hat{\ell}' - \frac{1}{k^2} \frac{\partial^2}{\partial \ell \partial \ell'} \right] g(\bar{r}, \bar{r}') d\ell' \quad (2.38)$$

where $\bar{J}_S(\bar{r}')$ in Eqn. (2.36) is replaced by

$$\bar{J}_S(\bar{r}') = \frac{I(\ell')}{2\pi a} \hat{\ell}' \quad (2.39)$$

with (ref Fig. 2.2)

ℓ' = distance parameter along the wire axis at \bar{r}' ,

$\hat{\ell}'$ = unit vector tangent to the wire axis at \bar{r}' and

a = wire radius.

For thin wire scatterers the current I can be assumed to be on the wire axis. In such a case, since \bar{r}' is a point at ℓ' on the wire axis and \bar{r} is a point at ℓ on the wire surface, $|\bar{r} - \bar{r}'| \geq a$ and the integrand is always bounded.

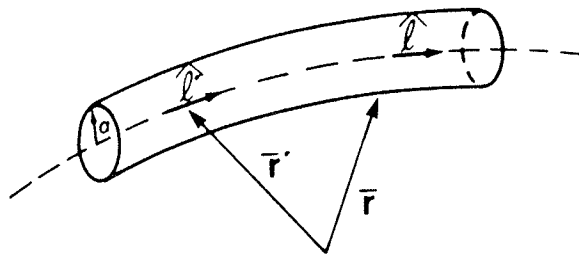


Figure 2.2: Geometry for Scattering by a Thin Wire

2.3 MAGNETIC FIELD INTEGRAL EQUATIONS (MFIE)

The magnetic field intensity produced by a surface current distribution \bar{J}_S is derived from Eqn. (2.32) as

$$\bar{H}(\bar{r}) = \frac{1}{4\pi} \int_S \bar{J}_S(\bar{r}') \times \nabla' g(\bar{r}, \bar{r}') dS' . \quad (2.40)$$

For a perfectly conducting surface (S), if the current \bar{J}_S is induced by an external incident magnetic field \bar{H}^i , then the total magnetic field inside the surface must be zero. Therefore, for \bar{r} just inside the surface (S)

$$\bar{H}^i(\bar{r}) + \bar{H}^s(\bar{r}) = 0 \quad (2.41)$$

where $\bar{H}^s(\bar{r})$ is the scattered field produced by the induced current \bar{J}_S in accordance with Eqn. (2.40). The MFIE in this case as obtained from the condition (2.41), by substituting the expression (2.40) for $\bar{H}^s(\bar{r})$, is in the form

$$\begin{aligned} \bar{J}_S(\bar{r}) = 2\hat{n}(\bar{r}) \times \bar{H}^i(\bar{r}) + \frac{1}{2\pi} \int_S \hat{n}(\bar{r}) \\ \times [\bar{J}_S(\bar{r}') \times \nabla' g(\bar{r}, \bar{r}')] dS' , \quad \bar{r} \in S \end{aligned} \quad (2.42)$$

with $\hat{n}(\bar{r})$ being the unit vector normal to the surface (S) at the point \bar{r} . Note that the contribution to the tangential component of the magnetic field, due to a surface element shrinking to the singular point $\bar{r} = \bar{r}'$, is equal to $1/2 \hat{n}(\bar{r}) \times \bar{J}_S(\bar{r})$, as in the case of infinite sheet of planar current [30, p. 251]. This contribution was taken into consideration when evaluating the surface integral in Eqn. (2.40).

For numerical evaluation purposes, the vector integral equation (2.42) is resolved into two scalar equations along the orthogonal surface unit vectors \hat{t}_1 and \hat{t}_2 , as illustrated in Fig 2.3, where

$$\hat{t}_1(\bar{r}) \times \hat{t}_2(\bar{r}) = \hat{n}(\bar{r}) . \quad (2.43)$$

Noting that $\hat{t}_1 \times \hat{n} = -\hat{t}_2$ and $\hat{t}_2 \times \hat{n} = \hat{t}_1$, the scalar MFIE's can be written as

$$\begin{aligned} \hat{t}_1(\bar{r}) \cdot \bar{J}_S(\bar{r}) &= -2\hat{t}_2(\bar{r}) \cdot \bar{H}^i(\bar{r}) \\ &- \frac{1}{2\pi} \int_S \hat{t}_2(\bar{r}) \cdot [\bar{J}_S(\bar{r}') \times \nabla' g(\bar{r}, \bar{r}')] dS', \bar{r} \in S \end{aligned} \quad (2.44)$$

and

$$\begin{aligned} \hat{t}_2(\bar{r}) \cdot \bar{J}_S(\bar{r}) &= 2\hat{t}_1(\bar{r}) \cdot \bar{H}^i(\bar{r}) \\ &+ \frac{1}{2\pi} \int_S \hat{t}_1(\bar{r}) \cdot [\bar{J}_S(\bar{r}') \times \nabla' g(\bar{r}, \bar{r}')] dS', \bar{r} \in S. \end{aligned} \quad (2.45)$$

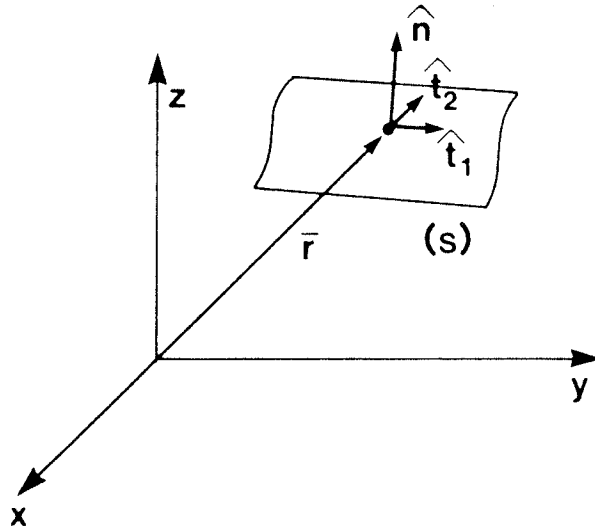


Figure 2.3: Geometry Pertaining to MFIE

Once the surface current density \bar{J}_s and the current intensity I are determined from the corresponding integral equations (2.37), (2.38), (2.44) and (2.45), the field quantities can be directly evaluated with the aid of Eqns. (2.33) and (2.40).

2.4 NUMERICAL SOLUTION

The integral equations (2.38), (2.44) and (2.45) can be solved numerically by the moment method. Harrington [8] has given an excellent general introduction to the method. A brief outline of the method follows.

The moment method applies to a general linear-operator equation

$$Lf = e, \quad (2.46)$$

where f is an unknown response, e is a known excitation, and L is a linear operator (an integral operator in the present case). The unknown function f may be expanded as a sum of basis functions f_j as

$$f = \sum_{j=1}^N \alpha_j f_j. \quad (2.47)$$

A set of equations for the coefficients α_j are then obtained by taking the inner product of equation (2.46) with a set of weighting functions $\{w_i\}$

$$\langle w_i, Lf \rangle = \langle w_i, e \rangle, \quad i = 1, \dots, N. \quad (2.48)$$

Due to the linearity of L, Eqn. (2.47), when substituted for f yields

$$\sum_{j=1}^N \alpha_j \langle w_i, Lf_j \rangle = \langle w_i, e \rangle, \quad i = 1, \dots, N. \quad (2.49)$$

This equation can be written in the matrix notation

$$[G][I] = [E] \quad (2.50)$$

where

$$G_{ij} = \langle w_i, Lf_j \rangle \quad (2.51)$$

$$I_j = \alpha_j \quad (2.52)$$

$$E_i = \langle w_i, e \rangle. \quad (2.53)$$

The solution is then

$$[I] = [G]^{-1}[E]. \quad (2.54)$$

For the solution of equations (2.38), (2.44) and (2.45) the inner product is generally defined as

$$\langle f, g \rangle = \int_S f(\bar{r})g(\bar{r}) dS \quad (2.55)$$

where the integration is made over the structure surface.

The selection of a set of basis functions $\{f_j\}$ is very important for an efficient and accurate solution. References [8, pp. 3-20] and [9, pp. 10-25] provide very good summaries of various possible weighting functions $\{w_i\}$ and basis functions $\{f_j\}$. The choice of

weighting functions $\{w_i\}$ classifies the specializations of (2.51). When $w_i = f_i$, the procedure is known as Galerkin's method, while in the least-square approximation one selects $w_i = Lf_j$. In most applications the weighting functions w_i are chosen as a set of delta functions

$$w_i(\bar{r}) = \delta(\bar{r} - \bar{r}_i) \quad (2.56)$$

with $\{\bar{r}_i\}$ being a set of points on the conducting surface. The result is a point sampling of the integral equations known as the collocation method of solution.

Solution of the matrix equations is typically accomplished via inversion or elimination, and sometimes by iterative techniques. The relative merits of these approaches may be found in the discussions appearing in [7, pp. 150-303]. In the next Chapter the moment method will be employed to evaluate the efficiency of the EFIE and MFIE for antenna and scattering problems.

Chapter III

APPLICATIONS

In the previous Chapter, the formulations of scattering or antenna problems in terms of the EFIE and MFIE were reviewed, and the numerical method to approximate the unknown currents was described. These integral equations and the moment method can now be combined as a complete solution procedure. Figure 3.1 illustrates the general structure of a program, similar to the NEC, which analyzes the electromagnetic responses of scatterers and antennas. Generally, setting up the elements of the structure matrix (based on the input geometry data) is the most complicated step in the whole solution process. It requires expanding the current elements either along wires or tangential to patch surfaces or in some cases, the combination of wires and patches. After the structure matrix, current vector, and excitation vector are set up, the solution for the current follows from standard techniques. Many methods are available to solve the matrix equation $[G] [I] = [E]$. Among the solution methods, the LU-factorization and the Gauss elimination are the most popular ones. Once the unknown currents on the segments or patches have been solved, then it is straight forward to calculate the scattered or radiated fields.

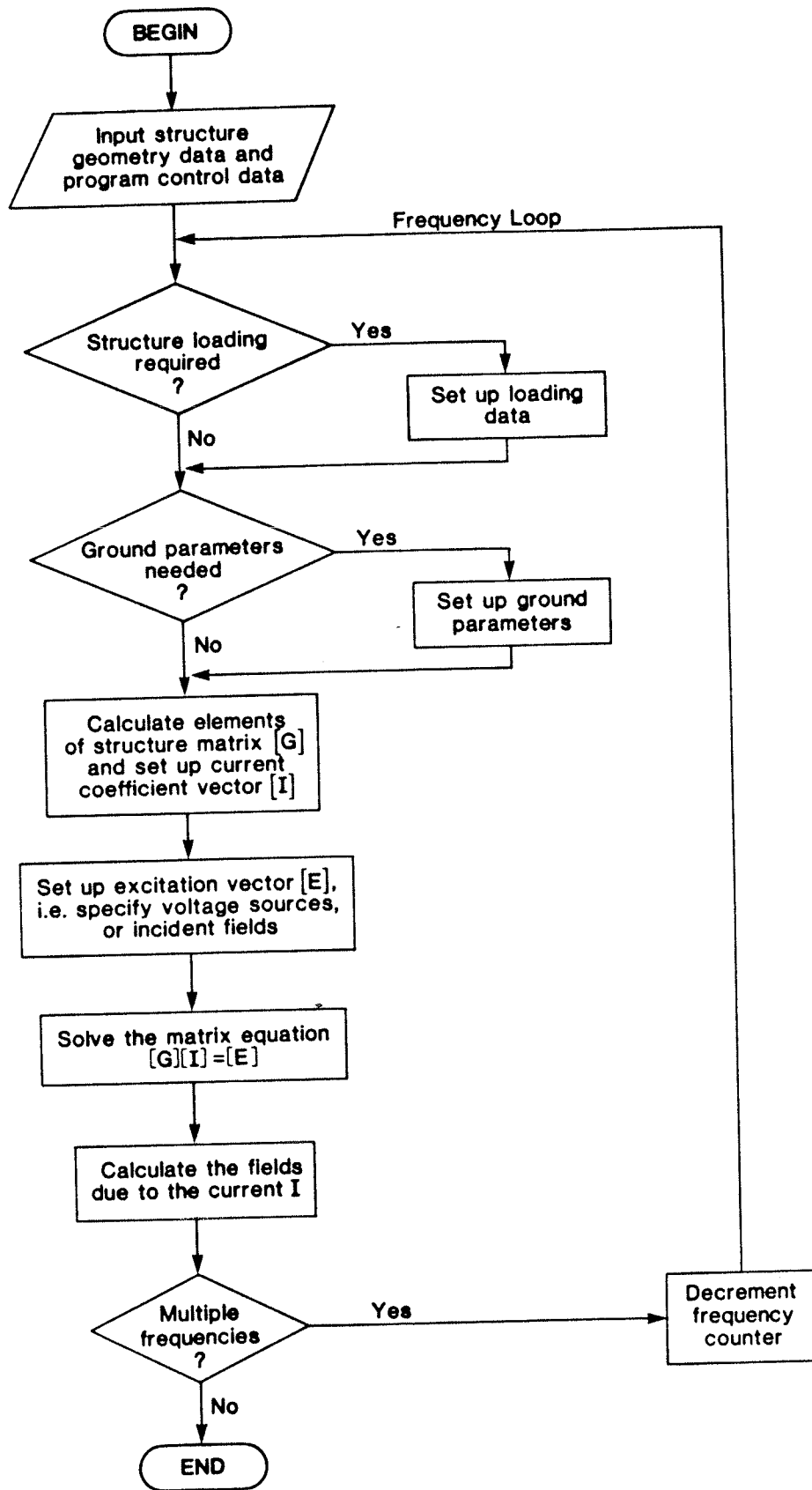


Figure 3.1: Block Diagram of the Overall Structure of an Electromagnetic Response Analysis Program

3.1 MODELING METHODOLOGY

In order to apply the moment method to solve scattering or antenna problems, the structure of the object being evaluated must be modeled properly. Two of the simplest and most basic devices for modeling structures are short straight segments for wires and flat patches for surfaces. The wire-grid modeling of conducting surfaces has previously been used with varying success [22] and [7, pp. 210-232]. A structure can be modeled as a combination of wire segments and flat patches, provided the patches are contiguous and closed. Proper choice of the segments and patches for a scatterer or an antenna determines the accuracy of the results. For a given problem, the knowledge of proper modeling schemes plays an important role in constructing the appropriate input structure geometry. A survey of literature [7, 8, 12, 22] reveals that there is no rule of thumb which can be applied to the modeling of generalized structures. Some useful guidelines, however, have been extracted from the literature and from experience gained while using the NEC. The following two sections outline the modeling methodology for both wires and surface patches.

3.1.1 Wire Modeling

Wire modeling is very easy to apply because of the simplicity of its structure. A wire segment is defined by the coordinates of its two end points and its radius. When using wire modeling, many factors may affect the accuracy of a numerical solution. Factors which are

associated with a change in electrical frequency are grouped under electrical considerations and the remaining factors under geometrical considerations. Geometrical factors will be described initially, followed by a discussion of electrical factors.

In wire modeling, geometrical considerations define a collection of some important factors which will affect the computed results if not followed properly. A wire antenna or any wire-based object must be modeled with strings of wire segments along the paths of the conductors. Segments which are electrically connected must have coincident end points. If segments intersect at points other than their ends, an unpredicted solution may result. In general, wire segments can intersect with each other at any angle. However, severe errors may result if the angle of intersection is so small as to place the observation point on one wire segment within the volume of another wire segment.

The major electrical consideration in wire modeling is the segment length (ℓ), which is relative to the wavelength of the problem being evaluated. In general, the greater the number of segments per wavelength, the better the accuracy of the solution. However, increasing the number of segments per wavelength will result in greater CPU time and a larger memory requirement. One method of compromising is to use variable segment lengths. Longer segments may be used to simulate wires with no abrupt changes, while shorter segments are needed to model critical regions, such as a sharp corner. Nevertheless, extremely short segments should be avoided since they may lead to numerical inaccuracy in the current expansions [12].

The ratio of the segment length (ℓ) to the wire radius (r), ℓ/r , is another electrical factor which will strongly affect the computed results. A small value of ℓ/r may result in extraneous oscillations in the solution. In particular, the application of a small ℓ/r ratio at a wire bend may result in the centre of one segment falling within the radius of the other segment. This in turn leads to severe computational errors.

In addition to modeling wire objects, wire segments can be employed to model closed conducting surfaces. Intuitively, the differences in the electromagnetic properties between a solid, perfectly conducting object and its wire-grid replica can be made to be arbitrarily small as the wire-grid density is increased. Also, the use of wire modeling allows a single wire grid to represent both surfaces of a thin conducting plate. The current on the grid will be the sum of the currents that would flow on opposite sides of the plate. While information about the currents on the individual surfaces is lost, the wire grid will yield the correct radiated fields. Figure 3.2 shows an application of a wire grid to model a sphere.

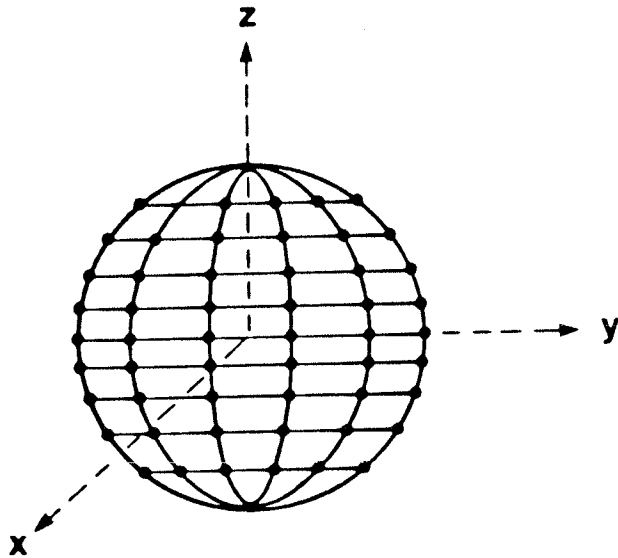


Figure 3.2: Modeling of a Sphere with Wire-grid Approach

3.1.2 Surface-Patch Modeling

Compared with wire modeling, surface-patch modeling is more difficult to set up. A surface patch consists of three elements: the cartesian coordinates of the patch centre, the components of the outward directed, unit normal vector, and the patch area. Figure 3.3 illustrates the components of a surface patch and its geometrical orientation. Similar to wire modeling, factors which affect the accuracy of numerical result can be grouped under either geometrical considerations or electrical considerations.

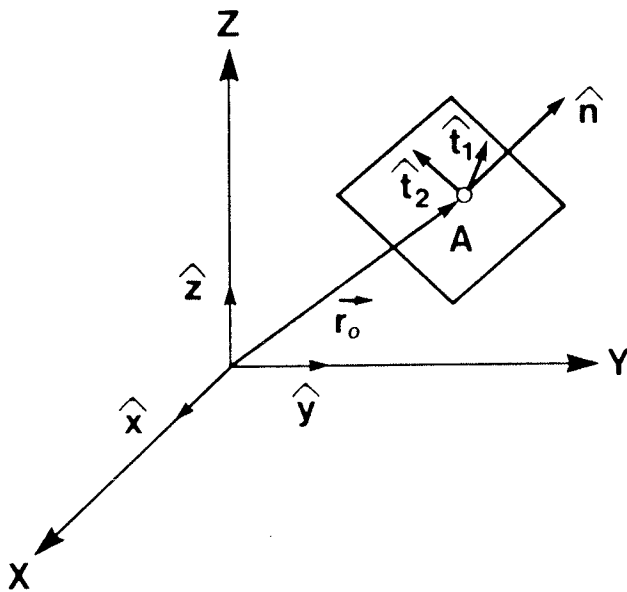
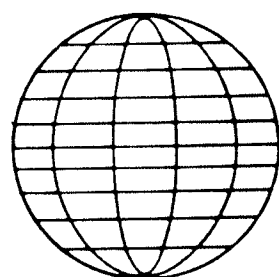


Figure 3.3: Patch Position and Orientation

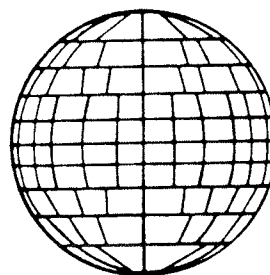
Geometrically, a conducting surface is constructed using multiple, small flat-surface patches covering the entire surface of the object being studied. These patches should conform as closely as possible to the contour of the object's surface, without overlapping. When using surface patches, the total generated surface must be closed because discontinuity at the edges are not taken into account by the NEC program. Thus, if a thin metal structure is modeled, the narrow sides as well as the broad surfaces must be considered. Also, the parallel surfaces on opposite sides should not be too close, or severe numerical errors may occur. In such a case, wire-grid modeling may be more appropriate.

Although the shape of the patch is not required in numerical calculations, very long and narrow patches should be avoided when

subdividing the surface of a structure. In surface-patch modeling, two methods of modeling an object are available, namely uniform segmentation and variable segmentation. Figure 3.4 illustrates the application of these schemes to modeling of a sphere. In the uniform segmentation case an equivalent number of divisions are employed in the azimuthal axis. This uniform division results in all patches having equal areas but with long and narrow patches near the equator. In the variable segmentation method, however, the number of divisions in the azimuth is increased toward the equator so that the patch length and width are kept approximately equal. Burke and Poggio [11, p. 9] studied the differences between these two modeling schemes, and their results indicated that much better agreement with experiment was obtained when using the variable segmentation scheme.



Uniform Segmentation



Variable Segmentation

Figure 3.4: Modeling of Spheres Using Uniform and Variable Segmentation Schemes

The only electrical consideration to deal with in surface-patch modeling is the patch area, which is measured in wavelength squared. Similar to the segment length in wire modeling, large patches may be

applied to model large, smooth surfaces, whereas small patches are needed in the area where the radius of curvature is small. Also, for critical regions, like edges, where the magnitude of the current may vary rapidly, smaller patches should be used for obtaining accurate solutions.

When modeling a complex structure with features not previously encountered, accuracy may be checked by comparison with reliable experimental data if available. Alternatively, an optimal model of a structure can be obtained by varying the segment length, patch density, or wire radius and observing the effect on the results. Some variation in the output data will always be found. A large variation would indicate that the solution has not converged and more segments or patches should be added. In general, a model will be valid over a range of frequencies. Nevertheless, for frequencies beyond the upper limit of a particular model, a new set of geometrical parameters must be employed with finer segmentations.

Although selecting a sufficient number of wire segments or patches generally gives satisfactory results, it does not necessarily mean that by increasing their number the solution will converge. This instability may be caused by i) the inappropriate modeling for the object being considered, ii) an ill conditioned matrix due to internal resonances, or iii) numerical round off errors for a large matrix. One of the objectives of this study is to analyze the performance and limitations of various modeling schemes by applying the moment method to antenna and scattering problems with varying parameters.

3.2 APPLICATION TO SCATTERING PROBLEMS

For the purpose of evaluating the performance and limitations of the moment method, the NEC has been applied to scattering problems of conducting spheres. To determine the accuracy of the computed data, the numerical results were compared with analytical solutions expanded in terms of the spherical wave functions. The comparison was made for the radar cross-section of spheres of various radii ranging from $ka = 2$ to 12. Specifically, for a plane wave traveling along the z -axis as shown in Fig. 3.5, the E- and H-plane radar cross-sections were obtained by specifying $\phi = 0$ (x - z plane) and $\phi = \pi/2$ (y - z plane), respectively. For completeness, both wire-grid and surface-patch modeling schemes were studied. Note that in general, however, the surface-patch modeling is more suitable for volumetric objects.

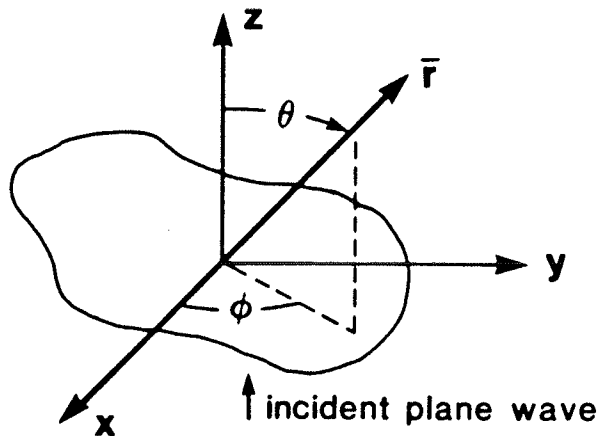


Figure 3.5: Scattering Problem Geometry

3.2.1 Analytical Method

Scattering by conducting spheres has been investigated previously by Harrington [1, p. 295] and Wait [21]. For a plane wave traveling along the z-axis (Fig. 3.5), the far-zone scattered electric field components are given as

$$E_{\theta}^S = -j \frac{E_0}{kr} e^{-jkr} S_1(\theta, \phi) \quad (3.1)$$

$$E_{\phi}^S = j \frac{E_0}{kr} e^{-jkr} S_2(\theta, \phi) \quad (3.2)$$

where

$$S_1(\theta, \phi) = \cos \phi \sum_{n=1}^{\infty} j^n \left[a_n \frac{d}{d\theta} P_n^1(\cos \theta) + b_n \frac{P_n^1(\cos \theta)}{\sin \theta} \right] \quad (3.3)$$

$$S_2(\theta, \phi) = \sin \phi \sum_{n=1}^{\infty} j^n \left[a_n \frac{P_n^1(\cos \theta)}{\sin \theta} + b_n \frac{d}{d\theta} P_n^1(\cos \theta) \right] \quad (3.4)$$

$$a_n = -\frac{c_n \hat{J}'_n(ka)}{\hat{H}_n^{(2)'}(ka)} \quad (3.5)$$

$$b_n = -\frac{c_n \hat{J}_n(ka)}{\hat{H}_n^{(2)}(ka)} \quad (3.6)$$

$$c_n = \frac{j^{-n}(2n+1)}{n(n+1)} \quad (3.7)$$

and E_0 is the magnitude of the incident electric field, P_n is the Legendre polynomial of order n [1, p. 465] and \hat{J}_n , \hat{H}_n are the Riccati

Bessel and Hankel functions of order n [1, p. 464]. The radar cross-section is dependent on the elevation and azimuthal angles θ and ϕ , respectively (Fig. 3.5), and is given by the expression [1, p. 116]

$$\sigma(\theta, \phi) = \lim_{r \rightarrow \infty} 4\pi r^2 \left| \frac{E^S}{E_0} \right|^2 \quad (3.8)$$

which simplifies to

$$\sigma(\theta, \phi) = \frac{4\pi}{k^2} \left[|S_1(\theta, \phi)|^2 + |S_2(\theta, \phi)|^2 \right]. \quad (3.9)$$

Thus the normalized radar cross-section is

$$\frac{\sigma}{\pi a^2} = \frac{4}{(ka)^2} \left[|S_1(\theta, \phi)|^2 + |S_2(\theta, \phi)|^2 \right]. \quad (3.10)$$

3.2.2 Wire-Grid Approach

When using the NEC with the wire-grid approach, a structure is modeled by electrically-small wire segments. To reduce the computational cost and the amount of matrix storage [12], when generating the input structure geometrical data, 1/8 symmetry was employed. A data preparation program was developed to interface with the NEC input processor. This program generates the wire-oriented geometry for an octant of the surface of a sphere as shown in Fig. 3.6. The complete sphere is constructed by i) reflecting the octant in the x - z plane to form a quadrant, ii) reflecting the quadrant in the x - y plane to form a hemisphere, and finally iii) reflecting this hemisphere in the y - z plane to complete the sphere.

To obtain the radar cross-section using the NEC, an incident plane wave traveling along the z -axis was used as the incident field.

The output from the NEC was in the form of σ/λ^2 dB. In order to be consistent with the analytical solution, the normalized radar cross-section was calculated with the following relation [1, p. 116]

$$\frac{\sigma}{\pi a^2} = \frac{4\pi}{(ka)^2} 10^{.1 \left(\frac{\sigma}{\lambda^2} \right) \text{dB}} \quad (3.11)$$

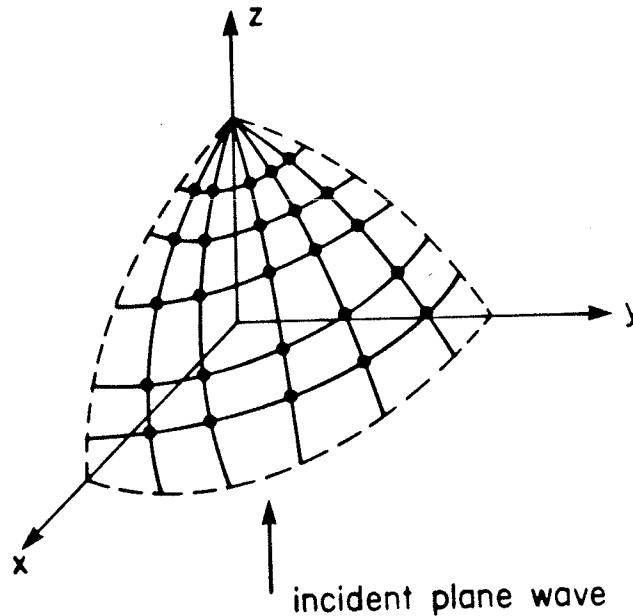


Figure 3.6: Wire Segmentation Scheme

A sphere as shown in Fig. 3.6 was modeled with 20 segments along the equator and a total of 288 segments spaced over the entire surface. The radar cross-sections of this sphere have been calculated for values of ka ranging from 0.75 to 3.0. This corresponds to a range of segment lengths from 0.0375λ (when $ka = 0.75$) to 0.15λ (when $ka = 3$). The electrical length of the wire segments was varied to study the effect of this parameter on the accuracy of the numerical solution. In order to accomplish this, instead of varying the radius (a) of the sphere, the wave number (k) was altered.

For ka less than 2.0 reasonable agreement was observed between the exact analytical and numerical solutions. The deviation, however, became drastically greater as ka increased from 2.0 to 3.0. These results indicate that useful radar cross-section can be calculated by wire-grid modeling, provided that the number of segments per wavelength is greater than 10.

As mentioned earlier in this Chapter, the wire radius (r) is relative to the segment length (l), and the ratio l/r is an important parameter in the wire-grid modeling. To visualize the effect of this parameter on numerical accuracy, calculations were carried out with $ka = 2$ and $l = 0.1\lambda$ for a uniform wire radius ranging from 0.0016λ to 0.016λ . This corresponds to l/r varying from 62.5 to 6.25. Figures 3.7 to 3.10 illustrate that the accuracy of the numerical solution depends heavily upon the proper value of l/r . As shown in Fig. 3.7, the best agreement between the numerical and analytical solutions are observed when $r = 0.0095\lambda$ and $l/r = 10.5$. These results point out that in order to obtain accurate numerical solutions to scattering problems, the ratio l/r must be greater than 8, but much less than 30.

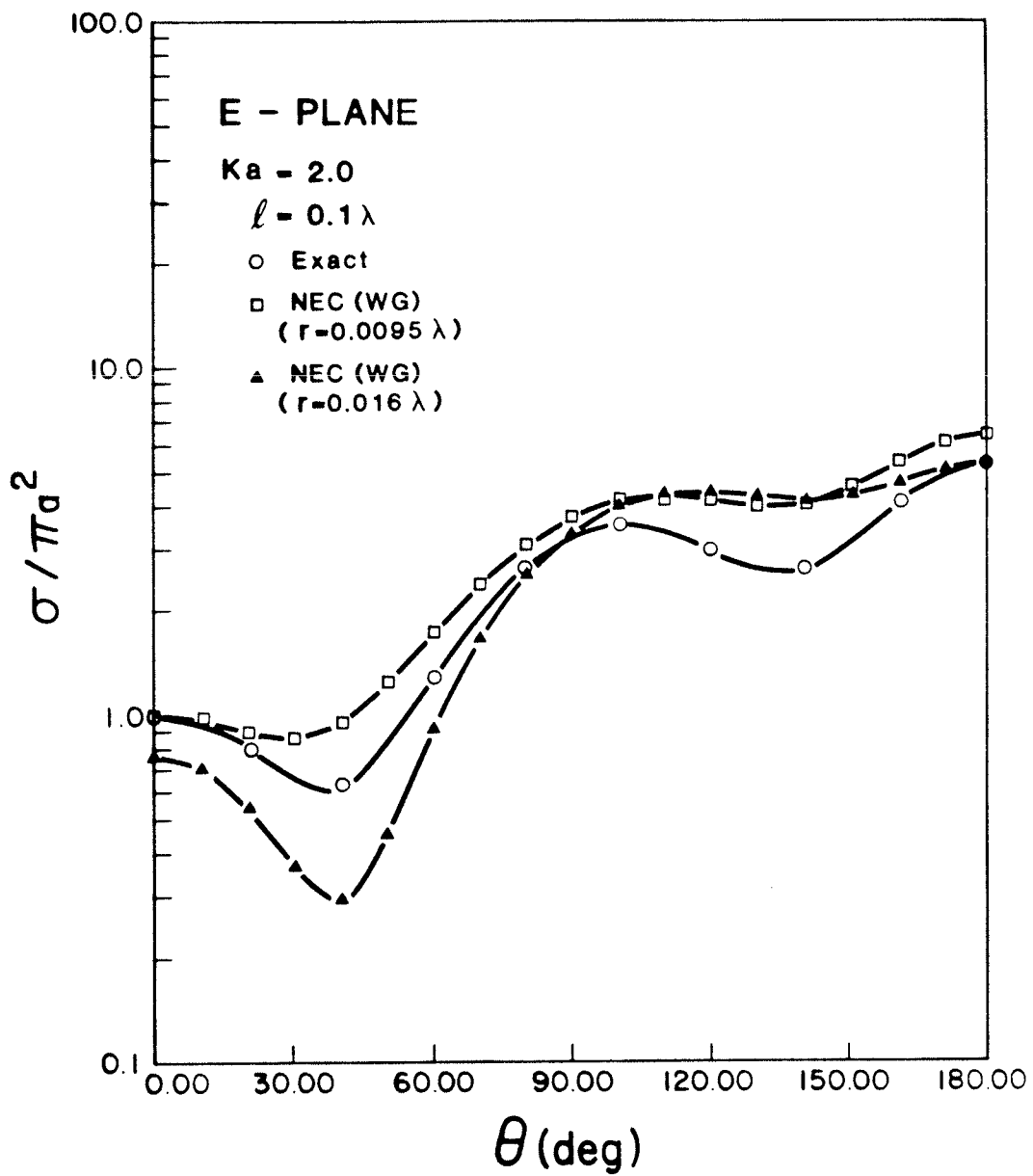


Figure 3.7: Comparison (A) of E-plane Scattering Cross-section with Wire-grid Model for Different Wire Radius

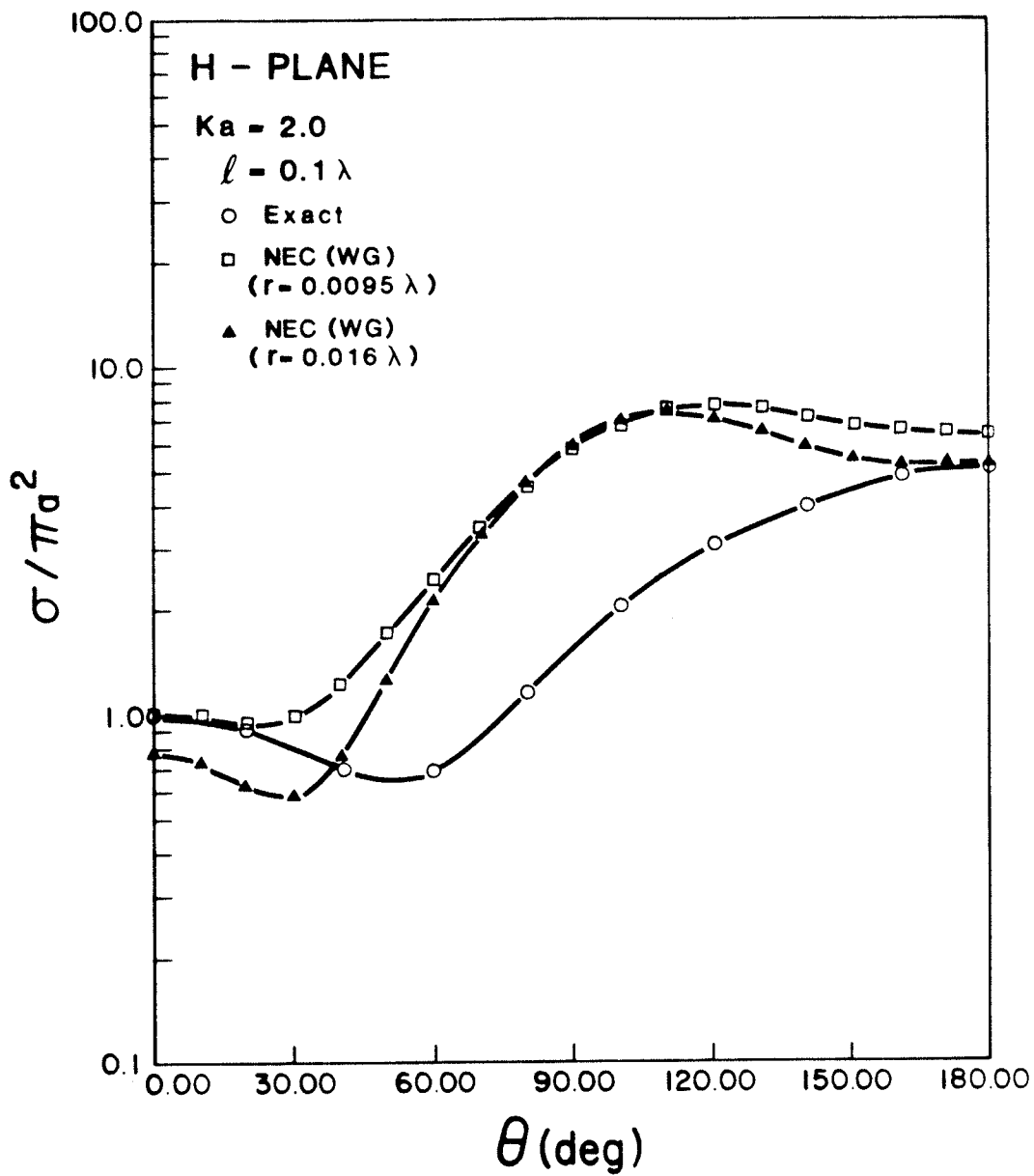


Figure 3.8: Comparison (A) of H-plane Scattering Cross-section with Wire-grid Model for Different Wire Radius

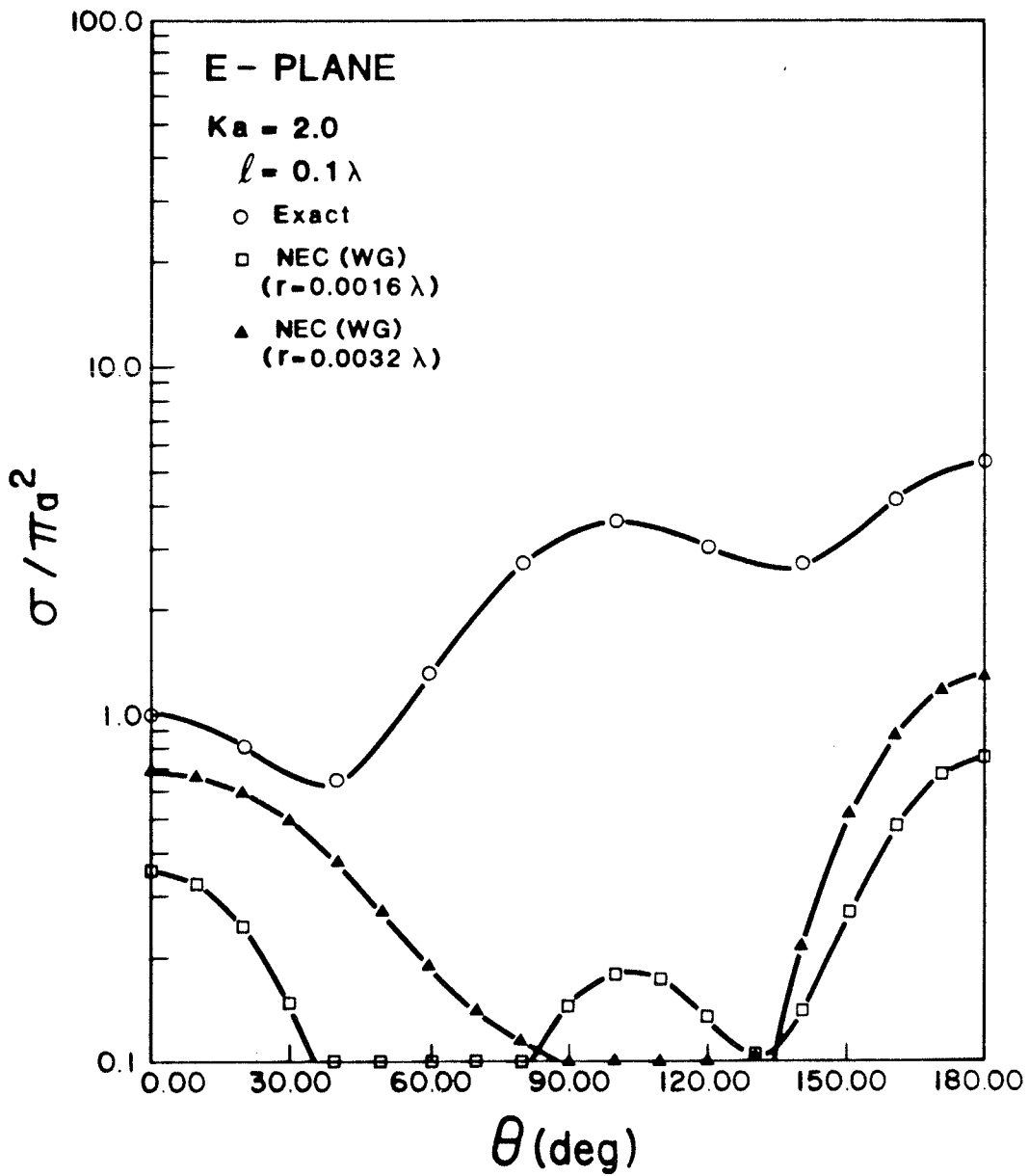


Figure 3.9: Comparison (B) of E-plane Scattering Cross-section with Wire-grid Model for Different Wire Radius

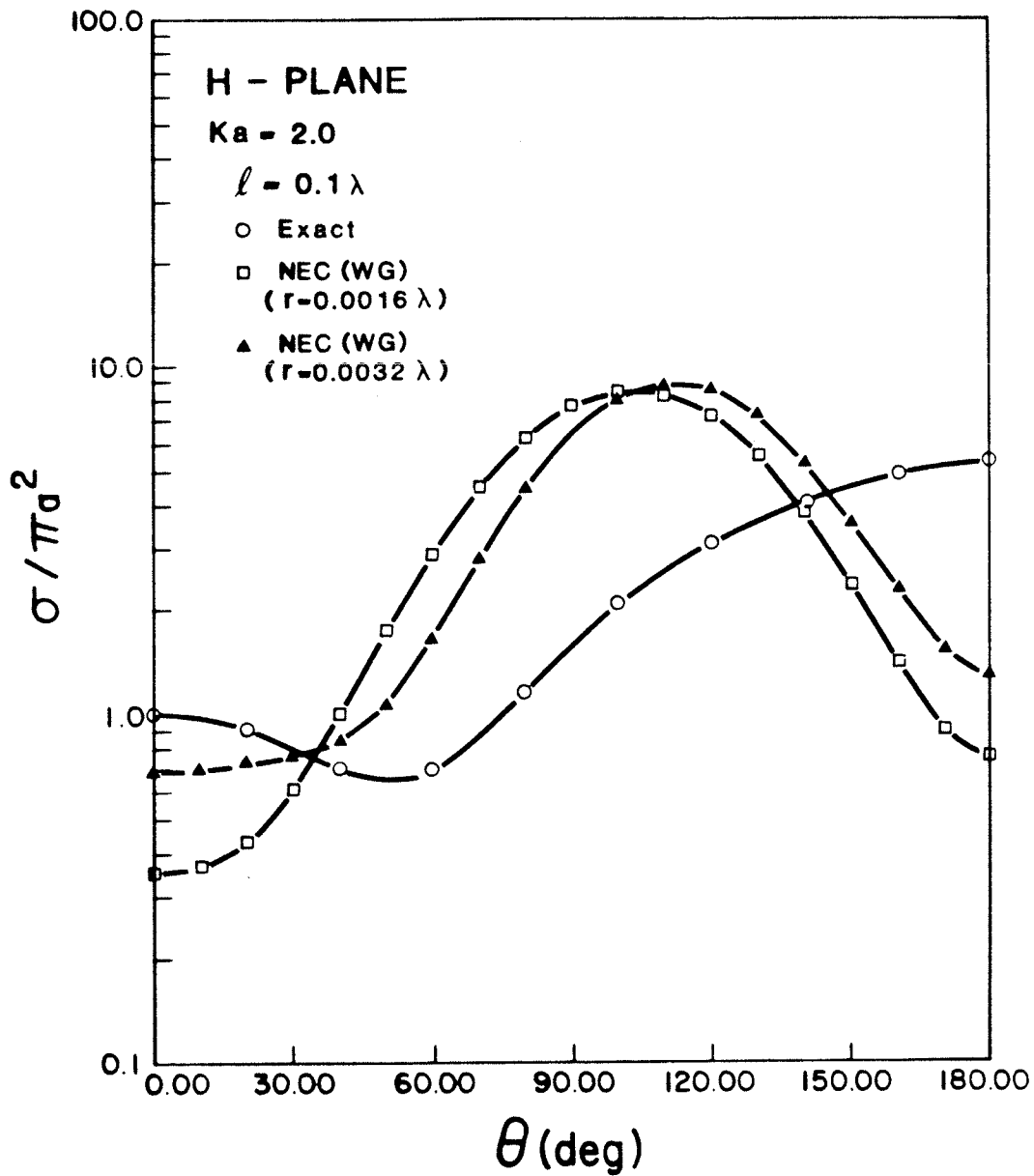


Figure 3.10: Comparison (B) of H-plane Scattering Cross-section with Wire-grid Model for Different Wire Radius

3.2.3 Surface Patch Approach

When using surface patches, the structure being evaluated can be modeled by electrically-small and arbitrarily shaped flat patches. As in the wire-grid case, $1/8$ symmetry was employed and the octant shown in Fig. 3.11 was generated by a data preparation program. The complete sphere was created by applying successive reflections in the x - z , x - y , and y - z planes, respectively.

Note that for the wire-grid case, no wires should coincide with the axis of reflection and that wires intersecting this axis should do so at, or near right-angles. Also, for the surface-patch case, no overlapping patches are permitted along the reflecting axis, and patches along this axis should be complete.

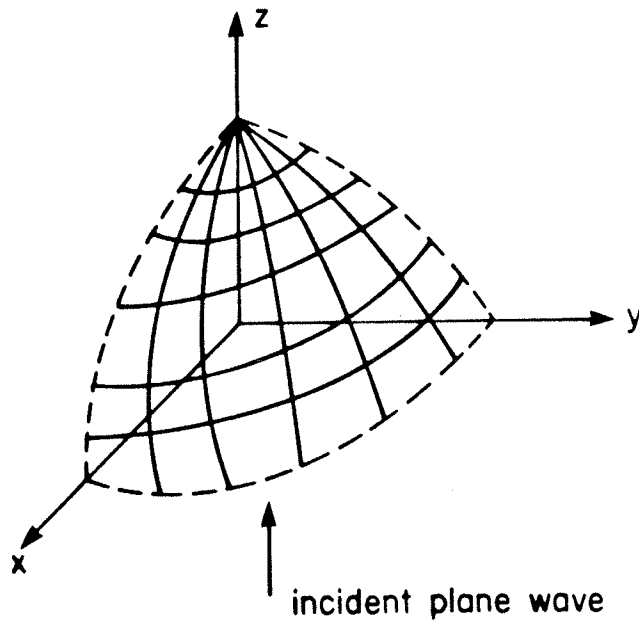


Figure 3.11: Surface Patch Segmentation for a Sphere

Using the variable segmentation scheme, a sphere as shown in Fig. 3.11 was modeled with 256 patches, the maximum area of a patch being about $0.049 \lambda^2$. Calculations were carried out for ka ranging from 2 to 12. This corresponds to a variation from 200 to 5 patches per wavelength squared. Only the results for $ka = 4$ and 12.0 are shown for brevity.

Figure 3.12 shows a very good agreement between the analytical and the numerical solutions for the E-plane, and Fig. 3.13 gives an excellent agreement for the H-plane. However, similar to the wire-grid modeling case, the accuracy of the numerical solution deteriorates for $ka > 5$. This effect is best illustrated by Figures 3.14 and 3.15. These results indicate that the accuracy of the numerical solutions for forward scattering seems to be adequate for a wide range of ka values. Beyond 90 degrees ($\theta = 90$ degrees) off the forward direction, the accuracy tends to deteriorate. These results reveal that surface-patch modeling is sufficiently accurate for analyzing scattering from volumetric objects for a wide range of frequencies when the patch area is less than 0.04 wavelength squared.

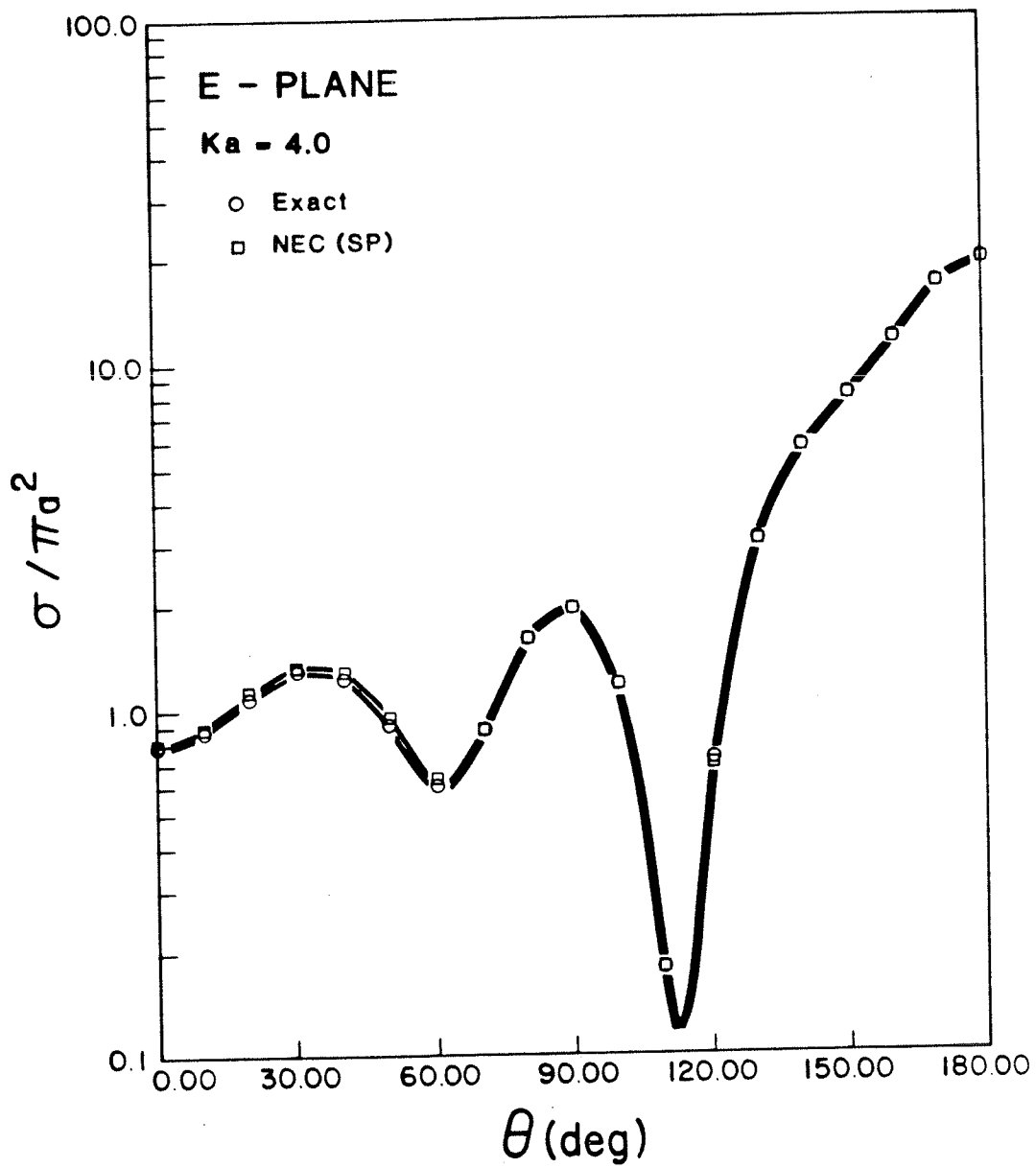


Figure 3.12: E-plane Scattering Cross-section of a Sphere When $Ka = 4$

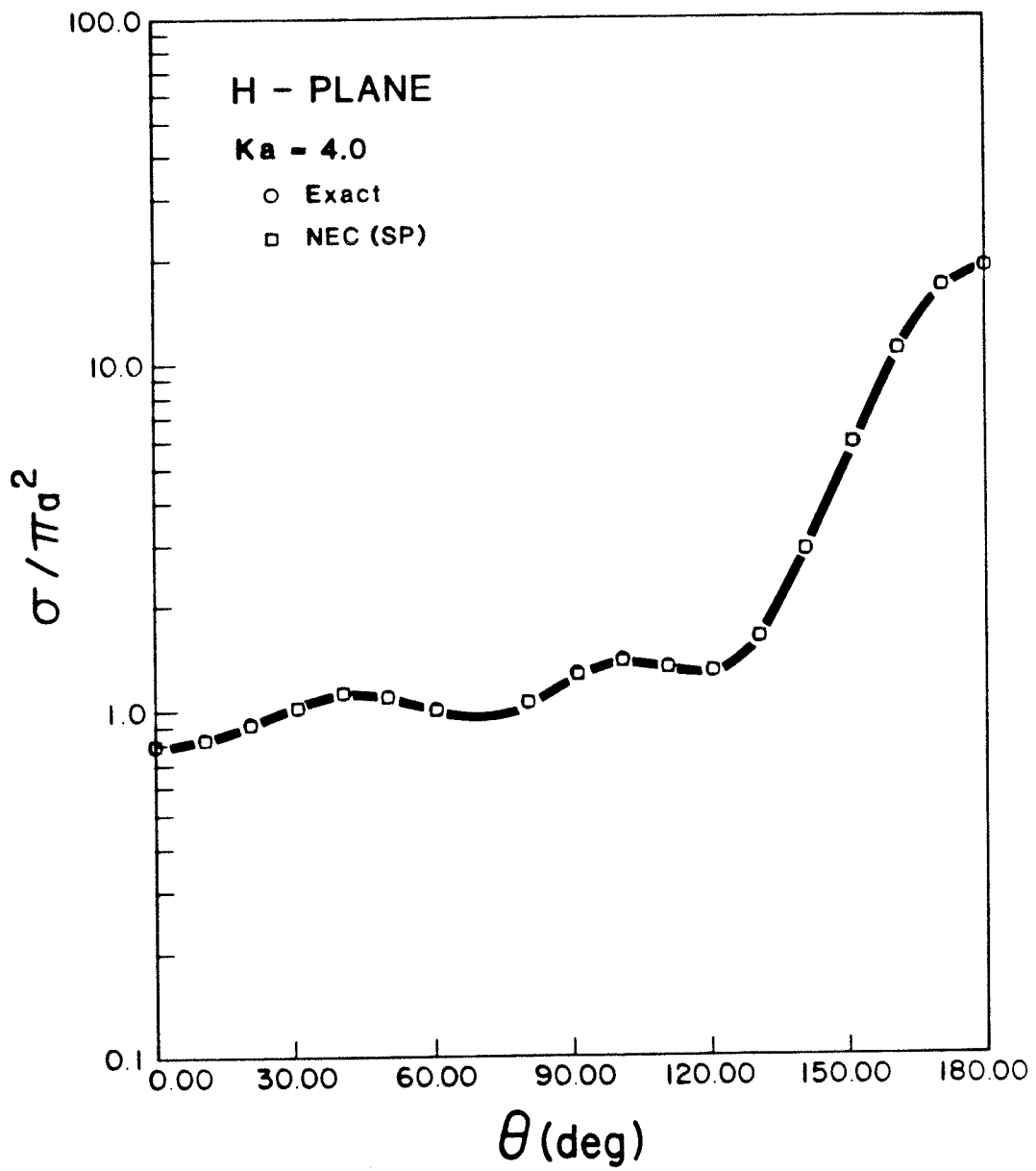


Figure 3.13: H-plane Scattering Cross-section of a Sphere When $Ka = 4$

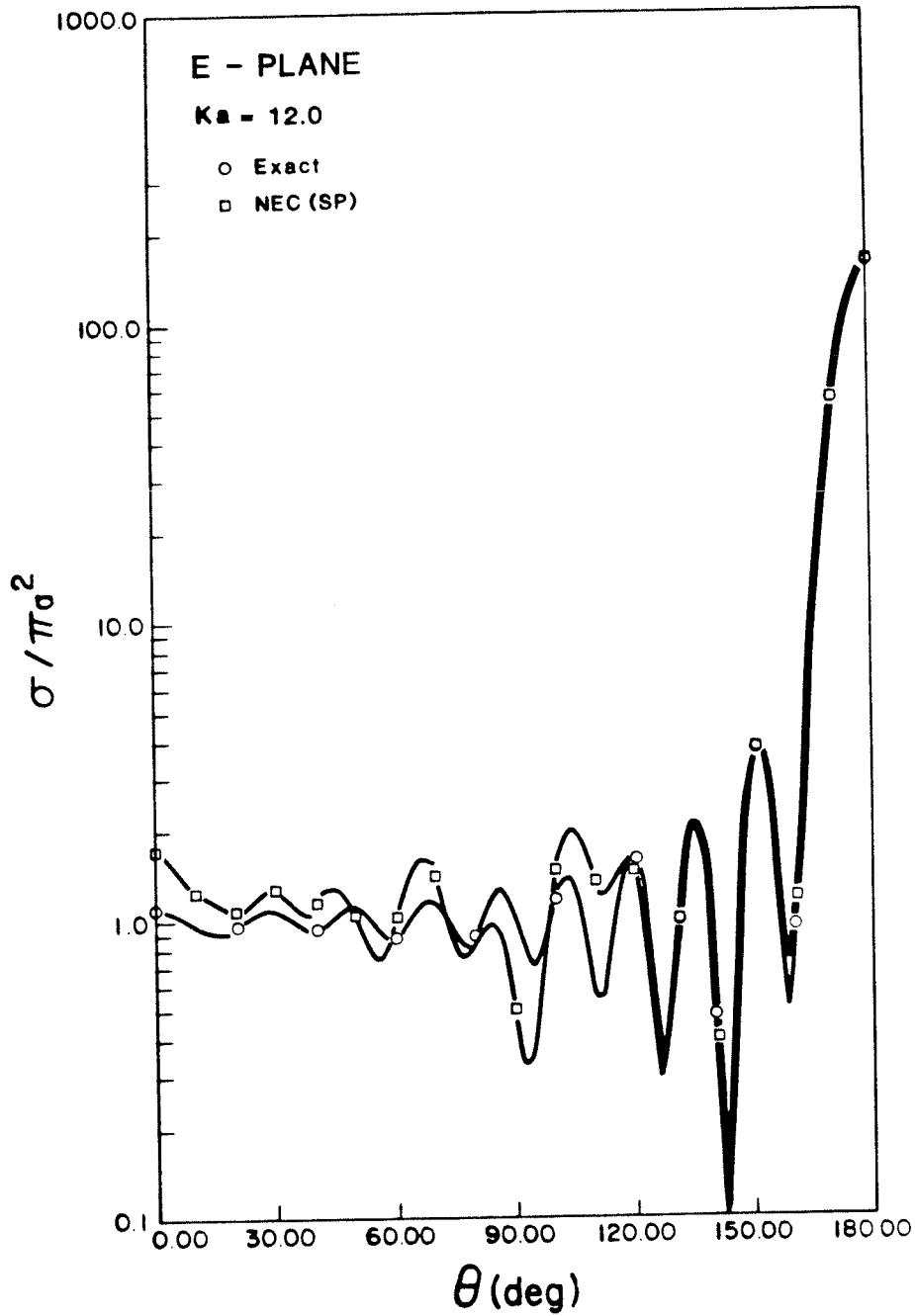


Figure 3.14: E-plane Scattering Cross-section of a Sphere When $Ka = 12$

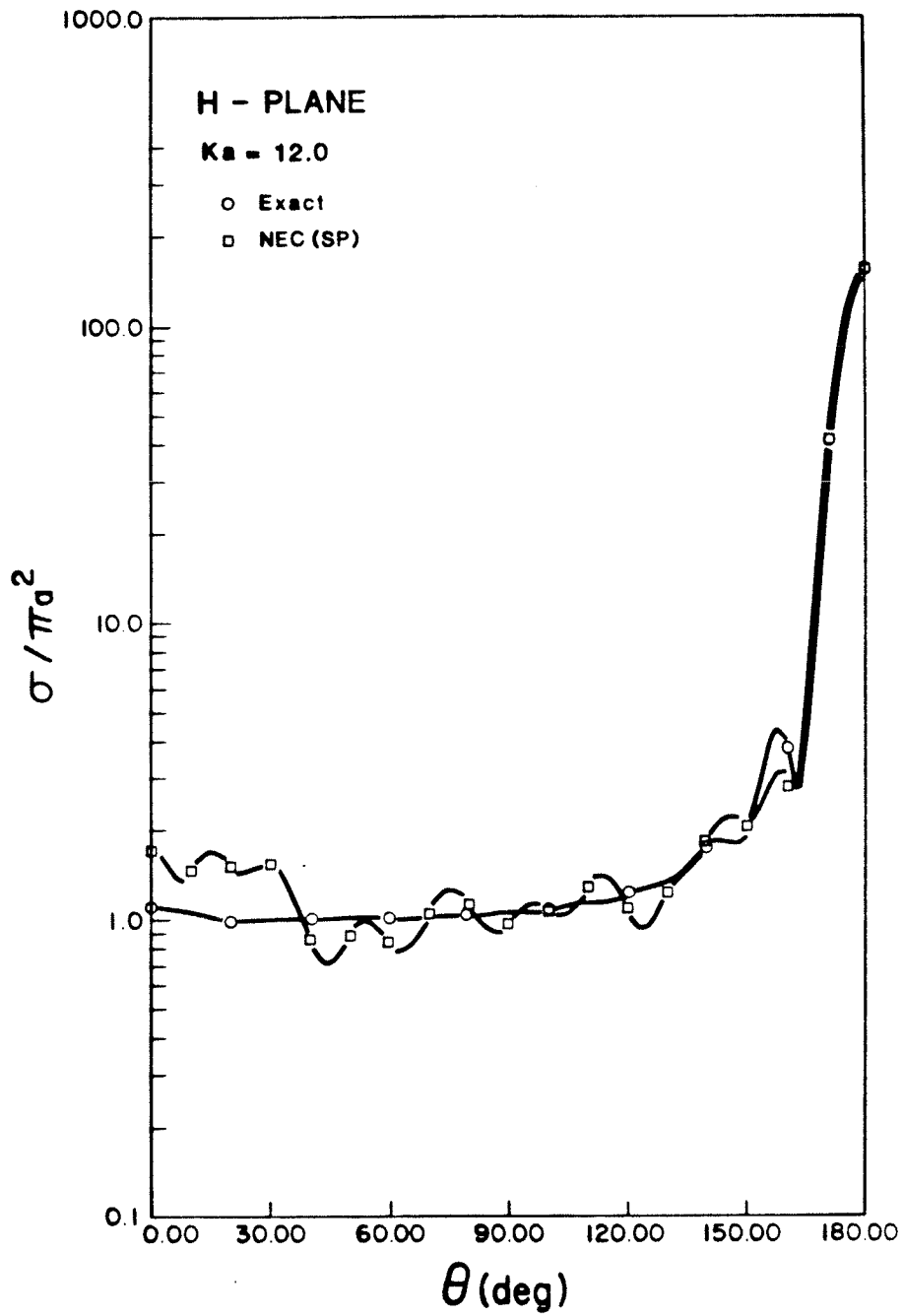


Figure 3.15: H-plane Scattering Cross-section of a Sphere When $Ka = 12$

3.2.4 Comparison of Wire-Grid and Surface-Patch Modeling Schemes

The results from the previous modelings point out that the solution by the surface patches is more stable than that obtained by wire grids for volumetric objects. Numerical accuracy deteriorates slightly when the maximum patch size is larger than 0.04 wavelength squared. For the wire-grid case, however, a small change in the l/r ratio introduces a drastic deviation of the numerical solution from the analytical results.

Figures 3.16 and 3.17 illustrates that surface patches give an excellent agreement between the numerical and analytical solutions. The wire-grid modeling does not provide good results except in the forward and backward direction. This comparison concludes that the surface-patch modeling, in general, is superior to the wire-grid modeling for analyzing volumetric objects. Nevertheless, in the next section, the wire modeling will be applied to practical modeling of a complex wire-structure antenna.

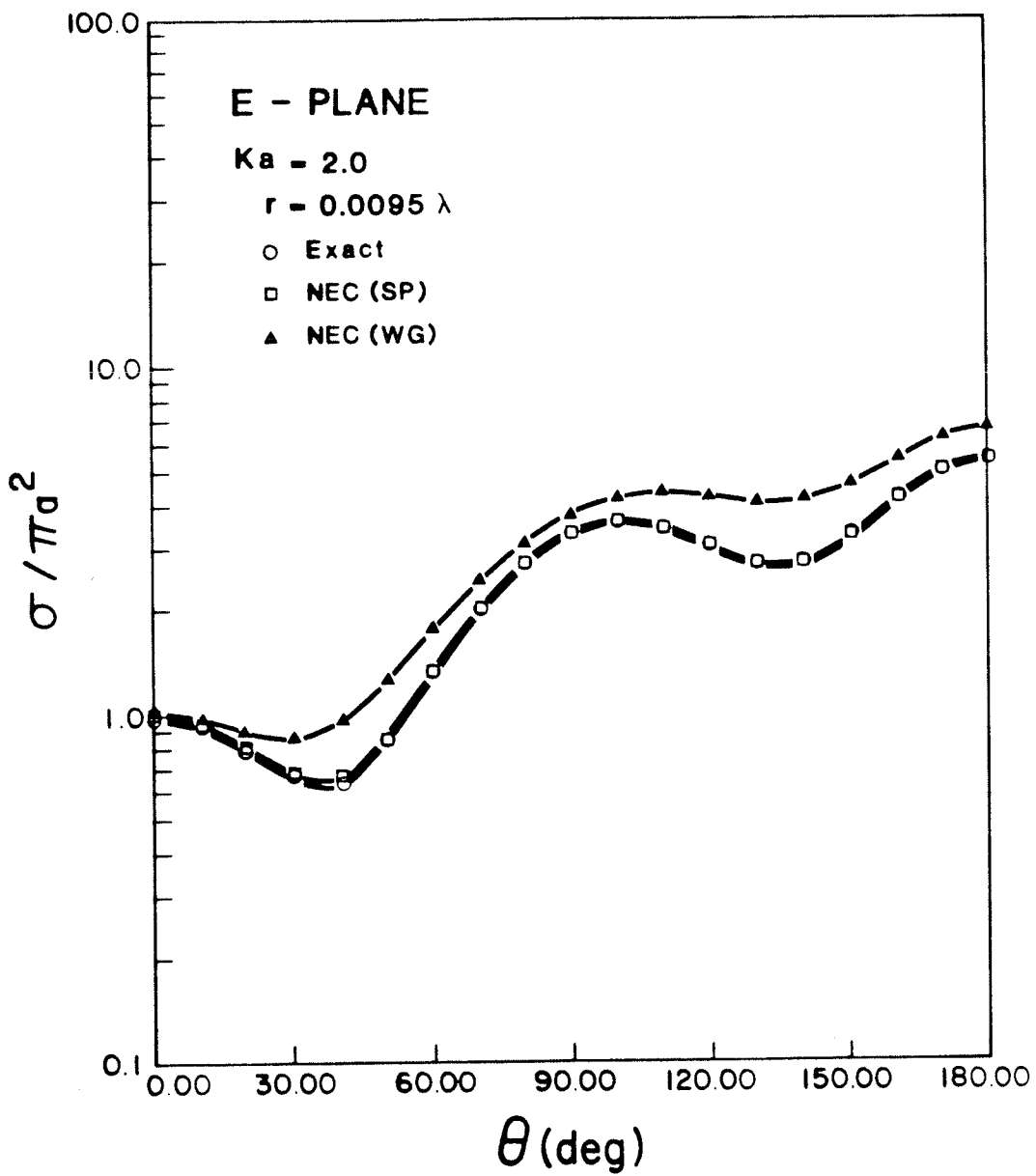


Figure 3.16: Comparison of E-plane Scattering Cross-section using NEC and Analytical Method

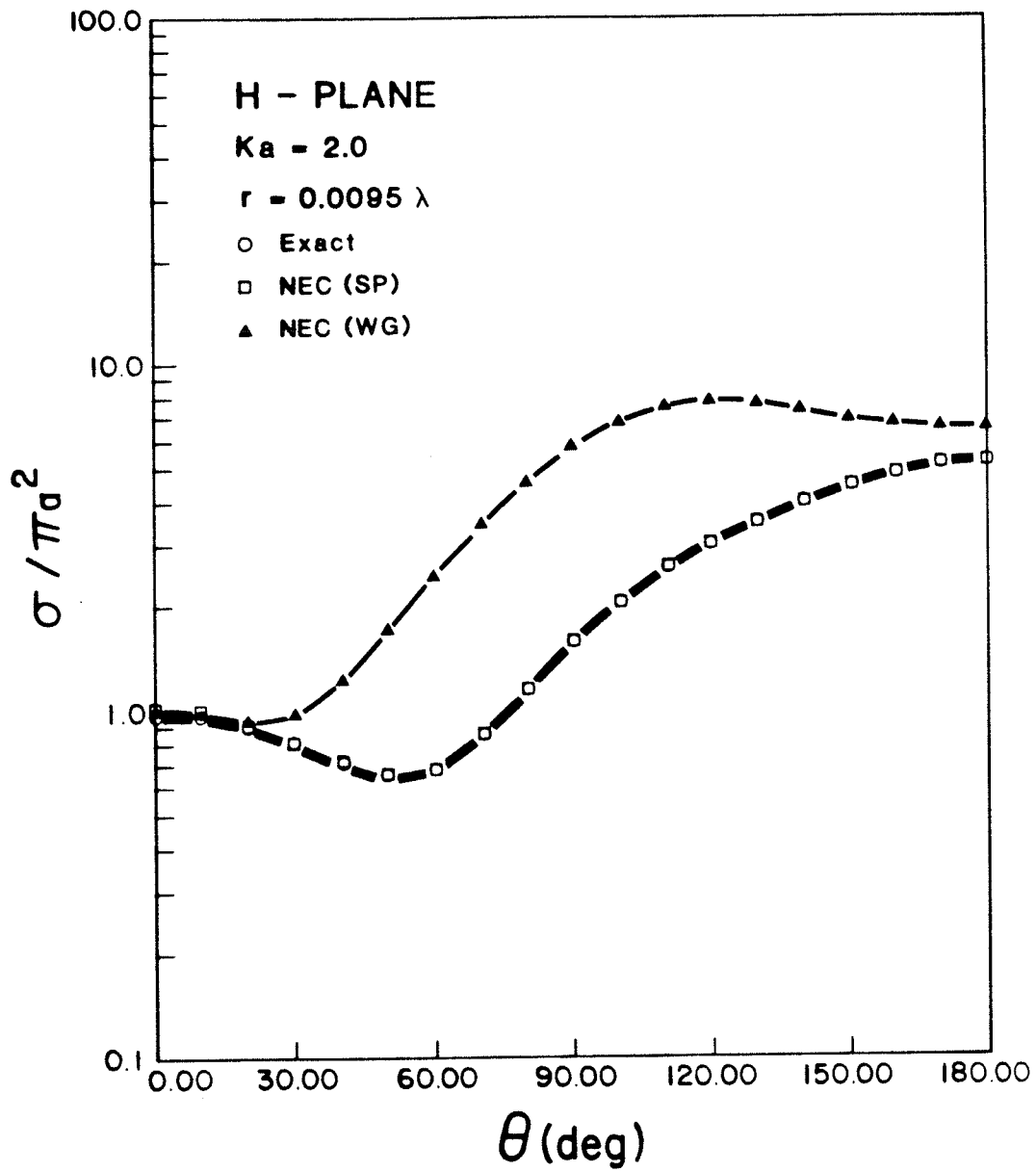


Figure 3.17: Comparison of H-plane Scattering Cross-section using NEC and Analytical Method

3.3 APPLICATION TO WIRE ANTENNAS

When designing an antenna, engineers usually formulate the general structure of the antenna based on previous experience so as to satisfy the required radiation characteristics. However, converting a design into a fully functional antenna with all the required characteristics is an arduous task that often requires at least as much effort as the initial design. The controlling parameters of a new antenna structure can be identified analytically, experimentally or numerically. To identify the parameters by experiment is, in general, expensive and slow. An accurate analytical treatment of a new design is usually a formidable task, if possible at all. With the advent of design workstations and easy-to-use programs, the trend is to study the properties of an antenna numerically.

The application of the moment method to scattering problems as presented in the previous section demonstrates the usefulness of surface-patch modeling for volumetric objects. In this section the wire modeling is applied to a sandwich wire antenna [24, 25] to study its usefulness in wire-structure objects. A feasible numerical model for this sandwich wire antenna based on the moment method is developed, and the effects of different parameters on the radiation characteristics are described.

3.3.1 Sandwich Wire Antenna

A sandwich wire antenna is an undulating centre conductor supported by a dielectric substrate located on the walls of a conducting trough as shown in Fig. 3.18. Rotman and Karas [24, 25] introduced a sandwich wire antenna of sinusoidal shape with a tapered aperture illumination giving a -20 dB sidelobe level. Graham and Dawson [26] developed a planar array with a number of sandwich wire antennas stacked together. This antenna array yielded a sidelobe level of -26 dB. Green and Whitrow [27] gave an approximated analytical solution for sandwich wire antennas with periodic uniform undulations. The theoretical sidelobe level of their solution is of the order of -13 dB regardless of the shape of the undulations. Recently, Aboul-Atta and Shafai [28] gave an approximated analytical treatment for tapered undulations with a sidelobe level below -20 dB. A survey of this literature reveals that an exact analytical solution for a sandwich wire antenna still does not exist, but that a detailed analysis of the antenna properties can be accomplished either experimentally or numerically.

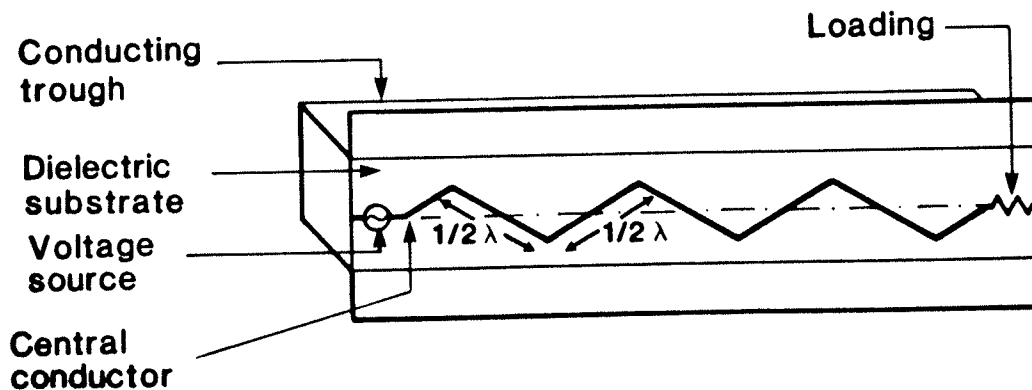


Figure 3.18: Geometry of a Sandwich Wire Antenna

As described earlier, a sandwich wire antenna with periodic uniform undulations yields a radiation pattern with -13 dB sidelobe levels. Rotman and Karas [25] and Aboul-Atta and Shafai [28] have however demonstrated sandwich wire antennas with tapered undulations achieving sidelobe levels below -20 dB. To achieve better sidelobe levels, an appropriate numerical model of the antenna structure should be defined, its parameters varied, and its sidelobe levels compared until an optimal design is found. However, search through a set of possible undulations is expensive and inefficient. Alternatively, an approximated optimal undulation can be synthesized by applying the Taylor's amplitude distribution [31]. Shafai et al [29] have designed a sandwich wire antenna with tapered trapezoidal undulations by this method, and their design is shown in Fig. 3.19.



Figure 3.19: Geometry of a Central Conductor with Tapered Trapezoidal Undulations

Initially, to reduce the matrix dimensions, the supporting dielectric substrate was neglected when modeling the sandwich wire antenna as shown in Fig. 3.18. Nevertheless, for practical antenna

dimensions, a correct modeling of the sidewalls by the surface-patch or wire-grid modeling methods results in a matrix size exceeding 1200 x 1200 elements. The computer storage and time requirements to handle the appropriate matrices of the current distribution exceed the limit of many existing computers. In addition, the roundoff errors due to the manipulation of matrices larger than 300 x 300 are excessive, and the solution accuracy becomes questionable. After extensive analysis, it was found that the current distribution on the central conductor is determined mainly by the shape of the conductor [29]. Useful results can be obtained if either the side walls are modeled appropriately or removed completely. However, neglecting the trough side walls affects the current distribution, primarily in the E-plane. After a careful study, it was determined that the simplified model with the side walls removed yielded the antenna radiation pattern, with reasonable accuracy, in the H-plane.

A sandwich wire antenna as shown in Figure 3.20 has been used to study the effect of the wire segment length on the H-plane radiation patterns. The numerical model is set up by placing the 17.5 period central conductor (Fig. 3.19) $1/4 \lambda$ above a ground plane. With the wire radius selected to be 0.01λ , calculations were carried out at a frequency of 11.0 GHz for the number of segments ranging from 6 to 16 per wavelength. This corresponds to a segment length varying from 0.1667λ to 0.0625λ . Figure 3.21 illustrates that only slight deviations are observed when the segment length is decreased from 0.1667λ to 0.0625λ . In the earlier sections when wire-grid modeling was used to analyze the scattering of a sphere, the accuracy of a

numerical solution was shown to depend heavily on the segment length. The slight deviation in the results of this example reveals that solutions obtained for wire structures are relatively more stable than those obtained for volumetric objects over a wide range of segment length variations. For accurate solutions the average number of segments per wavelength should still be greater than 10.

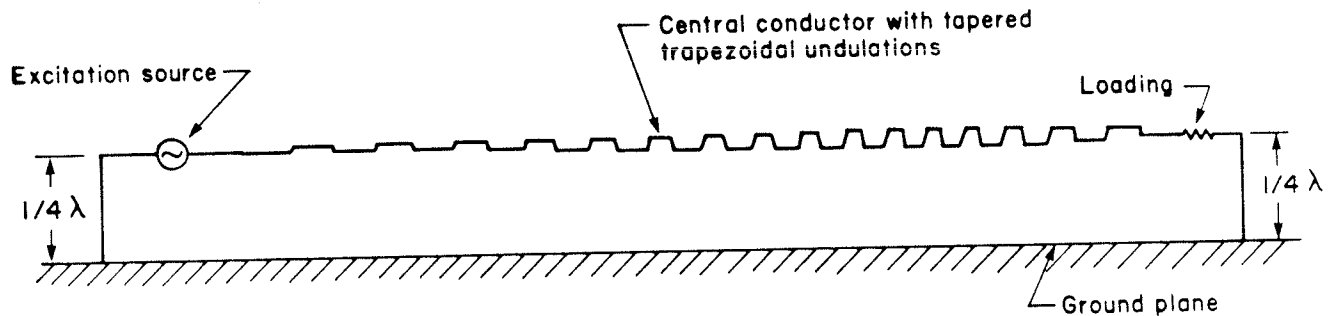


Figure 3.20: Wire Modeling of a Sandwich Wire Antenna with Tapered Trapezoidal Undulations

For a segment length equals 0.0625λ , the calculated H-plane radiation pattern (Fig. 3.22) shows good agreement to the measured data within 30 degree off the main beam. However, beyond 30 degree off the main beam, the deviations become greater. These discrepancies between the calculated and measured patterns are mainly caused by the simplicity of the numerical model assumed for the NEC program. Nevertheless, the calculated radiation pattern provides several useful radiation characteristics such as the main beam width, the sidelobe levels, and the effect of load end reflections.

When wire-grid modeling was applied to model a sphere in the earlier sections, the l/r ratio was shown to be a crucial factor in obtaining accurate solutions. To determine whether the l/r ratio is also critical in the modeling of wire structures, the sandwich wire antenna has been modeled with a constant length of 0.0625λ , but with the wire radius ranging from 0.002λ to 0.02λ . The calculations were carried out at a frequency of 11.0 GHz. Figure 3.23 illustrates that when the l/r ratio is decreased from 6.25 to 3.125, the main beam becomes wider for the same excitation frequency, but the general shape of the radiation pattern remains in a similar form. However, when the l/r ratio is increased from 6.25 to 31.25 as shown in Figure 3.24, not only the main beam becomes narrower, but the shape of the radiation pattern also deteriorates. These deviations indicate that the effects of the l/r ratio for wire structures are in general less significant than those for volumetric objects. For an accurate solution of wire antenna models, the l/r ratio must be between 6 to 20.

Radiation pattern squinting is another radiation characteristic that can be analyzed by using the sandwich wire model. Figure 3.25 illustrates the beam squint as the excitation frequency is increased from 10.0 GHz to 12.0 GHz. This shifting corresponds closely to the experimental data reported by Shafai et al [29]. This beam squinting together with other solutions like beam width, sidelobe level, and effect of load end reflections suggest that the sandwich wire antenna model is a flexible tool for the analysis of other antenna properties. These include the current distribution along the central conductor, the loading of the antenna structure, and the near field radiation patterns over a wide range of frequencies.

The application of the moment method to various problems in this Chapter reveals that a major constraint in the numerical method is the limitation of matrix dimensions. In the NEC program, for example, the number of matrix elements is limited to 300 X 300, which is not sufficient for many applications. One solution to this problem is to increase the matrix size, but this renders an excessive memory requirement and possibly introduces round-off errors. The next Chapter discusses an alternate approach capable of handling large structures with no abrupt changes in radius of curvature.

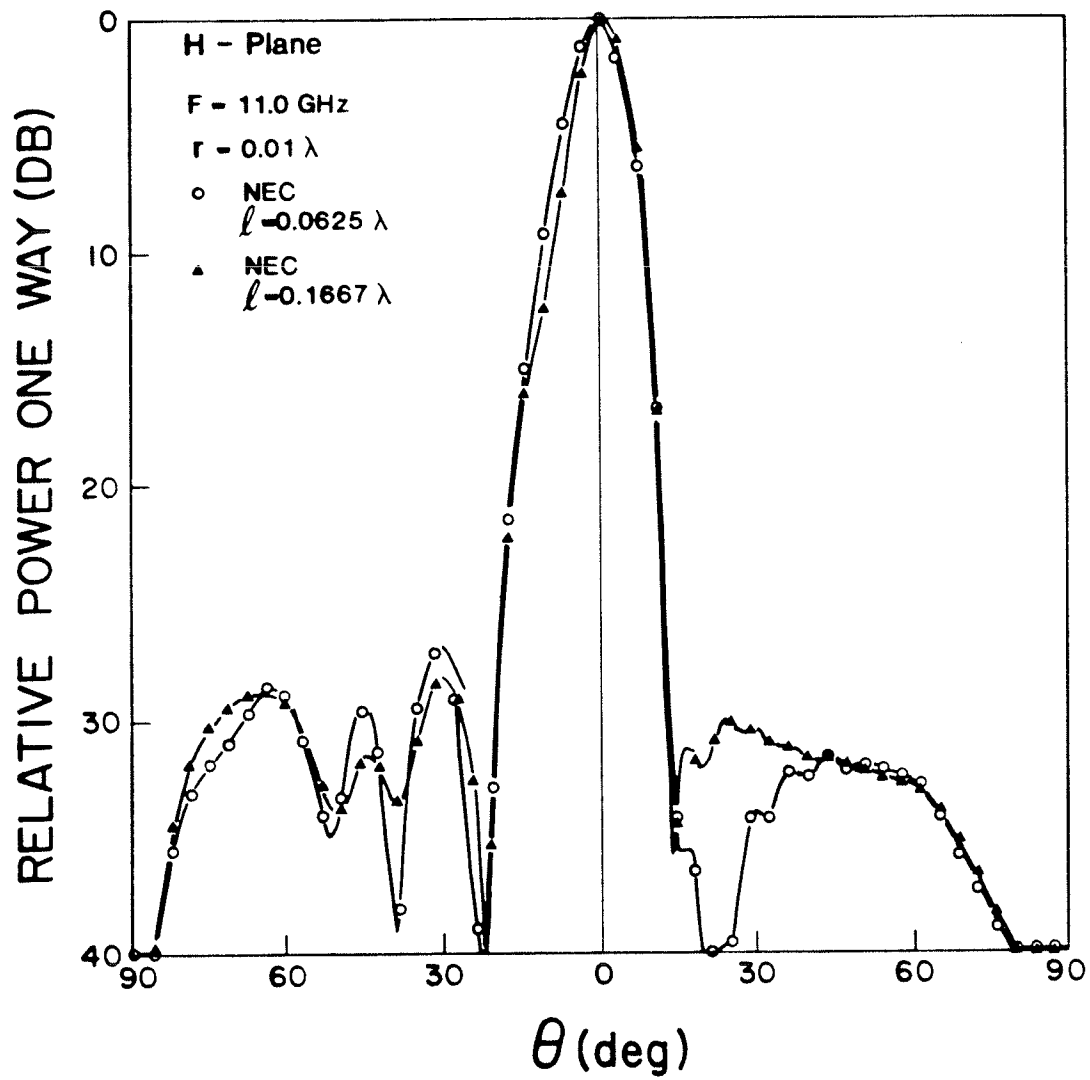


Figure 3.21: Comparison of H-plane Radiation Patterns of Different Segment Lengths

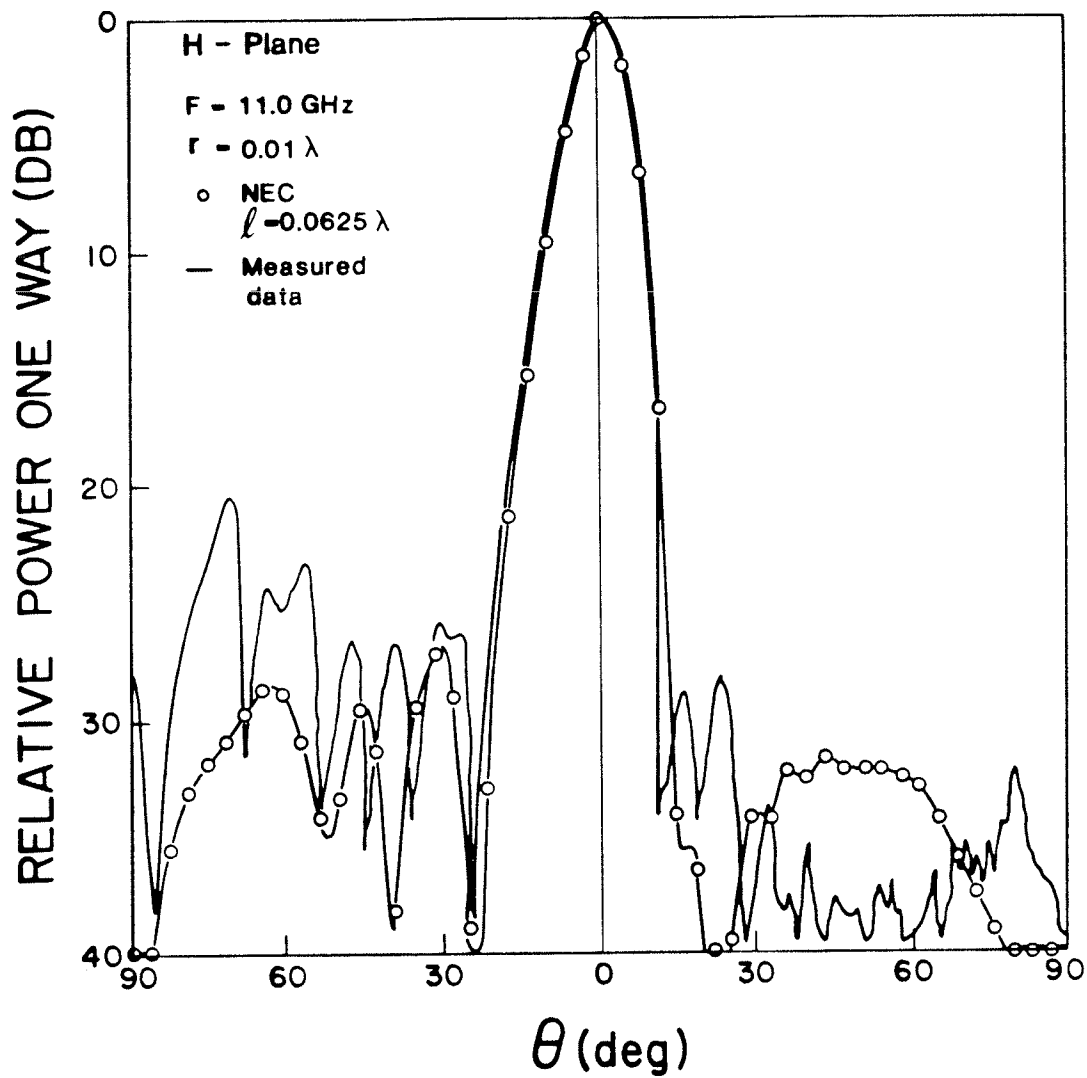


Figure 3.22: Comparison between the Calculated and Measured H-plane Radiation Patterns

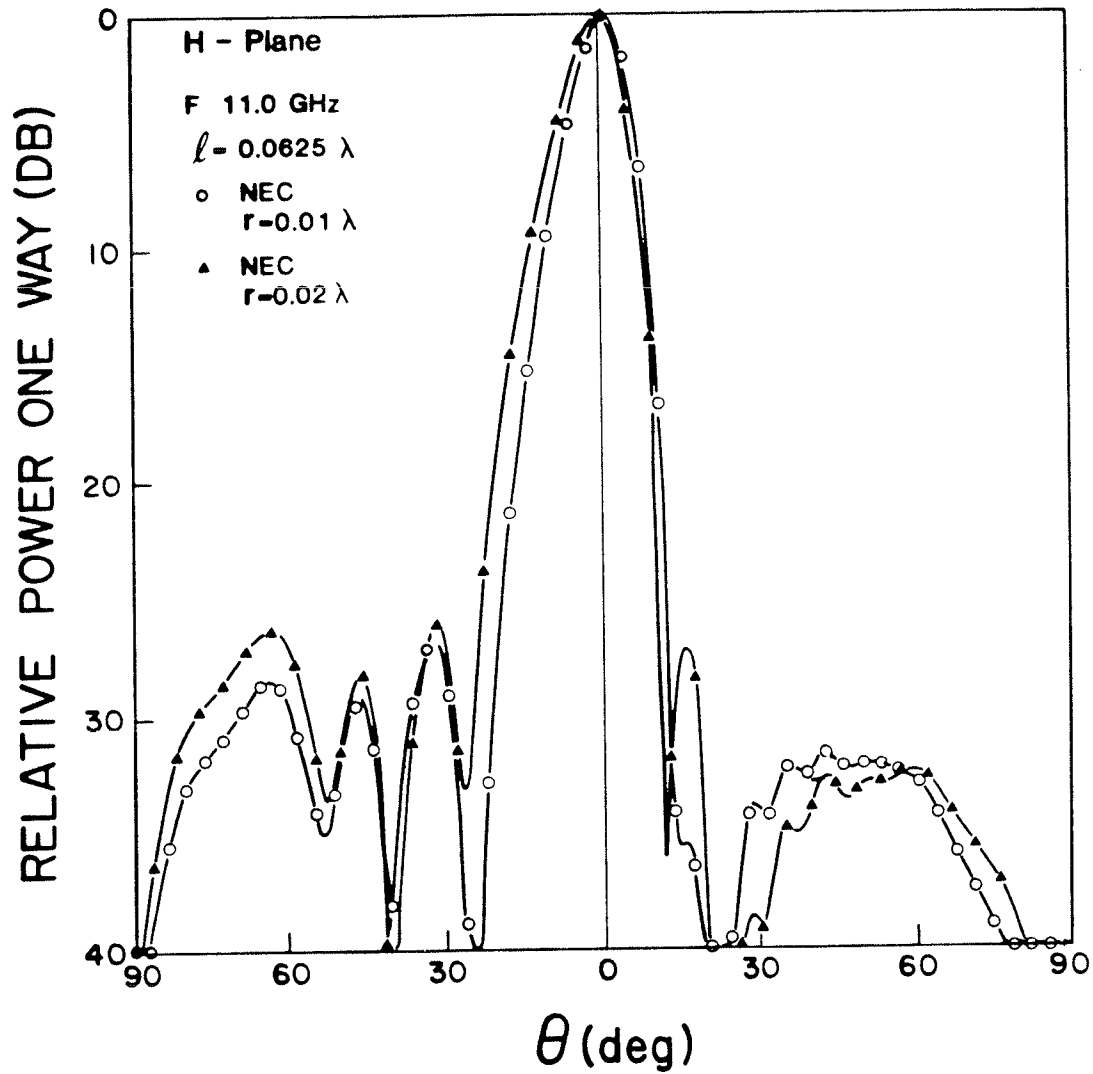


Figure 3.23: Comparison (A) of H-plane Radiation Patterns for Different L/R Ratios

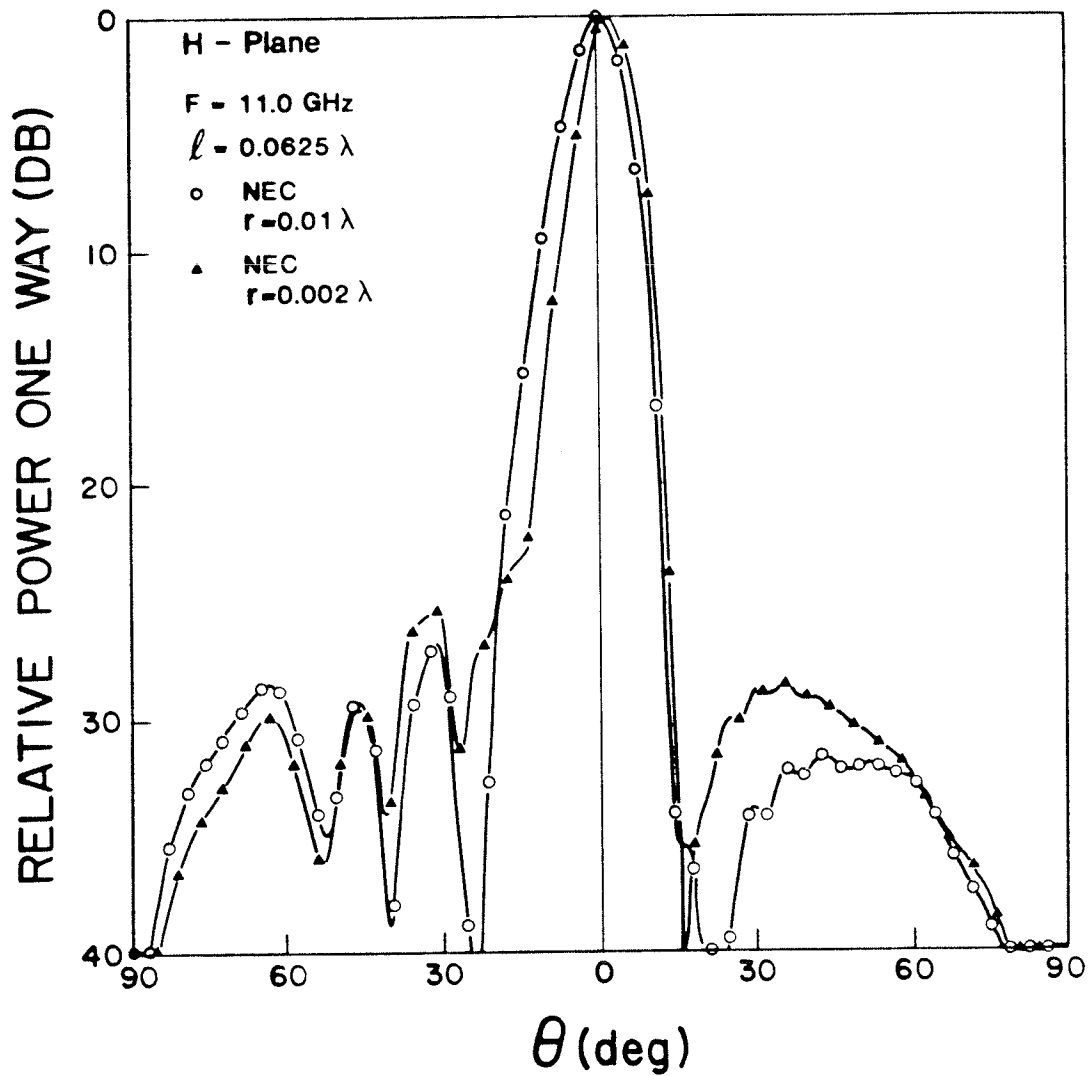


Figure 3.24: Comparison (B) of H-plane Radiation Patterns for Different L/R Ratios

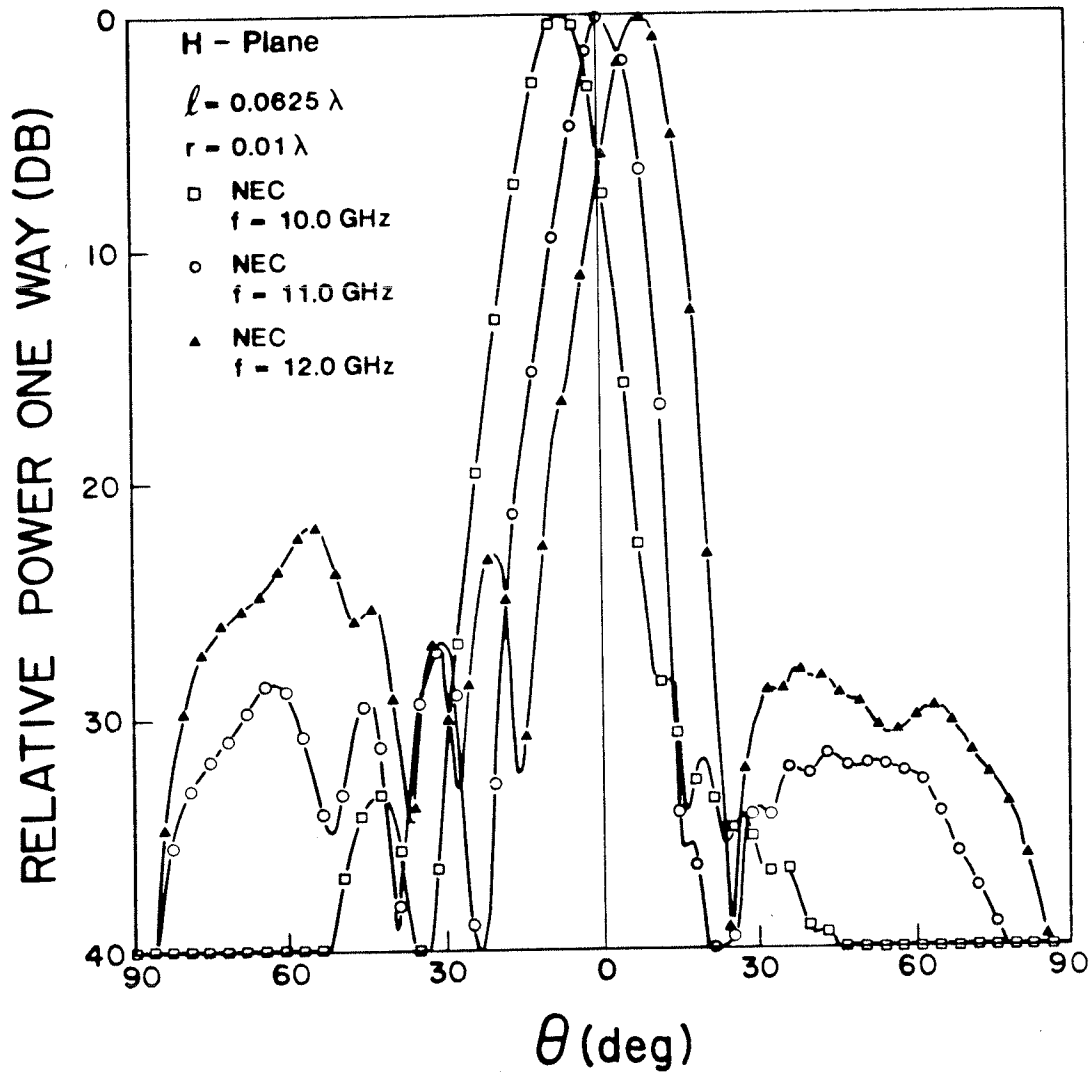


Figure 3.25: Beam Squint with Respect to Different Frequencies

Chapter IV

TECHNIQUES FOR THE SOLUTION OF ELECTRICALLY LARGE STRUCTURES

Because of the nature of the integral formulation, a field component at a given point in space depends on the overall surface current distribution. The moment method is a numerical solution technique for such integral equations. Difficulties arise when the moment method is applied to electromagnetic scattering by very large objects as the matrix size increases drastically with a small increase in electrical dimension. The resulting matrix is either too large or too costly to be handled by many main frame computers. To address this crucial issue, this Chapter describes the advantages of using geometrical symmetry, followed by a discussion of the utilization of virtual memory addressing to improve performance of programs involving large matrices. Finally, the Chapter ends with a detailed discussion of a rapid and reasonably accurate method for solving electrically large objects.

4.1 UTILIZATION OF SYMMETRY

Whenever the geometry of a structure allows, symmetry should be utilized to simplify the solution of the current coefficient matrix. Table 4.1 compares the proportionality factors of matrix storage requirement, matrix fill up time, and matrix factor time for different

numbers of planes of symmetry. Column two represents the in-core memory required to store the complex coefficient matrix for a structure modeled by N elements. Column three shows the optimum computation time required to fill up the coefficient matrix. The generation time of each matrix element depends on the nature of each problem and may increase drastically. The last column indicates the required computation time for factoring a matrix in core memory. This comparison reveals that the utilization of geometrical symmetry not only reduces the memory requirement but also reduces the matrix fill up time and matrix factor time significantly.

TABLE 4.1			
Comparison of Matrix Storage, Fill-up Time, and Factor Time for Different Numbers of Planes of Symmetry			
No. of Planes of Symmetry	Matrix Storage	Matrix Fill Up Time	Matrix Factor Time
0	N^2	N^2	$N^3/3$
1	$N^2/2$	$N^2/2$	$N^3/12$
2	$N^2/4$	$N^2/4$	$N^3/48$
3	$N^2/8$	$N^2/8$	$N^3/192$

4.2 VIRTUAL MEMORY ADDRESSING TECHNIQUE

Before the advent of virtual memory computer systems, numerical application programmers implemented their algorithms based on memory overlays for large programs and out-of-core storage for big matrices. Memory overlays reuse the same memory region over and over again for different segments of a program. This technique requires extra effort to partition a program and keep track of the size and sequence of each program segment. Out-of-core storage keeps the major portion of a matrix in secondary storage devices, such as disks and tapes, and swaps the required portion into the system memory on demand. These compromising schemes use up excessive central processor unit (CPU) time and thus slow down program execution. The techniques are still appropriate for mini or desk-top computers, which support limited physical memory and small address space. However, for main frame or super-mini computers the techniques have become obsolete, as these new generation computers provide virtual memory addressing. This section discusses the advantage of using virtual memory addressing to improve performance of programs involving many large matrices.

For a program like NEC, the execution time depends on the number of patches and wire segments needed to model an object. In general, the required CPU time approximately follows the formula:

$$T = (T_1 + T_2 + T_3 + T_4)\tau \quad (4.1)$$

$$T_1 = 2^{-s}N^2 \quad (4.2)$$

$$T_2 = \frac{4^{-s}N^3}{3} \quad (4.3)$$

$$T_3 = \frac{N^3}{4^s} \left(\frac{N^2}{C} - 1 \right) \quad (4.4)$$

$$T_4 = 2^{-s+1} N^2 \quad (4.5)$$

where

τ = average CPU time required for one operation

s = numbers of planes of symmetry

C = in-core memory available for the program

N = number of patches or wire segments

T_1 is the computer time required to fill the interaction matrix; T_2 is the time needed to factor the matrix; T_3 is the time needed to re-compute element locations and transfer records when out-of-core storage is required; and T_4 is the time required to calculate the current and field solutions. For small objects, T_1 and T_2 account for nearly all the running time, unless a large number of excitations or far fields are requested. But for large structures, if the out-of-core storage concept is used, the required data has to be swapped between the program store and the secondary storage devices. However, re-computing the element locations and transferring records consumes additional CPU time. In such cases, T_3 will become a dominant factor. Since new main frame and super-mini computers have built-in hardware to provide virtual memory addressing, these computers can handle memory management more efficiently. Therefore, for an application program involving many large matrices, the new trend is to store all the matrices in the program store.

Although the original version of the NEC program allows rather large integral problems to be handled with minimal core memory, it suffers from lack of speed. This is primarily due to the necessity of re-computing the element locations and excessive data transfers between the system core memory and disk storage. To improve the efficiency, the NEC program was modified by applying a virtual memory addressing scheme, and the results are summarized in Table 4.2. In the table, the first row represents the requirements of the original NEC program, and the second row the requirements of the modified version. The second column shows the number of records transferred during program execution. Column three indicates the required computation time for calculating the scattering fields from a structure of 108 wire segments. The last column indicates the in-core memory requirements between the original and modified versions of NEC. Data in column two points out that the modified version reduces the number of record transfers by several orders of magnitude. Because of the great reduction in data transfers, the new version of NEC consumes 4.4 times less CPU time for solving the same scattering problem. On the other hand, the new version needs only 40% more program store than the original version. This comparison reveals that the utilization of a virtual memory addressing technique for large matrices has significantly improved the performance of the NEC program.

TABLE 4.2			
Comparison of the Performance of NEC for a Structure of 108 Segments			
Version of NEC	I/O Counts (records)	CPU Time (seconds)	Core Storage (kilo bytes)
Original	62 732	364.913	512
Modified	758	83.743	700

4.3 PROGRESSIVE NUMERICAL METHOD (PNM)

The previous sections demonstrate that the utilization of structure symmetry and in-core memory speeds up the program execution and reduces I/O counts; however, these improvements have limitations. Beyond 300 X 300 elements, computation errors such as accumulated errors and round off errors become noticeable. This inaccuracy has led to the modification of the moment method by combining asymptotic techniques, such as the physical optics approximation [3] and the geometrical theory of diffraction [4,32] to reduce the size of the matrix required for an accurate solution. Wherever possible, a combination of these asymptotic techniques with the moment method is probably the most efficient and promising way of obtaining the numerical solution of field problems where electrically large structures are concerned.

For geometrical reasons the asymptotic techniques may not be applicable for a wide class of field problems, particularly in the

antenna area. As a result an alternate numerical approach, which overcomes the difficulties of large matrix inversions in the conventional moment method, must be developed. Shafai [33] has solved two dimensional problems of scattering by very large objects, using the progressive numerical method (PNM). To reduce matrix dimensions, his method applies the reduction of interactions among the surface current distributions as a function of the electrical distance. That is, instead of solving the integral equation simultaneously for the entire object, the PNM solves the integral equations for selected subregions of the surface progressively. This method is essentially an extension of Kinzel's sectioning method [34] but includes the effect of earlier computed surface current distributions at each subsequent evaluation step. The following sections discuss the PNM, the optimization employed to find the parameters needed to use the method effectively, and applications of the PNM to two dimensional scattering problems.

4.3.1 Description of the Method

Since Shafai [33] has described the principle of the PNM, the following is only a summary of the method. As mentioned in Chapter II solutions of the electric or magnetic field integral equations, using the moment method, can be reduced to matrix equations of the form:

$$[G][I] = [E] \quad (4.6)$$

where $[E]$ is the excitation matrix obtained by sampling the incident field on the surface of the object. The matrix $[I]$ is the unknown

current distribution, and $[G]$ is an $N \times N$ square matrix representing the coefficients obtained from expanding the unknown function. Off-diagonal elements of $[G]$ are due to mutual interactions of the unknown current distribution. Expanding the matrix in its component forms, Equation (4.6) can be written as

$$\begin{bmatrix} [G_{11}] & [G_{12}] & \cdot & \cdot & \cdot & [G_{1n}] \\ [G_{21}] & [G_{22}] & \cdot & \cdot & \cdot & [G_{2n}] \\ \cdot & \cdot & \cdot & \cdot & \cdot & \cdot \\ \cdot & \cdot & \cdot & \cdot & \cdot & \cdot \\ \cdot & \cdot & \cdot & \cdot & \cdot & \cdot \\ [G_{n1}] & [G_{n2}] & \cdot & \cdot & \cdot & [G_{nn}] \end{bmatrix} \begin{bmatrix} [I_1] \\ [I_2] \\ \cdot \\ \cdot \\ \cdot \\ [I_n] \end{bmatrix} = \begin{bmatrix} [E_1] \\ [E_2] \\ \cdot \\ \cdot \\ \cdot \\ [E_n] \end{bmatrix} \quad (4.7)$$

where $[G_{11}]$, $[G_{12}]$, ..., $[G_{nn}]$ are $M \times M$ square matrices with $M \ll N$. Geometrically, this is equivalent to sub-dividing an object into several small sub-regions as illustrated in Figure 4.1.

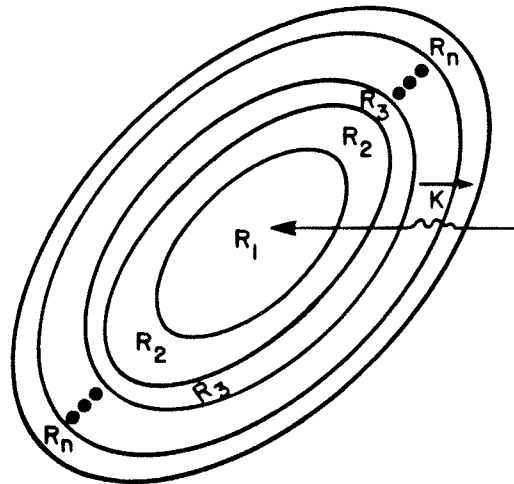


Figure 4.1: Dividing an Object into Several Small Sub-regions

If the first region R_1 is selected in such a way that its current distribution is governed mainly by the excitation, the induced

surface current of this region can be calculated while neglecting the interactions from the remaining sections of the object. For conducting scatterers, this region is located at the centre of illumination of the applied incident field. Using this approach, field relations in R_1 can be simplified to

$$[G_{11}][I_1] = [E_1], \quad (4.8)$$

and the solution of which gives approximately the required current distribution $[I_1]$. Similarly, assuming the current distribution in the second region R_2 can be determined mainly by the contribution of R_1 and the excitation, the unknown field function can be expressed as

$$[G_{22}][I_2] = [E_2] - [G_{21}][I_1] \quad (4.9)$$

The solution of this equation then gives the required current $[I_2]$.

Solutions of regions one and two can subsequently be used to find the current distribution for region three. This process can be applied successively until the required current distribution for the last region is found. In general, for the n^{th} region, the field relation is

$$[G_{nn}][I_n] = [E_n] - \sum_{i=1}^{n-1} [G_{ni}][I_i]. \quad (4.10)$$

However, because of the coupling effect from the adjoining region, solutions calculated near the edge of each region become inaccurate. An iteration process may be one way of enhancing the accuracy but is usually slow and expensive. Alternatively, overlapping regions may be used to improve the accuracy of the

solution. That is, in each evaluation step, instead of retaining all the previously calculated solutions, inaccurate solutions close to the adjoining region to be calculated next are discarded. The next region then begins immediately after the last retained solution. The geometry of such overlapping regions and their matrix representation are shown in Figures 4.2 and 4.3, respectively.

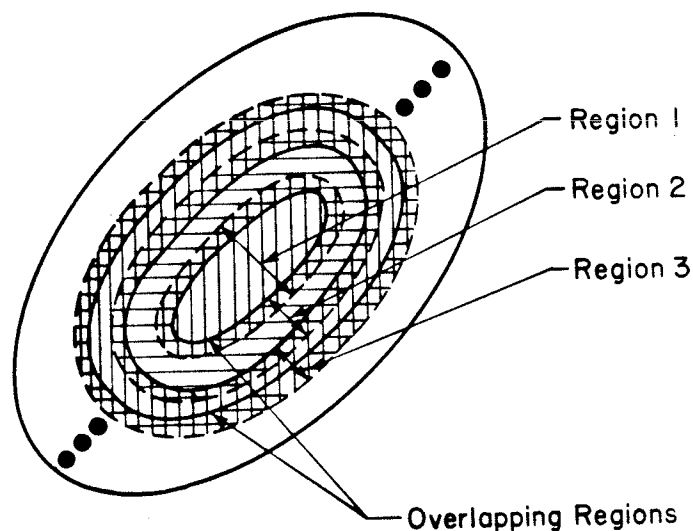


Figure 4.2: Geometry of Overlapping Regions

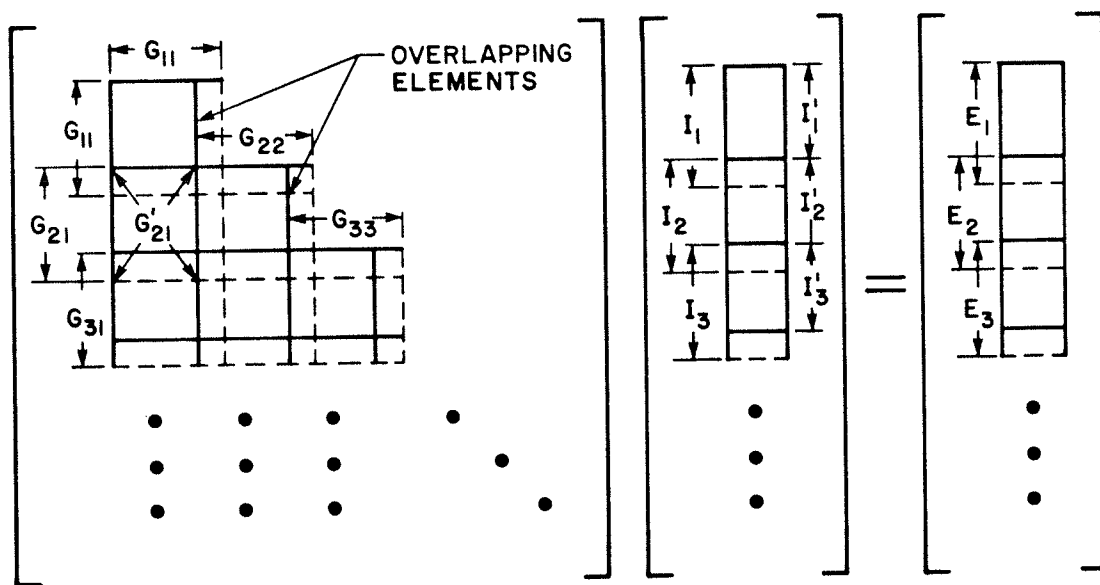


Figure 4.3: Matrix Representation of Overlapping Regions

In order to use the PNM effectively, it is necessary to understand the effect of the region size and degree of overlapping between adjoining regions on the accuracy of the solution. The last section of this Chapter discusses an optimization process for finding the optimal values for these parameters. After determining the optimal region size and the number of calculated solutions to be retained, Equation (4.8) can be used to find $[I_1]$. Retaining $[I_1']$, the acceptable part of $[I_1]$, $[I_2]$ can now be calculated from

$$[G_{22}][I_2] = [E_2] - [G'_{21}][I_1'] \quad (4.11)$$

where $[G'_{21}]$ is non-square matrix as shown in Figure 4.3. Similarly, for the n^{th} region, Equation (4.10) becomes

$$[G_{nn}][I_n] = [E_n] - \sum_{i=1}^{n-1} [G'_{ni}][I_i'], \quad (4.12)$$

and is used in the implementation of the PNM program as listed in Appendix A.

4.3.2 Discussion of the Method

Equations (4.8) and (4.12) together with Figure 4.3 indicate that when solving field equations, the PNM utilizes mostly the lower triangular elements of the coefficient matrix. For the upper triangular matrix, the method requires only the upper elements of the diagonal sub-matrices $[G_{11}]$, $[G_{22}]$, ..., $[G_{nn}]$. Let M denote the dimension of these sub-matrices and N the dimension of the coefficient matrix. For M much smaller than N , the PNM becomes equivalent to a

partial triangularization of the coefficient matrix. In other words, by solving these sub-regions progressively, the PNM directly obtains a matrix which is nearly lower triangular. However, for the conventional moment method, only after numerous calculations, such as the LU-factorization or the Gauss elimination, does the coefficient matrix become a triangular one. The only price the PNM pays for this saving is the generation and manipulation of excitation terms. This section analyzes the computation time requirements for the PNM and compares them with those of the conventional moment method.

If the Gauss elimination is used to solve matrix equations for both the conventional moment method and the PNM, their computational time requirements can be compared. The moment method expands the unknown function into an $N \times N$ coefficient matrix; thus, the computer time required to fill up such a matrix is

$$t = N^2 \alpha \quad (4.13)$$

where α denotes the computer CPU time unit for generating a matrix element. On the other hand, the matrix fill up time for the PNM can be expressed as

$$t' = \left(\frac{1}{2} N^2 + MN - \frac{1}{2} M^2 \right) \alpha \approx \frac{1}{2} N^2 \alpha \quad (4.14)$$

or

$$\frac{t'}{t} \approx \frac{1}{2} . \quad (4.15)$$

Unfortunately, the generation time α of each matrix element depends on the nature of each problem and cannot be generalized. As a

result, it is not included in the comparison. Nevertheless, it is worth mentioning that some problems may require costly computation of special functions, such as Bessel or Legendre functions or even numerical integrations.

The Gauss elimination technique involves approximately $N^3/3$ operations. Thus, the computer time required for the solution of the matrix equation of the moment method is given by

$$T = \frac{1}{3} N^3 u \quad (4.16)$$

where u is the CPU time per operation. However, Equations (4.8) and (4.12) indicate that the solution process of the PNM involves two separate computations. That is, for each evaluation step, the PNM must i) generate the excitation terms and ii) calculate the solution of an $M \times M$ matrix. If overlappings are utilized to reduce coupling effects between adjoining regions, and m out of M solutions are retained for each evaluation step, then $n = N/m$ becomes the total number of steps needed. The time factors for the solution of the matrix equation of the PNM can now be expressed as

$$T_1 = \frac{1}{2} n^2 M m u \quad (4.17)$$

$$T_2 = \frac{1}{3} n M^3 u \quad (4.18)$$

where T_1 and T_2 refer to computation times for the generation of the excitation terms and the matrix solutions, respectively. Thus the total computer time for the PNM is given by

$$T' = \frac{1}{2} n^2 M m u \left(1 + \frac{2}{3} \frac{M^2}{N} \right) \quad (4.19)$$

or

$$\frac{T'}{T} = \frac{3}{2} \frac{M}{m} \left[\frac{1}{N} + \frac{2}{3} \left(\frac{M}{N} \right)^2 \right] \quad (4.20)$$

which shows considerable saving in computation time for $M \ll N$. Also, the comparison points out that the computation time depends on the degree of overlapping between adjoining regions. Hence, the optimal values for M and m play an important role in reducing the computation time requirement for the PNM. With the aim of improving the solution accuracy of the PNM, the following section discusses an optimization process which yields the optimal combination for parameters M and m .

4.3.3 Optimal Parameters for the PNM

Any attempt at optimization of the PNM must concentrate on minimizing the errors of the solution, with a reduction in computer CPU time and required memory. The present investigation attempts to find the optimal values for the number of divisions (X_1) per wavelength, the sub-region size (X_2) for each evaluation step, and the number of calculated current pulses (X_3) which are discarded to reduce coupling effects between regions. This section discusses the formulation of the object function, the structure of the staged-analysis program, and the ease with which various objectives may be incorporated. Finally, the section ends with a discussion of the physical significance of the optimal parameters found.

The fundamental problem of optimization is to arrive at the best possible decision in any given set of circumstances. Two different

approaches are available for the optimization process, namely the indirect method and direct search method [35]. The use of indirect methods require that a function is differentiable; hence, the method is restricted to well-behaved functions [36]. Even when functions are piecewise continuous and differentiable, the application of indirect methods to multi-dimensional problems involves tedious and burdensome manipulations. On the other hand, the direct search method involves only function evaluations and comparisons and is relatively easier to apply for problems of multi-variables. The discrete nature of parameters X_1 , X_2 , and X_3 suggests that the direct search approach is the only feasible choice.

To analyze the behaviour of the optimal values for these parameters, the optimization process should compare the solution of the PNM with that of the conventional moment method and minimize their difference by varying the parameters. However, for electrically large objects, this procedure introduces two drawbacks: i) the solution of the moment method may not be accurate and ii) excessive computer CPU time is required to invert the large $N \times N$ matrix produced by the moment method. In order to alleviate effects of these drawbacks, the optimization process is applied to a problem of which an analytical solution exists, so that the objective function minimizes the difference between the exact and PNM solutions.

For conducting circular cylinders, the difference between the exact field solution and the numerical solution obtained by the PNM can be formulated as a non-linear optimization problem. Practically,

X_1 can be increased, over a wide range, to improve accuracy. However, as X_1 increases so does the number of calculations, and as a result excessive computation time becomes a major difficulty. For this reason, X_1 has been limited to $8 \leq X_1 \leq 15$. In stage one of the optimization process, the function to be minimized is:

$$F_1(\underline{x}) = \sum_{n=1}^N W_n (|I_n^{\text{exact}}(\underline{x}) - I_n^{\text{PNM}}(\underline{x})|) \quad (4.21)$$

where

$$W_n = I_n^{\text{PNM}}(\underline{x}) \quad (4.22)$$

$I_n^{\text{Exact}}(\underline{x})$ = exact solution for the n^{th} current element

$I_n^{\text{PNM}}(\underline{x})$ = PNM solution for the n^{th} current element

subject to

$$8 \leq X_1 \leq 15 \quad (4.23)$$

$$X_2 = X_1 \quad (4.24)$$

$$X_3 = 0. \quad (4.25)$$

The use of the current element itself as a weighting function emphasizes the effect of errors in large currents.

To make the optimization process more effective, stage one minimizes the errors in the current elements instead of in the field components. Since the surface currents at different parts of an object are found through different equations, the summation of the

random errors in the induced current does not generally cancel out. However, when the current elements are added together to yield the field components, the vector sum tends to cancel out the random errors. This cancellation suggests that the relative errors in the current elements are, in general, much larger than those in the field components. Therefore, in stage one it is more effective to minimize the total current element error rather than the total field solution error.

After stage one, the optimization problem reduces to a two dimensional one. In stage two, the function to be minimized becomes:

$$F_2(\tilde{x}) = \sum_{n=1}^N W_n (|F_n^{\text{exact}}(\tilde{x}) - F_n^{\text{PNM}}(\tilde{x})|) + W_{N+1} \text{MEMORY}(\tilde{x}) + W_{N+2} \text{TIME}(\tilde{x}) \quad (4.26)$$

where

$$W_n = F_n^{\text{PNM}}(\tilde{x}) \quad (4.27)$$

$F_n^{\text{exact}}(\tilde{x})$ = exact field solution for the n^{th} element

$F_n^{\text{PNM}}(\tilde{x})$ = PNM field solution for the n^{th} element

$$W_{N+1} = \begin{cases} 20 & \text{when MEMORY}(\tilde{x}) - \text{MEMORY}_S > 0 \\ 0 & \text{when MEMORY}(\tilde{x}) - \text{MEMORY}_S \leq 0 \end{cases} \quad (4.28)$$

$$W_{N+2} = \begin{cases} 20 & \text{when TIME}(\tilde{x}) - \text{TIME}_S > 0 \\ 0 & \text{when TIME}(\tilde{x}) - \text{TIME}_S \leq 0 \end{cases} \quad (4.29)$$

subject to

$$x_2 \leq x_1 \quad (4.30)$$

$$x_3 < x_2 \quad (4.31)$$

$$X_i > 0, \quad i = 2,3. \quad (4.32)$$

Similar to stage one, the field component itself is used as a weighting function. $MEMORY_S$ and $TIME_S$ are the maximum memory size and computer CPU time allowed before a penalty factor is applied. These constraints are imposed by the user to fit particular requirements. For this analysis, they are set to the lowest values arrived at the end of stage one.

The two objective functions (4.21) and (4.26) and their associated constraint functions are evaluated using a multi-stage optimization program. The program, listed in Appendix C, applies a combination of dynamic programming [35, 36, 37] and integer programming [38, 39] to perform optimization. Figure B.1 of Appendix B illustrates the block diagram of this process.

In stage one, the optimization process keeps the values for X_2 and X_3 fixed and applies an equal interval search [38] to the objective function (4.21) to determine the optimal value for X_1 . In stage two, the process uses a grid search method [39], based on the objective function (4.26), to obtain optimal values for X_2 and X_3 while the value of X_1 , obtained in stage one, remains fixed. Finally, in stage three the optimization program varies the results obtained from stages one and two and employs a similar grid search to yield the best combination of parameters. Figures B.2 to B.4 of Appendix B illustrate the detailed algorithm for stages one to three, respectively.

During the optimization process, if the total number of divisions required to cover the entire object is not an integral multiple of the number of current pulses retained in each step, a special technique is employed to calculate the last region. This special feature allows the staged-analysis program to analyze any combination of discrete parameters.

In order to examine the effectiveness of the objective functions (4.21) and (4.26), the optimization process was applied to scattering from conducting circular cylinders. For simplicity only two-dimensional scattering problems were considered by assuming that the cylinder is infinitely long. The incident field was taken as a plane wave, at normal incidence, travelling in the negative x-direction as shown in Figure 4.4. Because of geometrical symmetry, the incident field was sampled only at half the points in the positive y-direction. However, the induced currents were sampled uniformly using the pulse function technique [8, pp. 11-12]. The respective transverse magnetic (TM) and transverse electric (TE) field integral equations and their matrix formulations [8, pp. 41-57] are well known and are given by

$$E_z^i(\bar{r}) = \frac{k\eta}{4} \int_C J_z(\bar{r}') H_0^{(2)}(k|\bar{r}-\bar{r}'|) dc' \quad r \text{ on } C \quad (4.33)$$

$$H_z^i(\bar{r}) = -\frac{1}{2} J_z(\bar{r}) + \frac{j}{4} \int_C J_z(\bar{r}') H_1^{(2)}(k|\bar{r}-\bar{r}'|) \times \cos(\hat{n}, \bar{r}-\bar{r}') dc', \quad r \text{ on } C \quad (4.34)$$

where η is the free space wave impedance and $H_0^{(2)}$ and $H_1^{(2)}$ are Hankel functions of zero and first order, respectively. Both equations have

been applied to analyze the performance of the optimization process. As the TE case involves more complex field equations, its results were used to draw conclusions on the optimal parameters.

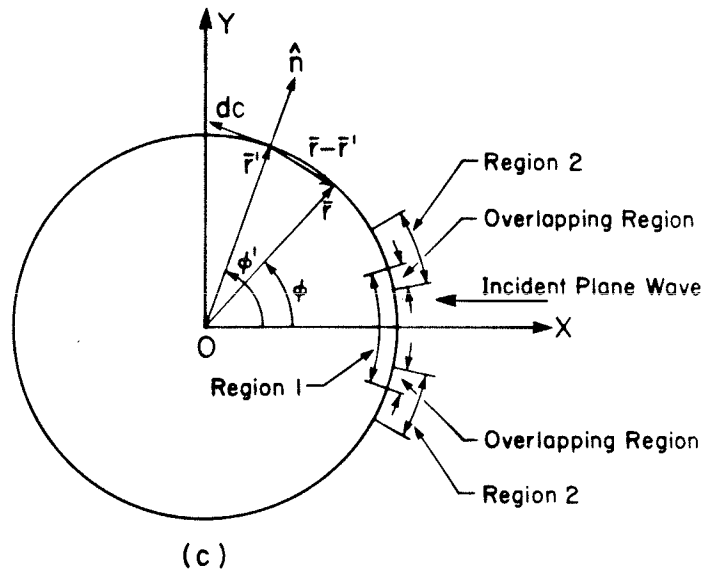


Figure 4.4: Cross Section of a Circular Cylinder and Coordinate System

Initially, the optimization process was applied to a circular cylinder of $ka = 10$, the results of which are listed in Table 4.3. In the table X_1 is the number of divisions per wavelength, X_2 the region size for each calculation step, and X_3 the number of discarded current pulses in each step. $F_2(\underline{X})$ is the total computation error for the field solution based on the objective function (4.26). TIME and MEMORY are the computation time and memory required by the PNM using these parameters. Note that the CPU time is for Amdahl 5850. The data in column four indicates that the optimization process reduces the total computation error from 10.45 to 4.25. To generalize the relationships between these parameters over a wide range of

frequencies, the optimization process was analyzed for test runs having ka values ranging from 8.0 to 18.0. Table 4.4 shows the results of this analysis.

TABLE 4.3					
Optimal Results of Stage 3 for ka = 10					
X_1	X_2	X_3	$F_2(x)$	TIME (seconds)	MEMORY (k bytes)
7	6	1	9.49	0.36	0.281
8	4	1	6.68	0.45	0.125
9	4	2	9.37	0.68	0.125
10	5	1	10.45	0.62	0.195
11	6	2	4.25	0.81	0.281

The results of using different ka values show that X_1 has a mean value of 10.6 and a standard deviation of 2.2; X_2 has a mean value of 5.3 and a standard deviation of 1.1; and X_3 has a mean value of 2.0 and a standard deviation of 0.4. When these mean values are truncated to integers, these parameters have the following relationship:

$$X_1 = S \quad (4.35)$$

$$X_2 = S/2 \quad (4.36)$$

$$X_3 = S/5 \quad (4.37)$$

$$R = ka * X_1 \quad (4.38)$$

where S ranges from 8 to 12, and R is the total number of elements along the contour of a conducting object. The mean value of X_1 also indicates that an appropriate choice of S is 10. Equations (4.35) to (4.38) reveal that only R depends on the electrical dimension. The reason is that if the frequency of the excitation field is fixed and the electrical dimensions of the object are increased, more sampling points on the object's surface are required to maintain the same accuracy.

TABLE 4.4
Optimal Results of Stage 3 for different ka values

ka	X_1	X_2	X_3	$F_2(x)$ \sim	TIME (seconds)	MEMORY (k bytes)
8	15	7	3	5.04	1.05	0.383
9	14	7	2	9.83	0.98	0.383
10	11	6	2	4.25	0.62	0.281
11	8	4	1	8.94	0.52	0.125
12	12	6	2	9.29	1.25	0.281
13	10	5	2	12.74	1.10	0.195
14	9	4	2	12.87	1.18	0.125
15	10	5	2	9.15	1.42	0.195
16	8	4	2	15.26	1.21	0.125
17	10	5	2	12.10	1.74	0.195
18	10	5	2	9.13	1.93	0.195

Assuming S equals 10, when $ka = 20$ the values of X_1 , X_2 , X_3 , and R become 10, 5, 2, and 200, respectively. Substituting these values into Equation (4.20), the ratio of the required computation time between the PNM and the moment method is 0.0135. In other words, when $ka = 20$ the PNM is about 73.8 times more efficient than the conventional moment method. Using these parameters the PNM has been applied to scattering from a conducting circular cylinder of $ka = 20$. For comparison, the same scattering problem has also been calculated by the conventional moment method. Numerical data from both methods are compared with the exact analytical solution, and the results are shown in Table 4.5 and Figures 4.5 to 4.8.

TABLE 4.5

Comparison of the Computational Errors, Time, and Storage Requirements of the Moment Method and the PNM

$Ka = 20.0$
Number of Segments per Wavelength = 10

No. of Segments on Each Region	Number of Discarded Currents	Percentage Avg Error-Currents	Percentage Avg Error-Far Fields	Total CPU Seconds Consumed	No. of Bytes Needed
(Moment) 200	0	13.70	10.45	57.32	312.5k
(PNM) 5	2	7.98	4.49	7.86	0.2k

In Table 4.5, the first row represents the results produced by the moment method, and the second row, the results by the PNM. Column one indicates the total region size in terms of the number of segments. The second column indicates the number of discarded currents per region of calculation, after each computation step. Columns three and four represent the computed percentage error of the currents and the scattered field, respectively. These percentage errors were obtained by comparing the solutions of the PNM and moment method to the exact analytical solution. The last two columns show the required computation time and memory for each case. A comparison of the percentage average errors resulting from the use of these two methods indicates that the PNM gives more accurate current and field results than the moment method. Although the required computation time is not exactly 73.8 times faster, the comparison reveals that in practice the PNM is significantly faster than the moment method for electrically large objects. Furthermore, the memory requirement of the PNM is several orders of magnitude less than that of the moment method provided $M \ll N$.

Figures 4.5 and 4.6 compare the computed induced currents produced by the moment method and the PNM with the exact solution. Both numerical results oscillate about the exact solution, but the results using the PNM method are more accurate. Figures 4.7 and 4.8 compare the numerical data for the far scattered fields with the exact solution. Again, the PNM results are more accurate than that of the moment method.

In practice, large problems such as those involving three-dimensional objects can be solved only by resorting to intricate programming strategies. The algorithm presented here, however, requires minimal programming effort and maintains the advantages of rapid execution and reduced memory requirements.

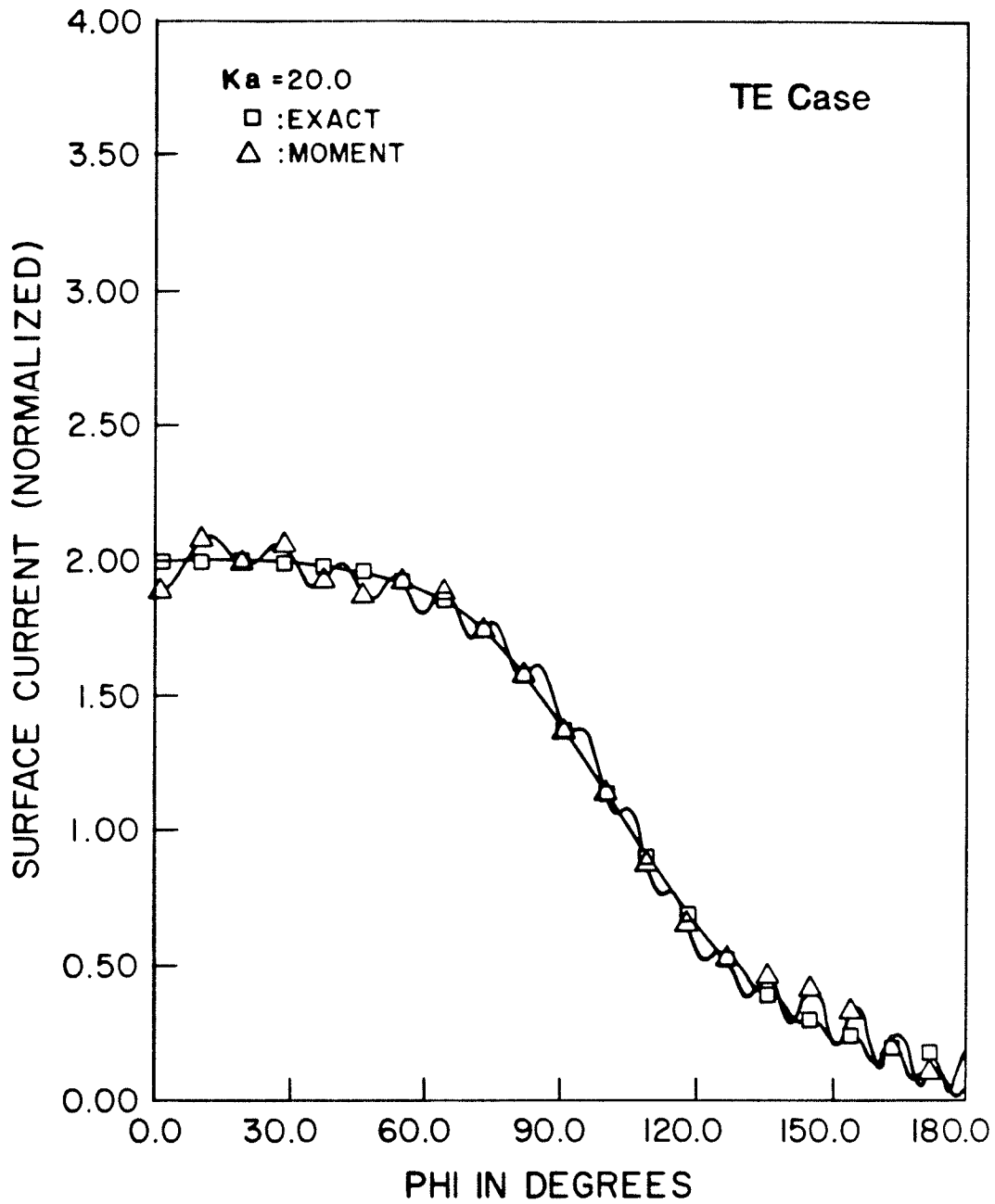


Figure 4.5: Comparison of the Moment Method Surface Current with the Exact Solution

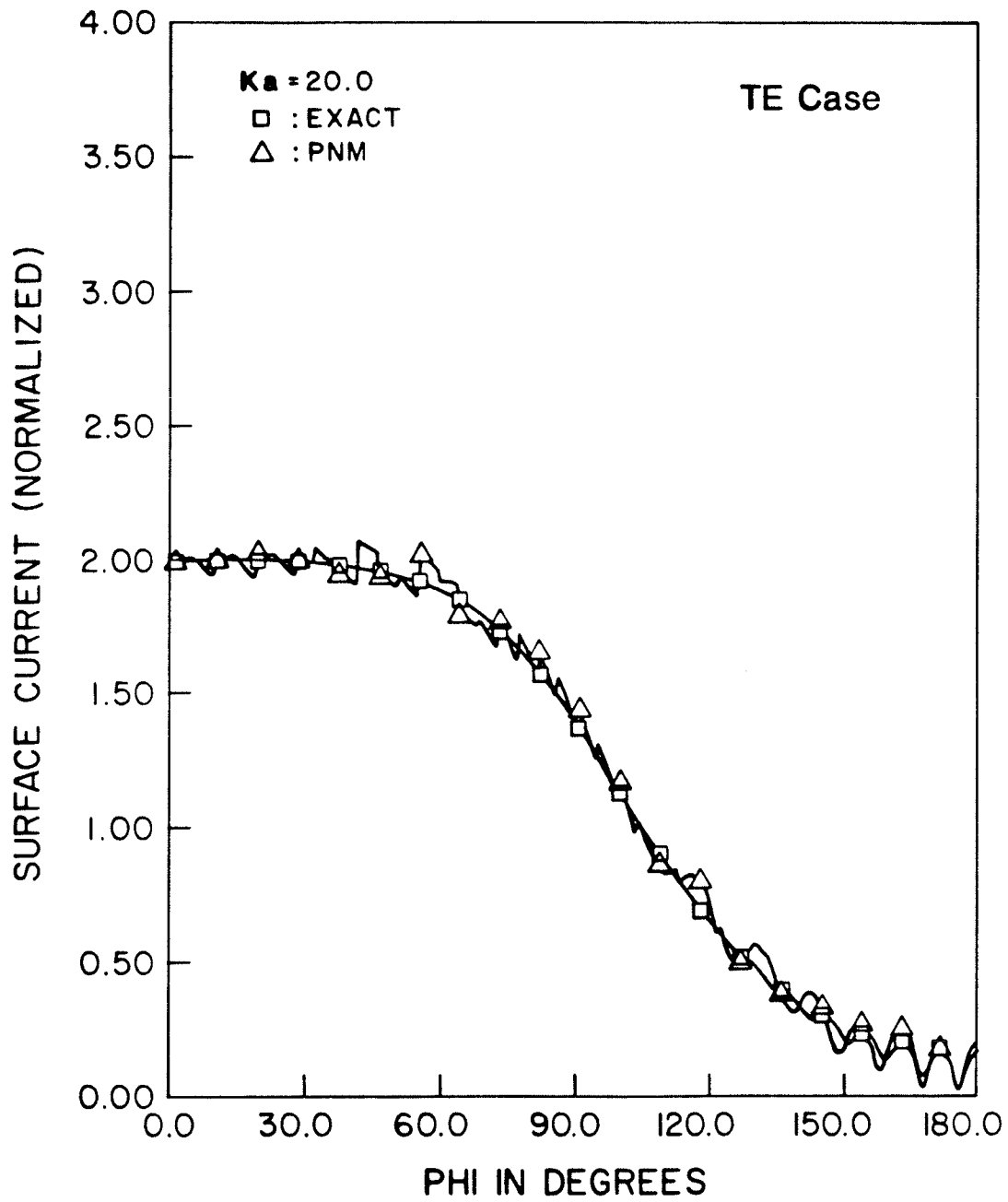


Figure 4.6: Comparison of the PNM Surface Current with the Exact Solution

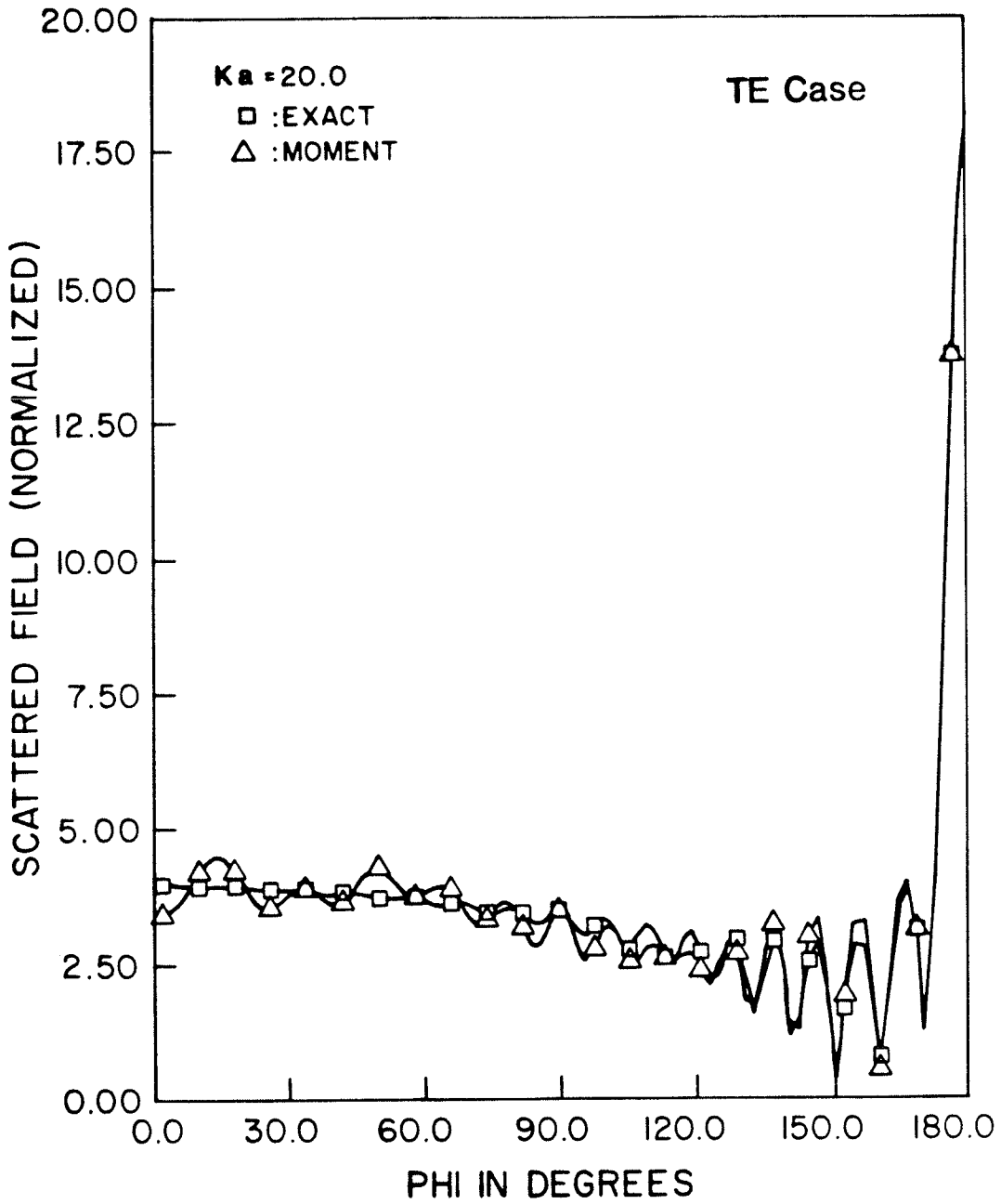


Figure 4.7: Comparison of the Moment Method Far Scattered Field with The Exact Solution

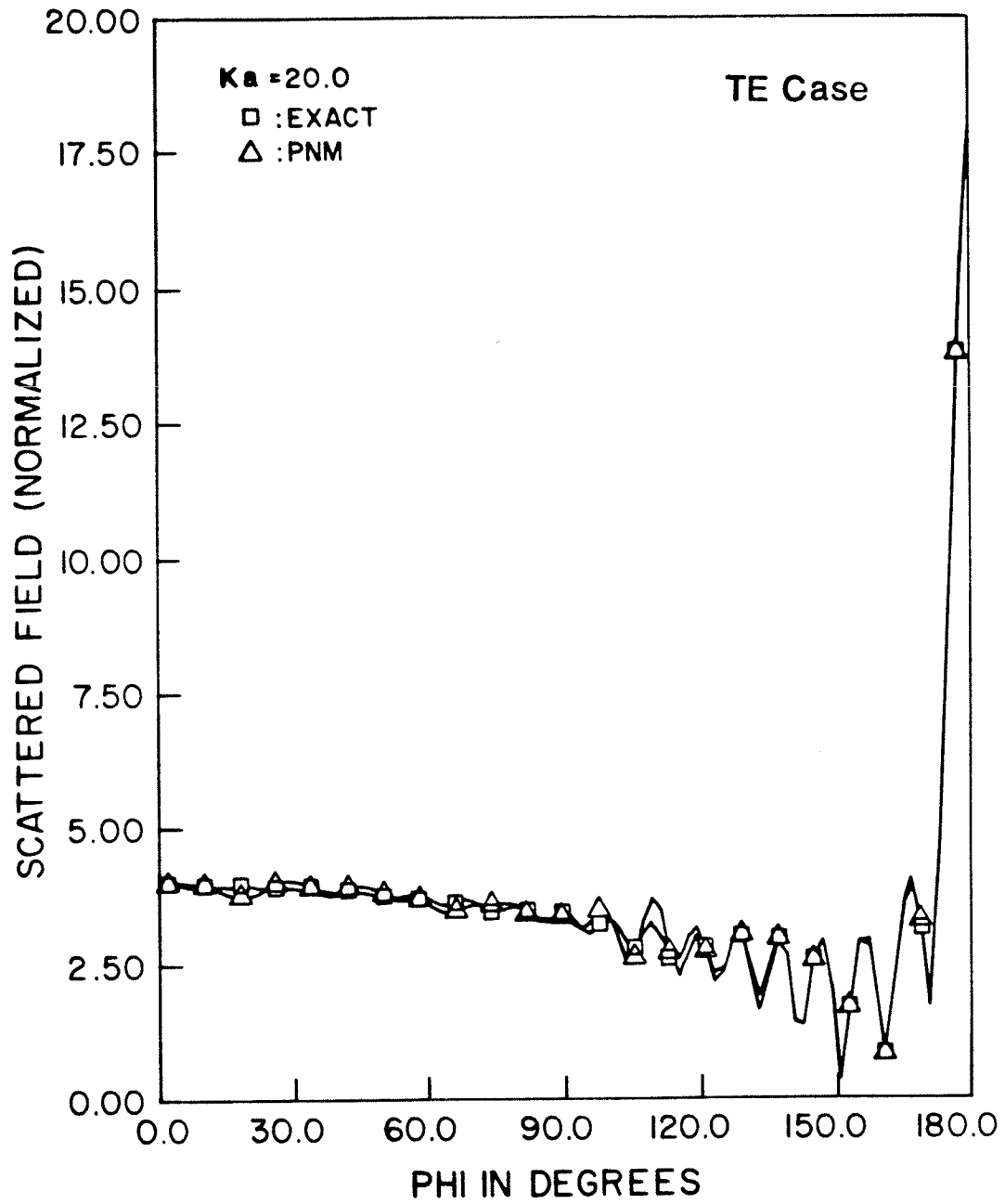


Figure 4.8: Comparison of the PNM Far Scattered Field with The Exact Solution

Chapter V

CONCLUSION

In this thesis general scattering and antenna problems were formulated in terms of the electric and magnetic field integral equations. In the limiting cases the EFIE was specialized for calculating axial currents; thus it is the appropriate choice for modeling wire segments. On the other hand, the MFIE was shown to be specialized for evaluating surface current distributions; hence it was chosen to model surfaces. The moment method was shown to be a feasible mechanism to reduce these integral equations to a set of linear equations whose matrix solution gives the required field distribution.

The application of wire segments and surface patches to model a specific problem geometry imposes a major burden on the user. A common question one may ask is what would be the proper technique to model a structure effectively? The modeling methodology described in this thesis reveals that a thorough understanding of different modeling schemes allows the user to model objects more efficiently. Some practical guidelines for wire segment and surface patch modeling were developed. With the aid of these modeling guidelines, the moment method can be applied to antenna and scattering problems for varying parameters to analyze the constraints of the method. Based on the results of the analysis, the performance and limitations of the method

were determined. The results of modeling a sphere for the determination of its scattering cross-section revealed that surface patch modeling is more suitable for volumetric objects. However, the application of wire modeling to the sandwich wire antenna indicated that this technique is an appropriate choice for wire-type structures. It was shown that by using the proper modeling scheme, reasonably accurate radiation characteristics can be obtained for electrically large and complex structures.

Furthermore, the analysis points out that the principal limitations of the moment method occurs when it is applied to electrically large objects. A study was conducted to find solutions to alleviate these major constraints. New computation techniques which rely on virtual memory addressing were described. For applications involving electrically large objects, these computation techniques lead to a significant improvement in performance.

However, such techniques are not without their limitations. The round off error introduces oscillations in the field solution when the size of the system matrix grows beyond 300 X 300 elements. An increase in the program precision will ease the problem, but renders an increase in the computation time and memory. Alternatively, the progressive numerical method was shown to be a promising scheme for electrically large and smooth objects. In order to use the PNM effectively, it is necessary to understand the effect of the region size and degree of overlapping between adjoining regions on the accuracy of the solution. An optimization process was developed to

investigate these parameters, and the optimal combination of region size and overlap was found. The results obtained with these parameters demonstrates a significant improvement over the conventional moment method.

Nevertheless, further investigation is required to study the effectiveness of the PNM for solving three-dimensional objects and objects composed of dielectric materials. It is expected that the PNM will give improved results for three-dimensional problems as the field magnitude attenuates faster and mutual interactions are weaker. Another area of relevant future research has to do with extending the applicability of the PNM to geometries of general shapes. At present the PNM cannot be applied to a geometry with an abrupt change in the radius of curvature on its surface. By adding more intelligence to the algorithm, the PNM will be capable of solving problems involving arbitrary shapes. In other words, it should be possible to set up the PNM in such a way that the conventional moment method is used to solve regions with abrupt changes and the PNM for the remaining sections.

In summary, the moment method can be applied to electrically large objects to find field responses for both antenna and scattering problems. However, the application of the proper modeling scheme is the key factor which determines whether the results are reliable or not.

Appendix A

THE PNM PROGRAM

```

*****
C
C SUBROUTINE: PNM (PROGRESSIVE NUMERICAL METHOD)
C THIS ROUTINE APPLIES PNM TO OBTAIN THE NUMERIAL SOLUTION OF
C ELECTROMAGNETIC SCATTERING PROBLEMS (TE CASE), USING MOMENT
C METHODS. THE PROGRAM REDUCES THE LARGE MATRIX OF THE
C CONVENTIONAL MOMENT METHOD INTO SEVERAL SMALL MATRICES AND
C DECREASES THE TIME REQUIRED TO SOLVE THE PROBLEM. THE PROGRAM
C WAS WRITTEN IN SUCH A WAY THAT IT CAN ALSO SOLVE THE SCATTERING
C FIELD PROBLEMS BY THE CONVENTIONAL MOTHOD, THAT IS SOLVING THE
C COMPLETE DENSED MATRIX. THE ROUTINE INPUTS KA, PH11, PH12
C AND RETURNS FPNM, JPNM, MEZ, MJZ TO THE INVOKING ROUTINE.
C
C KA = K*A WHERE K: WAVE PROPAGATION CONSTANT AND
C A: RADIUS OF THE CYLINDER
C
C PH11 = THE WHOLE REGION SIZE WHICH IS THE TOTAL NUMBER OF
C DIVISIONS ALONG THE CIRCUMFERENCE OF A CYLINDER SURFACE.
C
C PH12 = A SUBSET OF PH11. THE SIZE OF PH12 MUST BE
C (PH12 .GE. 1) .AND. (PH12 .LE. PH11).
C
C PH13 = THE AMOUNT OF PH12 WHICH IS DISCARDED DURING THE PNM
C CALCULATION. THE SIZE OF PH13 IS (PH13 .GE. 0.) .AND.
C (PH13 .LE. PH12).
C
C FPNM(37) = H-FIELD GENERATED BY PNM METHOD. THE FIELD ARE
C EVALUATED FROM 0 TO 180 (PHI) WITH 5 DEGREE
C INCREMENTAL STEPS.
C
C JPNM(PH11) = CALCULATED CURRENT ELEMENTS ALONG THE
C CIRCUMERENCE OF THE CONDUCTOR FOR THE H-FIELD.
C
C MEZ(37) = E-FIELD GENERATED BY THE PNM. THE FIELD ARE
C EVALUATED FROM 0 TO 180 (PHI) WITH 5 DEGREE
C INCREMENTAL STEPS.
C
C MJZ(PH11) = CALCULATED CURRENT ELEMENTS ALONG THE
C CIRCUMERENCE OF THE CONDUCTOR FOR THE E-FIELD.
C
C NOTE: WHEN PH12=PH11 AND PH13=0, PNM IS EXACTLY LIKE ORDINARY
C E- AND H-FIELD CALCULATION USING THE MOMENT METHOD.
C
*****

```

```

C
SUBROUTINE PNM(KA,PHI1,PHI2,PHI3,FPNM,JPNM,MEZ,MJZ)
INTEGER SEGMENT,N,M,PHI1,PHI2,PHI3,STEP,NPHI,I,LOOP,SPSIZE
INTEGER SIZE,REMAIN
REAL FPNM(300),DELCON,KA,X(300),Y(300),SIN,COS,SQRT,JPNM(300)
REAL J1,Y1,KRHO,NDOTR,PHI,U,L,PI,MEZ(300),MJZ(300),K,GAMMA,ALOG
REAL JN(300),YN(300)
COMPLEX J,CMLX,LMN(300,301),ALPHAN(300),CURR(300),SUM,UDOTL
PI=3.14159265
J=CMLX(0.0,1.0)
DELCON=PI/PHI1
PHI=DELCON

C
C GENERATE X AND Y COORDINATE POINTS ON THE CONTOUR.
C NOTE THAT X AND Y ARE MULTIPLIED BY THE CONSTANT K
C SINCE X=A*SIN(PHI), NOT X=KA*SIN(PHI).
C
DO 10 N=1,PHI1
  X(N)=KA*COS(N*PHI-PHI/2)
  Y(N)=KA*SIN(N*PHI-PHI/2)
C   WRITE(6,*) N, X(N), Y(N)
10 CONTINUE

C
SIZE=PHI2
SPSIZE=SIZE-PHI3
STEP=0
1 IF (STEP .GE. PHI1) GO TO 7
  REMAIN=PHI1-STEP
  IF (SIZE .GT. REMAIN) SIZE=REMAIN
  DO 20 M=1,SIZE
    DO 30 N=1,SIZE
      IF (M .NE. N) GO TO 2
      LMN(M,N)=1./2.
    GO TO 3
  2 KRHO=SQRT((X(STEP+N)-X(STEP+M))**2
    + (Y(STEP+N)-Y(STEP+M))**2)
    CALL BESSL1(KRHO,J1,Y1)
    NDOTR=((X(STEP+M)-X(STEP+N))*X(STEP+N)
      + (Y(STEP+M)-Y(STEP+N))*Y(STEP+N))/KRHO
    1 LMN(M,N)=J/4.*DELCON*NDOTR*(J1-J*Y1)
  END IF

C
C ADD THE COEFFICIENT OF THE OPPOSITE HALF OF THE CONTOUR.
C
3 KRHO=SQRT((X(STEP+N)-X(STEP+M))**2
  + (Y(STEP+N)+Y(STEP+M))**2)
  CALL BESSL1(KRHO,J1,Y1)
  NDOTR=((X(STEP+M)-X(STEP+N))*X(STEP+N)
    - (Y(STEP+M)+Y(STEP+N))*Y(STEP+N))/KRHO
  1 LMN(M,N)=LMN(M,N)+J/4.*DELCON*NDOTR*(J1-J*Y1)
30 CONTINUE
20 CONTINUE

C
C FILL UP THE LAST COLUMN OF LMN WITH THE EXCITATION FIELD.

```



```

C
DO 40 M=1,SIZE
  LMN(M,SIZE+1)=0.
  IF (STEP .LE. 0) GO TO 4
  DO 50 N=1,STEP
    KRHO=SQRT((X(STEP+M)-X(N))**2+(Y(STEP+M)-Y(N))**2)
    CALL BESSL1(KRHO,J1,Y1)
    NDOTR=((X(STEP+M)-X(N))*X(N)+(Y(STEP+M)-Y(N))*Y(N))
1      /KRHO/KA
    SUM=NDOTR*(J1-J*Y1)
    KRHO=SQRT((X(STEP+M)-X(N))**2+(Y(STEP+M)+Y(N))**2)
    CALL BESSL1(KRHO,J1,Y1)
    NDOTR=((X(STEP+M)-X(N))*X(N)-(Y(STEP+M)+Y(N))*Y(N))
1      /KRHO/KA
    SUM=SUM+NDOTR*(J1-J*Y1)
    LMN(M,SIZE+1)=LMN(M,SIZE+1)+SUM*CURRE(N)*(-1.)
1      *J/4.*KA*DELCN
50      CONTINUE
C      END IF
4      LMN(M,SIZE+1)=-LMN(M,SIZE+1)+CEXP(-J*X(STEP+M))
40     CONTINUE
      CALL GAUSS(SIZE,LMN,ALPHAN)
C
C      STORE THE INDUCED CURRENT ELEMENTS.
C
      DO 110 N=1,SIZE
        CURRE(STEP+N)=ALPHAN(N)
C        WRITE(6,*) STEP+N,CABS(ALPHAN(N))
110     CONTINUE
        IF((STEP+SIZE).NE.PHI1) GO TO 5
        STEP=PHI1
        GO TO 6
5       STEP=STEP+SPSIZE
C     END IF
6     GO TO 1
7     DO 55 I=1,PHI1
        JPNM(I)=CABS(CURRE(I))
55     CONTINUE
C
C     CALCULATE FIELD ALONG PHI; INCREMENT BY EVERY 5 DEGREES.
C
      DO 60 NPHI=1,37
        PHI=PI/36.*(NPHI-1)
        SUM=0.
        DO 70 N=1,PHI1
          U=X(N)*COS(PHI)+Y(N)*SIN(PHI)
          L=X(N)*COS(PHI)-Y(N)*SIN(PHI)
          UDOTL=(COS(U)+J*SIN(U))*(X(N)*COS(PHI)+Y(N)*SIN(PHI))/KA
1          + (COS(L)+J*SIN(L))*(X(N)*COS(PHI)-Y(N)*SIN(PHI))/KA
          SUM=SUM+CURRE(N)*UDOTL*KA*PI/(4.*PHI1)
70     CONTINUE
        FPNM(NPHI)=CABS(SUM)
60     CONTINUE
      ETA=120.*PI

```

```

GAMMA=1.7810742
DO 80 M=1,SIZE
  DO 90 N=1,SIZE
    IF (M .NE. N) GO TO 8
    LMN(M,N)=1.-2.*J/PI*ALOG(KA*DELCN*.163805)
  GO TO 9
8    KRHO=SQRT((X(N)-X(M))**2+(Y(N)-Y(M))**2)
    CALL BESSEL(KRHO,35,JN,YN)
    LMN(M,N)=JN(1)-J*YN(1)
C    END IF
C
C    ADD THE COEFFICIENT OF THE OPPOSITE HALF OF THE CONTOUR.
C
9    KRHO=SQRT((X(N)-X(M))**2+(Y(N)+Y(M))**2)
    CALL BESSEL(KRHO,35,JN,YN)
    LMN(M,N)=LMN(M,N)+(JN(1)-J*YN(1))
90   CONTINUE
80   CONTINUE
DO 85 M=1,SIZE
  LMN(M,SIZE+1)=CEXP(-J*X(M))
85   CONTINUE
CALL GAUSS(SIZE,LMN,ALPHAN)
DO 86 I=1,PHI1
  MJZ(I)=CABS(ALPHAN(I))*4./(KA*DELCN*120.*PI)
86   CONTINUE
DO 95 NPHI=1,37
  PHI=PI/36.*(NPHI-1)
  SUM=0.
  DO 100 N=1,PHI1
    XPHI=X(N)*COS(PHI)
    YPHI=Y(N)*SIN(PHI)
    SUM=SUM+2.*ALPHAN(N)*CEXP(J*XPHI)*COS(YPHI)
100  CONTINUE
  MEZ(NPHI)=CABS(SUM)
95   CONTINUE
RETURN
END
C
C*****
C
C    SUBROUTINE: BESSEL
C    THIS ROUTINE GENERATES BESSEL FUNCTIONS OF 1ST AND 2ND KINDS
C    OF ORDER UPTO 50. IT USES THE RECURRENCE METHOD (9.1.27),
C    TO GENERATE DIFFERENT ORDER OF THE BESSEL FUNCTION. THE
C    ALGORITHM IS SIMPLIFIED BY USING THE WRONSKIAN'S RELATION
C    (9.1.15) AND NEUMANN EXPANSION RELATION (9.1.88). BECAUSE
C    SUBSCRIPT ZERO IS NOT ALLOWED IN THE FORTRAN LANGUAGE,
C    JN(1)=J(X) OF ORDER 0 AND JN(2)=J(X) OF ORDER 1, ETC.
C    NOTE : REFERENCES 9.1.27, 9.1.15, AND 9.1.88 ARE FROM
C           SECTION 9 OF THE HANDBOOK OF MATHEMATICAL FUNCTIONS BY
C           MILTON ABRAMOWITZ AT AL.
C*****
C

```

```

SUBROUTINE BESSEL (X,ORDER,JN,YN)
REAL JN(300), YN(300), FACTOR, PI, SUM, ALOG, X
INTEGER POWER, ORDER, INDEX
PI=3.14159265
JN(ORDER)=0.0
JN(ORDER-1)=1.0
I=ORDER-2
DO 10 INDEX = 1, I
  N=ORDER-INDEX-1
  JN(N) = 2.0*(N)*JN(N+1)/X-JN(N+2)
10 CONTINUE
FACTOR=JN(1)
DO 20 INDEX=3,ORDER,2
  FACTOR=FACTOR+2.0*JN(INDEX)
20 CONTINUE
C
C PERFORM NORMALIZATION
C
DO 30 INDEX=1,ORDER
  JN(INDEX) = JN(INDEX)/FACTOR
30 CONTINUE
C
C CALCULATE Y TERMS USING RECURENCE METHOD
C
SUM=0.0
DO 40 INDEX=3,ORDER,2
  POWER=(INDEX-1)/2
  SUM=SUM+(-1)**POWER*JN(INDEX)/POWER
40 CONTINUE
YN(1)=2.0/PI*(ALOG(X/2.0)+0.577215664)*JN(1)-4.0/PI*SUM
YN(2)=(JN(2)*YN(1)-2.0/(PI*X))/JN(1)
DO 50 INDEX=3,ORDER
  YN(INDEX)=2.0*(INDEX-2.0)/X*YN(INDEX-1)-YN(INDEX-2)
50 CONTINUE
RETURN
END
C
C*****
C
C SUBROUTINE: BESSL1
C THIS ROUTINE GENERATES BESSEL FUNCTION OF 1ST AND 2ND KIND OF
C ORDER 1; IT USES POLYNOMIAL APPROXIMATION LISTED ON PAGE 370
C OF HANDBOOK OF MATHEMATICAL FUNCTONS BY MILTON ABRAMOWITZ.
C
C*****
C
SUBROUTINE BESSL1 (X,J1,Y1)
REAL X,J1,Y1,ALOG,P1,F1,SIN,COS,SQRT,PI
PI=3.14159265
C
C CALCULATE J1 AND Y1 FOR X LESS THAN OR EQUAL TO 3.
C
IF (X .GT. 3.0) GO TO 1
J1=X*(.5-.56249985*(X/3.)**2+.21093573*(X/3.)**4

```

```

1      -.03954289*(X/3.)**6+.00443319*(X/3.)**8
2      -.00031761*(X/3.)**10+.00001109*(X/3.)**12)
      Y1=( (2./P1)*X*ALOG (.5*X)*J1-.6366198+.2212091*(X/3)**2
1      +2.1682709*(X/3.)**4-1.3164827*(X/3.)**6
2      +.3123951*(X/3.)**8-.0400976*(X/3.)**10
3      +.0027873*(X/3.)**12)/X
C
C      CALCULATE J1 AND Y1 FOR X GREATER THAN 3
C
      GO TO 2
1      F1=.79788456+.00000156*(3./X)+.01659667*(3./X)**2
1      +.00017105*(3./X)**3-.00249511*(3./X)**4
2      +.00113653*(3./X)**5-.00020033*(3./X)**6
      P1=X-2.35619449+.12499612*(3./X)+.00005650*(3./X)**2
1      -.00637879*(3./X)**3+.00074348*(3./X)**4
2      +.00079824*(3./X)**5-.00029166*(3./X)**6
      J1=F1*COS(P1)/SQRT(X)
      Y1=F1*SIN(P1)/SQRT(X)
C      END IF
2      RETURN
      END
C
C*****
C
C      SUBROUTINE: GAUSS
C      THIS ROUTINE CAPABLE OF SOLVING UP TO 100 SIMULTANEOUS LINEAR
C      ALGEBRAIC COMPLEX EQUATIONS USING GAUSS ELIMINATION METHOD.
C
C*****
C
      SUBROUTINE GAUSS(SIZE,LMN,ALPHAN)
      INTEGER ROW, COL, SIZE, LAST, MP1, LASTP1, M, N, INDEX, PTR
      REAL DET, CONUM
      COMPLEX LMN(300,301), MATRIX(300,301), ALPHAN(300), SUM
      COMPLEX TEMP, PIVOT, MAXSUM, MAXDIA, MINDIA, CMLPX, ERROR(300)
      ROW = SIZE
      COL = SIZE+1
      LAST= SIZE - 1
C
C      KEEP THE INPUT MATRIX
C
      DO 10 M=1,ROW
         DO 20 N=1,COL
            MATRIX(M,N)=LMN(M,N)
20      CONTINUE
10     CONTINUE
C
C      PERFORM ELIMINATION
C
      DO 30 M=1, LAST
         INDEX=M
         PIVOT=MATRIX(M,M)
         MP1=M+1
         DO 40 N=MP1,ROW

```

```

                IF (CABS (MATRIX (N,M)) .LE. CABS (PIVOT)) GO TO 40
                PIVOT=MATRIX (N,M)
                INDEX=N
C             END IF
40          CONTINUE
C
C          PERFORM ROW INTERCHANGE IF NEEDED.
C
                IF (INDEX .EQ. M) GO TO 1
                DO 50 N=M, COL
                TEMP=MATRIX (INDEX,N)
                MATRIX (INDEX,N)=MATRIX (M,N)
                MATRIX (M,N)=TEMP
50          CONTINUE
C          END IF
C
C          CALCULATION OF ELEMENTS OF NEW MATRIX (AFTER ELIMINATION)
C
1          DO 60 I=MP1, ROW
                DO 70 J=MP1, COL
                MATRIX (I,J)=MATRIX (I,J)-MATRIX (I,M)/MATRIX (M,M)
                *MATRIX (M,J)
70          CONTINUE
60          CONTINUE
30          CONTINUE
C
C          CALCULATE THE DETERMINANT AND THE CONDITON NUMBER OF THE MATRIX
C
                TEMP=MATRIX (1,1)
                MAXDIA=MATRIX (1,1)
                MINDIA=MATRIX (1,1)
                DO 90 N=2, ROW
C          TEMP=TEMP*MATRIX (N,N)
                IF (CABS (MATRIX (N,N)) .GE. CABS (MAXDIA)) MAXDIA=MATRIX (N,N)
                IF (CABS (MATRIX (N,N)) .LE. CABS (MINDIA)) MINDIA=MATRIX (N,N)
90          CONTINUE
                DET=CABS (TEMP)
C          WRITE (6,1000) DET
                CONUM=CABS (MAXDIA/MINDIA)
C          WRITE (6,1010) CONUM
                IF (DET .NE. 0.0) GO TO 2
C          WRITE (6,1020)
                GO TO 3
C
C          PERFORM FIRST STEP OF BACK SUBSTITUTION
C
2          ALPHAN (ROW)=MATRIX (ROW, COL)/MATRIX (ROW, ROW)
C
C          DO THE REMAINDER OF BACK-SUBSTITUTION PROCESS
C
                DO 100 M=1, LAST
                SUM=CMPLX (0.0,0.0)
                PTR=ROW-M
                INDEX=PTR+1

```

```

        DO 110 N=INDEX,ROW
            SUM=SUM+MATRIX (PTR,N) *ALPHAN (N)
110      CONTINUE
        ALPHAN (PTR) = (MATRIX (PTR, COL) -SUM) /MATRIX (PTR, PTR)
100      CONTINUE
C
C      CALCULATE THE COMPUTATION ERRORS
C
        DO 120 I=1,ROW
            SUM=CMPLX (0.0,0.0)
            DO 130 J=1,ROW
                SUM=SUM+MATRIX (I,J) *ALPHAN (J)
130          CONTINUE
            ERROR (I) =SUM-MATRIX (I, COL)
120      CONTINUE
C
C      PRINT THE RESULTING MATRIX AND THE ERROR OF CALCULATION.
C
        DO 140 N=1,ROW
            WRITE (6,*) ALPHAN (N) , ERROR (N)
140      CONTINUE
C      END IF
1000  FORMAT(' ', 'THE DETERMINANT IS: ', F12.6)
1010  FORMAT(' ', 'THE CONDITION NUMBER IS: ', F12.6)
1020  FORMAT(' ', 'THE GIVEN MATRIX IS SINGULAR'/'1')
3     RETURN
END

```

Appendix B

FLOW CHARTS FOR THE OPTIMIZATION PROGRAM

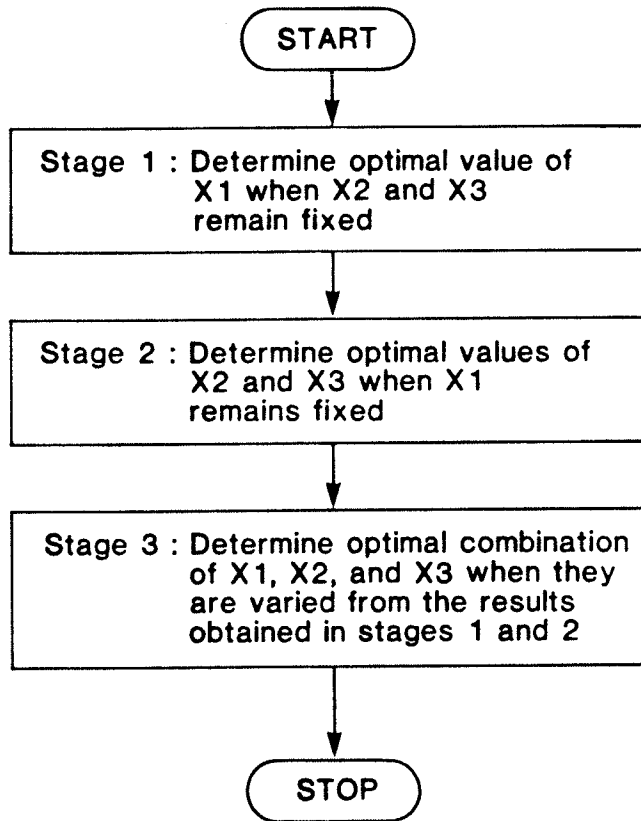


Figure B.1: Block Diagram of the Staged Analysis Program

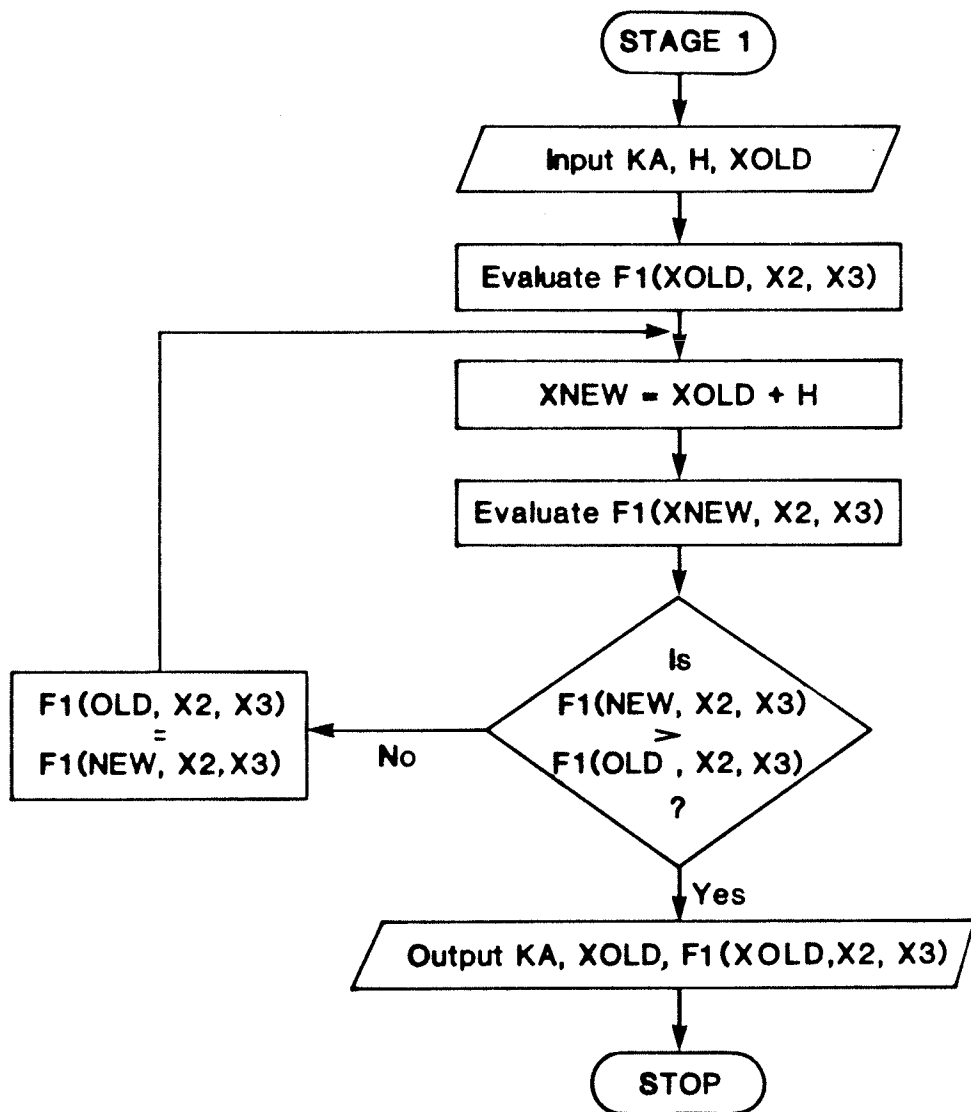


Figure B.2: Flow Chart for Stage 1 of the Staged-program

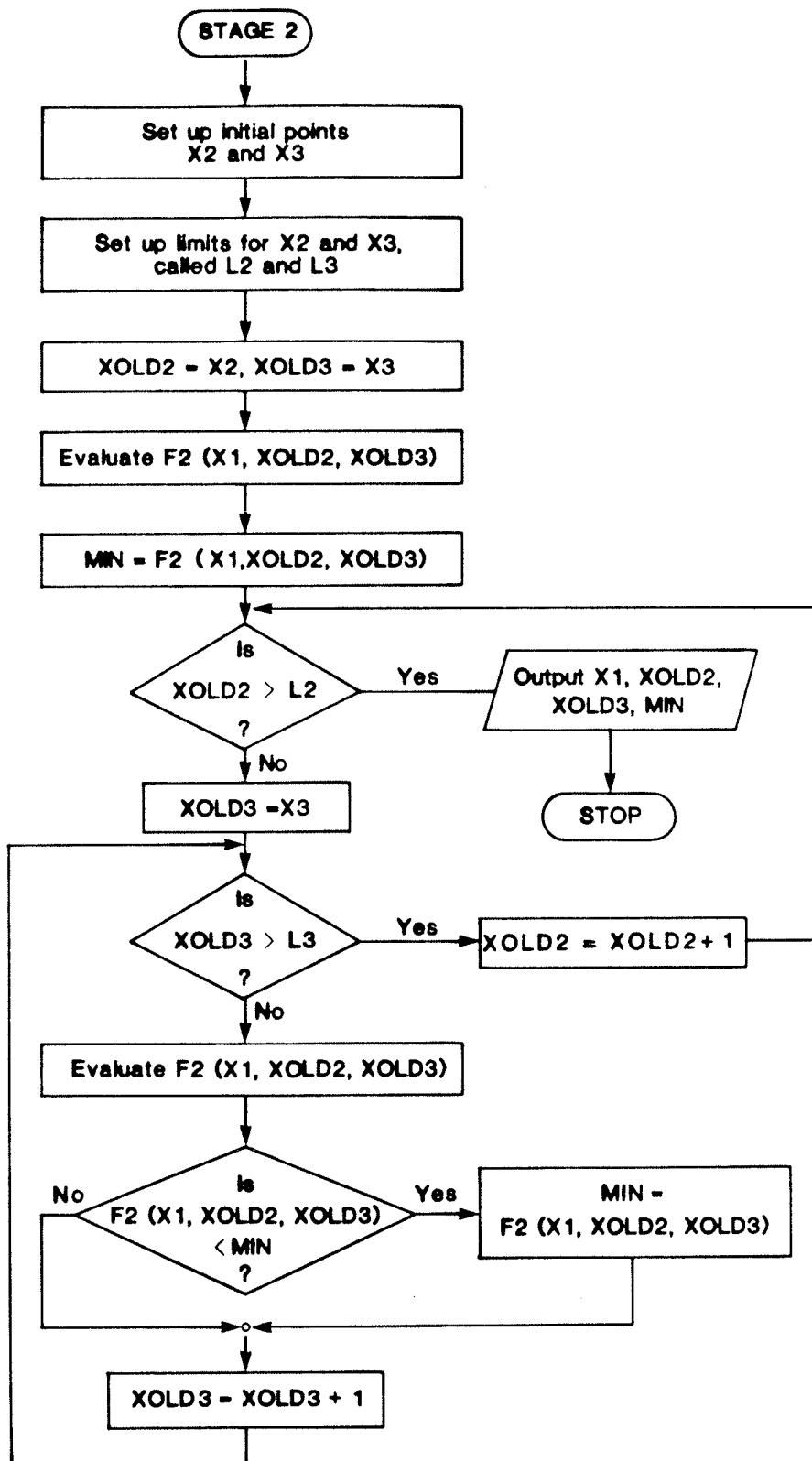


Figure B.3: Flow Chart for Stage 2 (Grid Search)

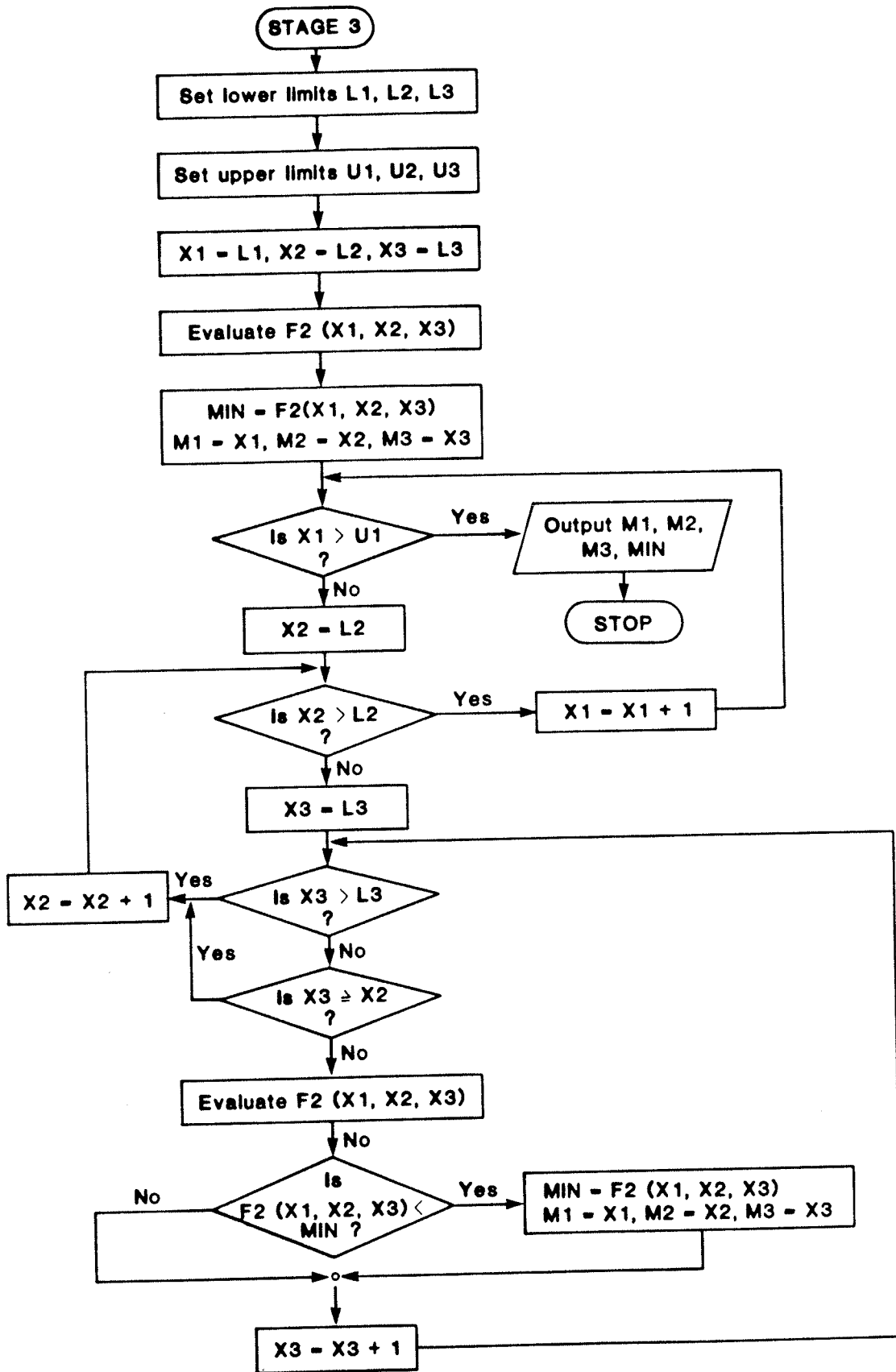


Figure B.4: Flow Chart for Stage 3

Appendix C

MULTI-STAGE OPTIMIZATION PROGRAM

```
INTEGER N,SEGMNT,SUBREG,DISCRD,INDEX,ORDER,TERMS,X(3),POSN
INTEGER DIVISN,IFIX,LAST,RATIO,PHI2,PHI3,LIMIT2,LIMIT3
INTEGER LAMDA,T1,T2,T3,S1,S2,S3,E1,E2,E3
REAL KA,ERROR,MINERR,FEXACT(100),JEXACT(100),MIN,F,TIME1
COMMON /EXDATA/ JEXACT,FEXACT,KA
C
C STAGE 1 - FIND THE OPTIMUM NUMBER OF SEGMENTS WHICH
C CORRESPONDS TO THE MINIMUM ERRORS FOR THE CURRENT ELEMENTS.
C
C START WITH 8 DIVISIONS PER WAVELENGTH AND END WITH
C 15 DIVISIONS.
C
CALL $TRTM(TIME1)
KA=16
RATIO=8
DIVISN=IFIX(KA/2.*RATIO)
LAST=IFIX(KA/2.*(RATIO+7))
CALL FUNCT1(KA,DIVISN,MINERR)
SEGMNT=DIVISN
LAMDA=RATIO
RATIO=RATIO+1
DIVISN=IFIX(KA/2.*RATIO)
20 IF (DIVISN .GT. LAST) GO TO 30
   CALL FUNCT1(KA,DIVISN,ERROR)
   IF (ERROR .GT. MINERR) GO TO 30
   MINERR=ERROR
   SEGMNT=DIVISN
   LAMDA=RATIO
   RATIO=RATIO+1
   DIVISN=IFIX(KA/2.*RATIO)
GO TO 20
30 WRITE(6,*) KA,SEGMNT,LAMDA
C
C STAGE 2 - GENERATE GRID POINTS AND PERFORM THE GRID SEARCH.
C
CALL EXACT(KA,SEGMNT,FEXACT,JEXACT)
PHI2=IFIX(LAMDA*0.5)
LIMIT2=IFIX(LAMDA*1.25)
PHI3=IFIX(LAMDA*0.1)
IF (PHI3 .LT. 1) PHI3=1
NFEVAL=0
T1=LAMDA
T2=PHI2
T3=PHI3
```

```

X(1)=SEGMNT
X(2)=PHI2
X(3)=PHI3
CALL FUNCT(F,X,NFEVAL,W1,W2)
MIN=F
POSN=NFEVAL
40 IF (PHI2 .GT. LIMIT2) GO TO 80
    X(2)=PHI2
    I3=PHI3
    LIMIT3=IFIX(0.75*PHI2)
50 IF (I3 .GT. LIMIT3) GO TO 70
    X(3)=I3
    CALL FUNCT(F,X,NFEVAL,W1,W2)
    IF (W2 .EQ. 100.0) GO TO 80
    IF (W1 .EQ. 100.0) GO TO 70
    IF (F .GE. MIN) GO TO 60
        T2=PHI2
        T3=I3
        MIN=F
        POSN=NFEVAL
60     I3=I3+1
        GO TO 50
70     PHI2=PHI2+1
        GO TO 40
80 WRITE(6,*) POSN,MIN,T1,T2,T3
C
C STAGE 3 - USE ITERATIVE TECHNIQUE TO FIND THE BEST COMBINATION
C
S1=T1-2
S2=T2-2
S3=T3-1
E1=T1+2
E2=T2+2
E3=T3+1
NFEVAL=0
DO 90 I1=S1,E1
    SEGMNT=I1*I1
    CALL EXACT(KA,SEGMNT,FEXACT,JEXACT)
    X(1)=SEGMNT
    DO 100 JJ=S2,E2
        X(2)=JJ
        DO 110 IK=S3,E3
            IF (IK .GE. JJ) GO TO 110
            X(3)=IK
            CALL FUNCT(F,X,NFEVAL,W1,W2)
            IF (F .GE. MIN) GO TO 110
                MIN=F
                POSN=NFEVAL
110     CONTINUE
100     CONTINUE
90     CONTINUE
    CALL $TPTM(TIME1)
    WRITE (6,*) POSN, MIN, TIME1
    STOP

```

```

END
C
SUBROUTINE FUNCT1 (KA, DIVISN, SUMERR)
INTEGER DIVISN
REAL FEXACT (100) , FPNM (100) , JEXACT (100) , JPNM (100) , ANGLE , KA , ERROR
REAL SUMERR, TIME2
CALL EXACT (KA, DIVISN, FEXACT, JEXACT)
CALL $TRTM (TIME2)
CALL PNM (KA, DIVISN, DIVISN, 0, FPNM, JPNM)
SUMERR=0.0
DO 10 I=1, DIVISN
    ERROR=JPNM (I) *ABS (JEXACT (I) -JPNM (I))
    SUMERR=SUMERR+ERROR
10 CONTINUE
CALL $TPTM (TIME2)
WRITE (6, *) KA, DIVISN, SUMERR, TIME2
RETURN
END
C
SUBROUTINE FUNCT (F, X, NFEVAL, W1, W2)
REAL JN (100) , YN (100) , J1, Y1, SECTOR, HALF, PI, ERROR, ANGLE
REAL DJN (100) , DYN (100) , PHI, KA, JPHI (100) , FEXACT (100) , FPNM (100)
REAL JEXACT (100) , JPNM (100) , PREV, SUMCUR, MEMORY, TIME, W1, W2
INTEGER N, SEGMNT, SUBREG, DISCRD, INDEX, ORDER, TERMS, X (3)
COMPLEX SUM, J, CMLX
COMMON /EXDATA/ JEXACT, FEXACT, KA
C
C
C
VARIABLE SUBSTITUTIONS
C
SEGMENT=X (1)
SUBREG=X (2)
DISCRD=X (3)
CALL $TRTM (TIME)
CALL PNM (KA, SEGMNT, SUBREG, DISCRD, FPNM, JPNM)
CALL $TPTM (TIME)
C
C
C
PRINT THE SCATTERED FIELDS WITH 5 DEGREE INCREMENTAL STEPS.
C
SUMFLD=0.0
DO 10 I=1, 37
    ANGLE=I*5.-5.
    ERROR=FPNM (I) *ABS (FEXACT (I) -FPNM (I))
C
    WRITE (6, *) ANGLE, FEXACT (I), FPNM (I), ERROR
    SUMFLD=SUMFLD+ERROR
10 CONTINUE
C
WRITE (6, 1000) SUMFLD
W1=0.0
FTIME=3.0
IF (TIME .GT. FTIME) W1=100.0
W2=0.0
MEMORY=SUBREG*SUBREG*4./1024.
IF (MEMORY .GT. 0.4) W2=100.0
F=SUMFLD+W1*TIME+W2*MEMORY
NFEVAL=NFEVAL+1

```

```

WRITE (6,*) NFEVAL,SEGMNT,SUBREG,DISCRD,F,MEMORY,TIME
1000 FORMAT(' ','THE CUMMULATED ABS ERRORS FOR SCATTERED FIELD: ',
1          F12.6)
1010 FORMAT(' ','THE CUMMULATED ABS ERRORS FOR SURFACE CURRENT: ',
1          F12.6)
RETURN
END

```

```

C
C*****

```

```

C
C      SUBROUTINE: EXACT
C      THIS ROUTINE CALCULATES THE BACK SCATTERING H-FIELD, USING THE
C      ALGORITHM (5-116) LISTED ON PAGE 235 OF TIME-HARMONIC ELECTRO-
C      MAGNETIC FIELDS BY R.F. HARRINGTON. THE ROUTINE INPUTS KA AND
C      SEGMNT AND RETURNS FEXACT, WHERE
C
C      KA = K*A WHERE K: WAVE PROPAGATION CONSTANT AND
C              A: RADIUS OF THE CYLINDER
C
C      SEGMNT = NUMBER OF SEGMENTS ON THE CIRCUMFERENCE
C
C      FEXACT(37) = H-FIELD FROM 0 TO 180 DEGREES INCREMENTED BY
C              5 DEGREES EACH TIME.
C
C*****

```

```

C*****
C

```

```

SUBROUTINE EXACT(KA,SEGMNT,FEXACT,JPHI)
INTEGER I,N,NPHI,SEGMNT,TERMS,ORDER
REAL FEXACT(100),JN(100),YN(100),SECTOR,HALF,PI,DJN(100),DYN(100)
REAL PHI,KA,JPHI(100),ANGLE
COMPLEX SUM,J,CMLPX

```

```

C
C      COMPLEX NUMBER J OPERATOR
C

```

```

J=CMLPX(0.0,1.0)
PI=3.14159265
TERMS=KA+10
SECTOR=PI/SEGMNT
HALF=SECTOR/2.
ORDER=TERMS+1
CALL BESSEL(KA,ORDER,JN,YN)
DO 10 N=1,TERMS
  DJN(N)=-JN(N+1)+JN(N)*(N-1)/KA
  DYN(N)=-YN(N+1)+YN(N)*(N-1)/KA

```

```

10 CONTINUE

```

```

C
C      CALCULATE INDUCED CURRENT
C

```

```

DO 20 I=1,SEGMNT
  PHI=I*SECTOR-HALF
  SUM=-1./(JN(2)-J*YN(2))
  DO 30 N=2,TERMS
    SUM=SUM+2.*COS((N-1)*PHI)/(DJN(N)-J*DYN(N))
  1      *J**(-N+1)*(-1)**(N-1)

```

```

30   CONTINUE
    SUM=J*2./ (PI*KA) *SUM
    JPHI (1) =CABS (SUM)
20   CONTINUE
    DO 40 NPHI=1,37
        PHI=PI/36.* (NPHI-1)
        SUM=JN (2) / (JN (2) -J*YN (2))
        DO 50 N=2,TERMS
            SUM=SUM+2.*COS ( (N-1) *PHI) *DJN (N) / (DJN (N) -J*DYN (N))
            * (-1) ** (N-1)
1
50   CONTINUE
    SUM=SQRT (2./PI*KA) *SUM
C    FEXACT (NPHI) =CABS (SUM)
40   CONTINUE
    RETURN
    END

```

REFERENCES

- [1] Harrington, R. F., Time Harmonic Electromagnetic Fields, McGraw-Hill Book Co., 1961.
- [2] Kleinman, R. E., "The Rayleigh Region," Proc. IEEE, Vol. 53, pp. 848-856, 1965.
- [3] Tew, M. d. and Tsai, L. L., "A Method Towards Improving Covergence of Moment Method Solutions," Proc. IEEE, Vol. 20, pp. 1436-1437, 1972.
- [4] Thiele, G. A. and Thomas, H. N., "A Hybrid Technique for Combining Moment Method with the Geometrical Theory of Diffractions," IEEE Trans., AP-23, No. 1, pp. 62-63, 1975.
- [5] Garbacz, R. J., "Modal Expansions for Resonant Scattering phenomena," Proc. IEEE, pp. 856-864, 1965.
- [6] Shafai, L. Electromagnetic Fields in the Presence of Cylindrical Objects of Arbitrary Physical Properties and Cross-Sections, Ph.D. Dissertation, University of Toronto, Ontario, Canada, 1969.
- [7] Mittra, R., Computer Techniques for Electromagnetics, Pergamon Press, New York, 1973.
- [8] Harrington, R. F., Field Computation by Moment Methods, Macmillan, New York, 1968.
- [9] Brebbia, C. A., The Boundary Element Method for Engineers, Pentech Press, London, 1978.
- [10] Poggio, A. T. and Burke, G. J., Numerical Electromagnetic Code (NEC-1) Part I: NEC Program Description - Theory, Lawrence Livermore Laboratory, 1977.
- [11] Poggio, A. T. and Burke, G. J., Numerical Electromagnetic Code (NEC-1) Part II: NEC Program Description - Code, Lawrence Livermore Laboratory, 1977.
- [12] Poggio, A. T. and Burke, G. J., Numerical Electromagnetic Code (NEC-1) Part III: NEC User's Guide, Lawrence Livermore Laboratory, 1977.
- [13] Shafai, L., "An Improved Integral for the Numerical Solution of Two-dimensional Diffraction Problems," Canadian Journal of Physics, Vol. 48, No. 8, pp. 954-963, 1969.

- [14] Shafai, L. and Bhartia, P., "Scattering Properties of Certain Conducting Cylindrical Geometries," Canadian Journal of Physics, Vol. 51, No. 8, pp. 861-864, 1973.
- [15] Shafai, L. and El-Moazzen, Y. S., "Radiation Patterns of an Antenna near a Conducting Strip," IEEE Trans on Antennas and Propagation, Vol. AP-20, No. 5, pp. 642-644, Sept. 1972.
- [16] Abdelmessih, S. and Sinclair, G., "Treatment of Singularities in Scattering from Perfectly Conducting Polygonal Cylinders - A Numerical Technique," Canadian Journal of Physics, Vol. 45, pp. 1305-1318, 1967.
- [17] Meixner, J., New York University Report EM-72, 1954.
- [18] Kay, A. F. and Nihen, J. F., "Scattering and Currents Induced on Sharp and Rounded Corners," IEEE Trans. on Antennas and Propagation, Vol. AP-14, pp. 112-114, Jan. 1966.
- [19] Lean, M.H., Electromagnetic Field Solution with the Boundary Element Method, Ph.D. Dissertation, University of Manitoba, Manitoba, Canada, 1981.
- [20] Tai, C. T., Dyadic Green's Functions in Electromagnetic Theory, International Textbook Co., Scranton, 1971.
- [21] Wait, J.R. and Jackson, C.M., "Calculation of the Bistatic Scattering Cross-section of a Sphere with an Impedance Boundary Condition," Radio Science, Vol. 69D, No. 2, pp. 299-315, 1965.
- [22] Richmond, J.H., "A Wire-grid Model for Scattering by Conducting Bodies," IEEE Trans. on Antennas and Propagation, Vol. AP-14, pp. 782-786, Nov. 1966.
- [23] Williams, D. and Brammer, D.J., "Moment Method Analysis of VHF Antennas on Vehicles on an Imperfect Ground," 2nd IEE International Conference on Antennas and Prop., (IEE conference publication No. 195, Part 1), pp. 535-538, York, U.K., April 1981.
- [24] Rotman, W. and Karas, N., "The Sandwich Wire Antenna: A New Type of Microwave Source Radiator," IRE National Conversion Records, Part 1, pp. 166-172, Mar. 1957.
- [25] Rotman, W. and Karas, N., "Printed Circuit Radiators, the Sandwich Wire Antenna," Microwave Journal, Vol. 2, pp. 29-33, Aug. 1959.
- [26] Graham, R. and Dawson, C., "A Sandwich Wire Aerial," 1st European Microwave Conf. London, pp. 528-531, Sept. 1969.
- [27] Green, H. E. and Whitrow, J. L., "A New Analysis of the Sandwichwire Antenna," IEEE Trans. on Antennas and Propagation, Vol. AP-19, No. 5, pp. 600-605, Sept. 1971.

- [28] Aboul-Atta, O. and Shafai, L., "Hemispherically Radiating Meander-Line Planar Array Antenna," 3rd IEE International Conference on Antennas and Prop., (IEE conference publication No. 219, Part 1), pp. 141-144, April, 1983.
- [29] Shafai, L. et al, Sandwich Wire Antenna Design, Final Report, DSS Contract No. 36001-2-0112, Serial No. OST82-00033, CRC Radar Research Laboratory, Mar. 1983.
- [30] Hayt, W. W., Engineering Electromagnetics, McGraw-Hill, 1981.
- [31] Taylor, T. T., "Design of Line Source Antennas for Narrow Beamwidth and Low Sidelobes," IRE Trans. on Antennas and Propagation, Vol. AP-3, No. 1, pp. 16-28, Jan. 1955.
- [32] Burnside et al, "A Technique to Combine the Geometrical Theory of Diffraction and the Moment Method," IEEE Trans., AP-23, pp. 551-558, 1975.
- [33] Shafai, L., "A Progressive Numerical Method and Its Application to Large Field Problems in Antennas and Electromagnetic Scattering," Can. Elec. Eng. Journal, Vol. 2, No. 4, 1977.
- [34] Kinzel, J. A., "Large Reflector Antenna Pattern Computation Using Moment Method," IEEE Trans., AP-22, No. 1, pp. 116-119, 1974.
- [35] Walsh, G. R., Methods of Optimization, John Wiley & Sons Ltd., New York, 1975.
- [36] Gottfried, B. S. and Weisman, J., Introduction to Optimization Theory, Prentice-Hall Inc., New Jersey, 1973.
- [37] Zahradnik, R. L., Theory and Techniques of Optimization for Practicing Engineers, Barnes & Noble Inc., New York, 1971.
- [38] Garfinkel, R. S. and Nemhauser, G. L., Integer Programming, John Wiley & Sons Ltd., New York, 1972.
- [39] Wilde, D. J. and Beightler, C. S., Foundation of Optimization, Prentice-Hall Inc., Englewood Cliffs, N.J., 1967.